Modelling of an optical time division demultiplexer.

SWIFT, Graham.

Modelling Of An Optical Time Division Demultiplexer

Graham Swift

A thesis submitted in partial fulfilment of the requirements of Sheffield Hallam University for the degree of Doctor of Philosophy

August 1997

Declaration

I declare that no part of this work has been submitted towards any other academic award.

Graham Swift

August 1997.

Acknowledgements

I would like to acknowledge the School of Engineering at Sheffield Hallam University for funding this project and my supervisory team of Dr. J.R. Travis, Professor A.K. Ray and Z. Ghassemlooy for their advice and encouragement during the production of this work.

I am also grateful to Professor M.J. Adams formerly of British Telecom now with Essex University for his guidance in the early stages.

I would also like to remember my colleagues and friends in the Electronics and Communications Research group for creating a pleasant environment to work in.

A special thanks must also go to Gail, Amy and James who made it all worthwhile.

Abstract

The communication Networks of the future will require signal switching in the optical domain to avoid the inherent speed bottleneck of optical-electronic-optical conversions. This has resulted in an intense research effort in this area. Of particular interest are wavelength division multiplexing (WDM) and optical time division multiplexing (OTDM). The latter offers the advantage that it operates over a single wavelength, removing the problems associated with dispersion in fibre systems whilst the former operates over a number of wavelengths. This thesis concentrates on the modelling and simulation of one particular system: the asymmetric semiconductor laser amplifier loop mirror (ASLALOM) for OTDM.

Initially, a literature review looks at the theory of laser operation which complements the following chapter on laser amplifiers. A review of current optical switching devices will be examined next with regard to switching speeds, crosstalk and the possibility of integration. Also wavelength division multiplexing and time division multiplexing are reviewed, comparing the different systems in current use.

At the present time, no complete models of an asymmetric semiconductor laser amplifier loop mirror have been developed. The intention of this work is to determine the equations necessary for a model to be developed and thus enable the system to be simulated. Computer modelling of a system prior to implementation is advantageous in all aspects of engineering. As this system is still confined to the laboratory a model would complement any practical work and identify critical design parameters.

In this work the Travelling Wave Semiconductor Laser Amplifier (TWSLA) is first modelled in a form which is appropriate for the asymmetric semiconductor laser amplifier loop mirror architecture. The simulations are then used to demonstrate the switching speeds for different configurations and identify any areas needing further work, such as crosstalk, birefringence and polarisation, a method for multi-channel output is also presented. A further aim is to lay a foundation for future work to enable the system to be fully characterised with regard to noise, dispersion and integration.

Glossary Of Symbols And Abbreviations

Abbreviations

AOTF	acousto optic tunable filter
ASE	amplified spontaneous emission
ASLALOM	asymmetric semiconductor laser amplifier loop mirror
BH	buried heterostructure
BLD	bistable linear diode
CW	clockwise
CCW	counterclockwise
DBR	distributed Bragg-reflector
DFB	distributed feedback
DH	double heterojunction
DOS	digital optical switch
EDFA	erbium doped fibre amplifiers
FP	Fabry-Perot
FWHM	full width half maximum
FWM	four wave mixing
GVD	group velocity dispersion
LD	laser diode
LED	light emitting diode
NOLM	non-linear optical loop mirror
NRZ	non return to zero
OTDM	optical time division multiplexing

RZ	return to zero
SLA	semiconductor laser amplifier
SLALOM	semiconductor laser amplifier loop mirror
SNR	signal to noise ratio
SRS	stimulated Raman scattering
TDM	time division multiplexing
TWSLA	travelling wave semiconductor laser amplifier
WDM	wavelength division multiplexing

Symbols

a gain coefficient

c velocity of light

e electronic charge

da/dn absorption cross section

dg/dn gain cross section

E electric field

E_n energy at quantum level n

E_p photon energy

f optical frequency

g material gain coefficient

G_S single pass gain

h Planck's constant

I electric current

m electronic mass

n_0 transparency density

n carrier density

N refractive index

P_C laser pumping due to current

P_n noises signal

r_n field reflection coefficient

R_n power reflection coefficient

S density of photons

t_n field transmission coefficient

T_n power transmission coefficient

T_2 atomic dephasing time

t_n field transmission coefficient

α laser loss coefficient

β_{sp} spontaneous emission factor

Γ confinement factor

τ_2 spontaneous recombination lifetime

τ_p photon lifetime

$\chi^{(3)}$ third order non-linear susceptibility

λ_2 spontaneous decay rate

$g(v)$ lineshape

μ dipole moment

ω radian frequency

Contents

Declaration i
Acknowledgements ii
Abstract iii
Glossary Of Abbreviations And Symbols iv
Abbreviations iv
Symbols vi
Contents viii

1. Introduction To Optical Communications 1

2. Laser Theory 6
2.1 Introduction 6
2.2. Concepts 6
2.2.1 Energy levels and emissions 6
2.2.2 Spontaneous relaxation of inverted carriers 8
2.2.3 Interaction of an electromagnetic wave with an atomic system 8
2.2.4 Optical gain. 10
2.2.5. Theory of laser oscillation 13
2.3. Semiconductor Laser Materials 15
2.3.1 Concepts 15
2.3.2 Laser structures 16
2.4 Laser Rate Equations 18
2.5. Summary 19

3. Optical Amplifiers 21
3.1 Introduction 21
3.2 Optical amplifier applications 21
3.2.1 Receiver amplifier 22
3.2.2 Inline amplifier 22
3.3.2 Wavelength translator 23
3.3 Semiconductor Laser Amplifiers 23
3.3.1 FP basics 23
3.3.2 FP analysis of SLA (Continuous wave) 24
3.3.3 Travelling wave semiconductor laser amplifier (TWSLA) 26
3.3.4 Analysis of TWSLA.(Continuous wave) 27
3.3.5 Noise characteristics of TWSLA's 28
3.4 Carrier Non-Linearities In TWSLA's 30
3.4.1 Intraband and interband transitions 30
3.4.1 Non-linear gain effects 31
3.5 Picosecond Pulse Amplification In TWSLA's 33
3.5.1 Pulse response TWSLA (Experimental observations) 33
3.5.1.1. Regular pulse input at rates > recombination time 33
3.5.1.2 Modulated pulse input in saturation region 35
3.6 TWSLA Dynamics 37

3.6.1 Simplifications 37
3.6.1.1. Homogenous broadening 38
3.6.1.2 Electronic band structure 40
3.6.2 Equations for TWSLA dynamic analysis 40
3.6.3 Pulse propagation dispersive effects 42
3.6.3.1. Dispersive systems analysis 42
3.6.3.2 Pulse broadening and gain dispersion in amplifying devices 45
3.7 Ultrashort Pulse Amplification In TWSLA's 46
3.7.1 Pump probe method 46
3.7.2 Temporal response 47
3.7.3 Gain saturation 48
3.7.4 Analytical description of gain saturation of ultra-short pulses 49
3.8. Summary 52

4 Optical Switching And Routing 53
4.1 Introduction 53
4.2 Mach Zender Interferometers 53
4.2.1 Thermo-optic 54
4.2.2. Stress-optic phase shifter 55
4.2.3 Electro-optic method 55
4.2.4. TWSLA devices 56
4.3 Directional Coupling. 58
4.3.1 Semiconductor directional couplers 58
4.3.2 Thermo-optic switching directional couplers 60
4.4. Digital Optic Switch 61
4.4.1. Semiconductor DOSs 62
4.4.2. Polymer DOSs using thermo-optics 66
4.5 Acousto Optic Switching 68
4.6. Opto-mechanical reflection switching 70
4.7. Electrostatic Mechanical Switching 71
4.8 Switching Architectures 73
4.6.1 Mach Zender thermo-optic. 73
4.6.2. Electro-optic directional coupler. 74
4.6.3 Lithium niobate DOS. 76
4.6.4 TWSLA array 76
4.7 Summary 77

5. Optical Multiplexing And Demultiplexing 78
5.1. Introduction. 78
5.2. Wavelength division multiplexing 78
5.2.1 Concepts. 78
5.2.2 Implementation of a WDM network 81
5.3 Optical Time Division Multiplexing 82
5.3.1 Concepts of OTDM. 83
5.3.2 OTDM processing nodes 83
5.3.3 Optical time division multiplexing techniques 84
5.3.3.1 Passive multiplexing. 85

5.3.3.2 Active multiplexing. 86
5.3.4 Optical time division demultiplexing techniques 88
5.3.4.1 Demultiplexing using FWM 89
5.3.4.2 Non linear optical loop mirror 92
5.3.4.3 Semiconductor laser amplifier loop mirror (SLALOM) 95
5.3.4.4 Asymmetric semiconductor laser amplifier loop mirror (ASLALOM) 97
5.4. Summary 100

6. Modelling Of TWSLA 102
6.1. Introduction 102
6.2 Input Signal Modulation Time And Saturation Intensity 102
6.3 Continuous Wave And High Data Rate Models 103
6.3.1 Steady state simulations 103
6.3.2 Analytical solution 104
6.3.3 Numerical solution 105
6.3.4 Analytical v numerical solution 107
6.4 Dynamic (Pulse) Input Analysis 108
6.4.1 Dynamic modelling of picosecond pulse inputs. 108
6.4.2 Longitudinal averaging method (point element model) 109
6.4.3 Point element model simulations 111
6.4.4 Finite length model 116
6.4.5 Finite length model simulations 119
6.4 Summary 118

7. Modelling Of ASLALOM 120
7.1 Introduction 120
7.2 Modelling Of Fused Fibre Coupler 121
7.3 Matrix Analysis Of Propagation Through ASLALOM 124
7.3.1 Matrix equation 124
7.3.2 Power transmission coefficients 127
7.4 Phase And Gain Responses 128
7.4.1 Simulation of the loop mirror phase response with constant gain 128
7.4.2 Simulation of the loop mirror gain response with constant phase 130
7.5 Loop Asymmetry 131
7.5.1. Large asymmetry loops 131
7.5.2 Medium asymmetry loops 134
7.5.3. Small asymmetry loops 136
7.5.3.1 Simulations with finite length effect of TWSLA 141
7.5.3.2 CCW modulation time 145
7.5.3.3 Window amplitude 147
7.5.3.4. Comparison between simulated and practical results 148
7.5.3.5 Data pulse input 150
7.5.4 High frequency control input 155
7.5.4.1 Response of ASLALOM with 100 GHz control 156

signal
7.5.4.2 CCW data response and the finite length effect 158
7.5.5 Binary data input 164
7.5.6. Patterning 168
7.5.7. A method for multi-output data 170
7.6. Birefringence and polarisation effects in an ASLALOM 174
7.6.1. Jones matrix of waveplate 174
7.6.2 Waveplate in a fibre loop 177
7.6.3 Birefringence in ASLALOM 179
7.6.4 Compensating for birefringence 180
7.7 Summary 181

8. Conclusions And Suggestions For Further Work 183
8.1 Conclusions 183
8.2 Suggestions For Further Work 187

References 189

Chapter 1

Introduction To Optical Communications

Communication technology has made significant advances with the increase of semiconductor technology and system development. Traditional communication techniques based on electronics are now being challenged by new optical systems. As early as 1880 Alexander Graham Bell reported the modulation of sunlight with the sound of a bell achieving speech transmission over a distance of 200 m [Bell 80]. For atmospheric communication, light was really only practical for line of sight, short distance transmission, since scatter and weather conditions were proving to be an obstacle for the optical signal. To overcome some of these problems, dielectric waveguiding which has a history dating back to 1910 [Hondros 10] was used to confine the signal. In 1950 B 0' Brian Sr. at American Optical was developing optical fibre bundles for light transmission. Interest in fibre communications grew when Kao [Kao and Hockham 66] predicted that 20 dB/km loss was achievable in glass fibres by removing the impurities. At this level, optical fibre communication was becoming a viable alternative. Prior to this the losses were in the 1000 dB/km range (coaxial cables which guide electromagnetic waves exhibit losses between 5 and 10 dB/km). In addition to high losses, other practical aspects had to be overcome with optical fibres such as jointing which needed to be performed quickly and easily by engineers in the field. Military applications were the first to use optical communications where conditions were unsuited to electromagnetic methods. Inevitably research continued on optical fibres and by 1977 the fibre losses had been reported as low as 0.5 dB/km for 1200 nm wavelengths. Early optical systems used multimode graded index fibres in the 0.85μm

wavelength region. Single mode fibres were difficult to joint and the availability of semiconductor light sources and silicon photodetectors was poor. Single mode fibres have the advantage of polarisation preservation, higher bandwidths and less fibre attenuation and, because of these advantages, interest in single mode fibres was renewed at the end of the 1970s. In parallel with the development of fibre systems, work proceeded on the various components to complete the optical communication system. Semiconductors as optical sources included light emitting diodes (LED) and injection lasers which were compatible in size with the optical fibre system. LEDs operate at much lower current than injection lasers. However their mechanism of light generation is by spontaneous emission and consequently the optical output of an LED is of random phase with no coherence. The injection laser on the other hand uses stimulated emission in a resonant cavity providing a coherent light source. The spectral width of an LED is also much wider than the laser. For 800-850 nm wavelength operation GaAlAs devices have spectral widths in the range 30-60 nm and 1-2 nm for LEDs and lasers respectively. However the LED does offer certain advantages over the laser, e.g. lower cost, ease of manufacture, reliability, and it gives a linear light output current curve . The first semiconductor lasers were fabricated from alloys of gallium arsenide which emitted in the range 0.8 to 0.9μm. The range of emission was extended to 1.1 to 1.5μm, taking advantage of improved fibre characteristics. The laser and LED were now becoming well established with a lifetime improvement from a few hours up to 25 years for semiconductor lasers and 100 years for LED's. Table 1.1 shows how laser diodes have developed over the years.

Years	1960	1970		1980	1990
LD Quality	Lasing	CW operation	Single transverse mode	Single longitudinal mode	Functions
Physics		Confinement	Index guiding	Wavelength filter	Nonlinearity
Structure	Homojunction	DH	BH	DFB, DBR	BLD, LD Amplifier
Application			Fibre comms. CD.	High bit rate fibre comms. Coherent comms	Photonic switching Optical signal processing

Table 1.1 Development steps of laser diodes.

The research and development into fibre communication systems is driven by the promise of communication systems offering numerous advantages such as greater bandwidth, small size, lower costs and high interference immunity. Figure 1.1 shows how the bit rate distance product has increased with new technologies.

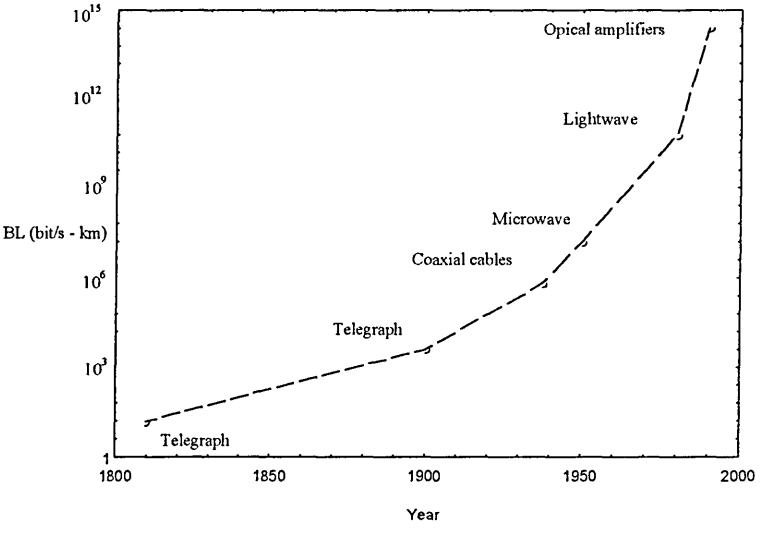

Figure 1.1 Bit rate distance product with the emergence of new technologies.

For a point to point communication system optical fibres are becoming well established, and this is the most common use of optical communication systems, any processing of the signal is performed by an optical to electronic conversion and processing the signal

using electronic methods, the signal then has to be converted back to the optical domain. This creates a time bottleneck which significantly reduces the speed of transmission. The challenge now facing the system designer is in the switching of the signal. The speed limitation of electronic switching is currently limited to about 10 Gbit/s [Zhang 96]. The requirements of future broadband multimedia services is likely to require switch speeds of the order of 100 Gbit/s. Application areas include medicine, education/training, banking etc. These will be serviced by various communication services i.e. high and low speed data, text, graphics, image, voice, audio and video. These particular services have different requirements in terms of traffic and performance. For example HDTV requires 1 Gbit/s data if no compression is used and 150 Gbit/s using complex compression techniques [Zhang 96]. Thus two hundred HDTV channels would require an aggregate bit rate between 30 Gbit/s and 200 Gbit/s. A study into the development of a European network linking major centres in Europe is "COST 239: Ultra-High Capacity Optical Transmission Networks" [O'Mahony 93] The findings of this study in terms of data capacity are summarised in table 1.2.

Cities	Data rate (Gbit/s)
London- Paris	150
Paris - Madrid	120
Zurich -Milan	90
Milan - Rome	120
Prague - Berlin	90
Berlin -Moscow	90

Table 1.2
Typical data requirements of European cities.

To achieve switching of an optical signal some kind of nonlinearity in a material is required which imposes an amplitude or phase shift on an optical signal [Islam 94]. Non linear effects of certain materials allowed for the construction of interferomic devices e.g. non linear directional couplers [Jensen 82], Kerr switches [Morioka and Sarawatari 88],

Mach Zender devices [Al-hemyari et al 94] and loop mirrors [Blow et al 90] which are able to switch in the optical domain.

As in any engineering system, reliable models need to be developed to enable simulation before actual construction takes place. This project is concerned with developing mathematical models of the ASLALOM. The accuracy of the model will depend on the assumptions and the approximations made which will inevitably be determined by the system requirements. Therefore the initial aim is to identify the equations which describe such an optical system and to build a model which is in agreement with current practical results. When a satisfactory model has been developed performance of the system will be investigated. Further work will consider the characteristics of the system which may hinder the performance, such as polarisation, birefringence and crosstalk.

Chapter 2

Laser Theory

2.1 Introduction

The purpose of this chapter is to introduce the underlying theoretical fundamentals of laser operation. The concept of energy levels as a quantised concept will lead to a general approach to the interaction of light with an atomic system. With these basics the operation of lasers can be explained, assisting the explanation of laser amplifier operation given in a later chapter.

2.2 Concepts

2.2.1 Energy levels and emissions

A picture of laser basics can be built up by referring to the concept of energy levels within an atomic system. In this description, the energy of electrons within the system are quantised, i.e. an electron can only exist at specific energy levels. Figure 2.1 depicts a simple two level system where only two energy levels, E_1, E_2 ($E_2 > E_1$) are shown.

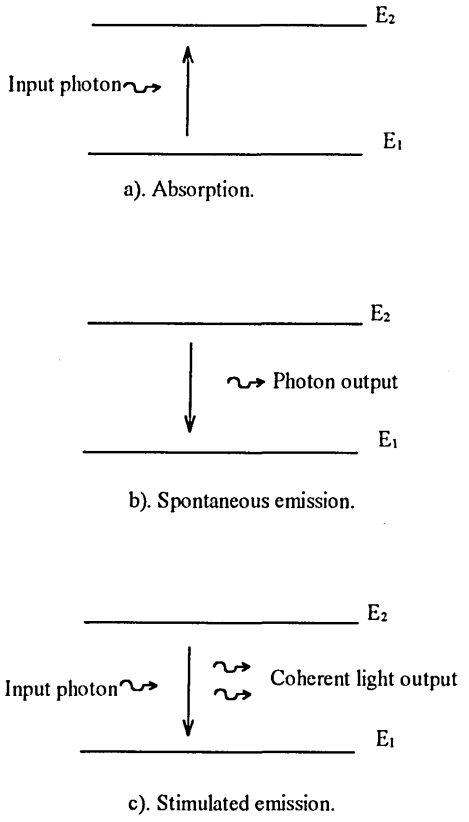

Figure 2.1 Energy levels and emissions.

Referring to Figure 2.1 if a photon is incident on the atomic media with an energy approximately equal to the gap between E_2 and E_1 (E_2 - E_1), absorption occurs and an electron is excited to a higher energy level (E_2) with an increase in potential energy equal to E_2 - E_1. The electron, on moving to a higher potential, is said to be in an "excited state". Absorption can take place for a definite amount of light input until 'population inversion' is reached. There are two mechanisms of emission where the electrons fall back to their original level; spontaneous and stimulated. As shown in Figure 2.1b, photon release can occur spontaneously when an electron falls from level E_2 to E_1 after a certain time has elapsed. Stimulated emission is described by figure 2.1c; whereby a photon incident on the material causes an electron to drop to level E_1 with two photons

emitted coherently. The frequency f of the emitted photon is $f = (E_2 - E_1)/h$ where h is Planck's constant.

2.2.2 Spontaneous relaxation of inverted carriers

To illustrate the natural decay of inverted electrons consider the previous two level system when a certain density of electrons n_2 have been pumped to an upper energy level E_2. As discussed these electrons will give up their energy by recombining and returning to level E_1. The rate at which electrons spontaneously decay or recombine is described by a spontaneous decay rate (γ_2) times the instantaneous number of electrons in that level i.e:

$$\left.\frac{dn_2(t)}{dt}\right|_{spont} = -\gamma_2 n_2(t) \equiv -\frac{n_2(t)}{\tau_2} \tag{2.1}$$

where n_2 is the density of electrons in level E_2 and τ_2 is termed the lifetime of electrons in level E_2. The atoms in level E_2 will recombine exponentially thus:

$$n_2(t) = n_2(0)e^{-\gamma_2 t} = n_2(0)e^{-\frac{t}{\tau_2}} \tag{2.2}$$

2.2.3 Interaction of an electromagnetic wave with an atomic system

Atomic lineshape

The theory behind the interaction of photons with an atomic system provides an explanation of various concepts. If a spectral analysis is performed of the radiation emitted by spontaneous ($E_2 \rightarrow E_1$) transitions for a two level system it is found that the radiation is not strictly monochromatic and occupies a finite frequency bandwidth. The function which describes the distribution of emitted intensity versus frequency (ν) is referred to as the line shape function, $g(\nu)$. Alternatively $g(\nu)$ can be determined by applying an electromagnetic field to the atomic system and plotting the amount of energy

absorbed by the 1→2 transitions as a function of frequency. The function $g(\nu)$ is usually normalised to unity according to [Yariv 91]:

$$\int_0^\infty g(\nu)d\nu = 1 \tag{2.3}$$

With the assumption that $\int_{\nu_1}^{\nu_2} g(\nu)d\nu$ is the probability that a 2→1 transition will result in a photon whose frequency is between ν_1 and ν_2.

An explanation of the frequency spread may be obtained by considering the interaction as a decaying oscillation. This is the basis of an attempt to describe the whole process as an electron which oscillates when displaced from a position of equilibrium within an electric field. The oscillations obey the following equation of motion [Christov 88]:

$$\frac{d^2\mu(t)}{dt^2} + \gamma\frac{d\mu(t)}{dt} + \omega_a^2\mu(t) = -\frac{e}{m}E(t) \tag{2.4}$$

where μ is the induced dipole moment due to an electric field E, e the electronic charge, m the electronic mass and ω_a the system resonant frequency. With no applied signal the system decays with a rate γ thus:

$$\mu(t) = \mu_0(t_0)\exp\left(\gamma(t-t_0) + j\omega_a(t-t_0)\right) \tag{2.5}$$

Equation (2.5) has a lineshape frequency function of the form:

$$l(\omega) = \frac{A}{1+[2(\omega_a-\omega)^2/\Delta\omega_a]^2} \tag{2.6}$$

where A is a constant of the material and $\Delta\omega_a = 1/\gamma$ is the full width half maximum (FWHM) of the response.

Figure 2.2 depicts a typical lineshape amplitude response using equation 2.6.

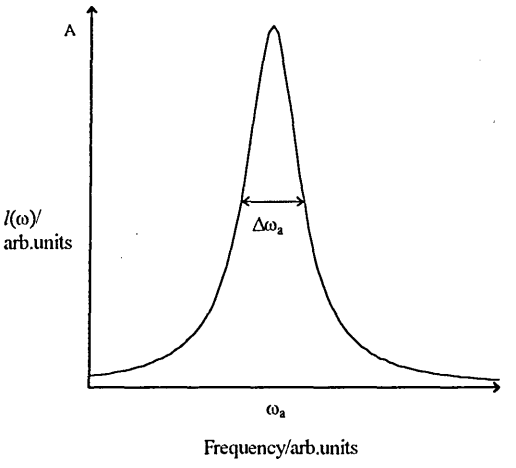

Figure 2.2 Typical lineshape function for an atomic medium.

Dephasing

The lineshape does not describe the whole picture and a further concept to consider is the dephasing time when a signal is incident on an atomic media. De-phasing arises from collisions within the atomic system which alter the properties of a wave by changing its phase. As time progresses more collisions occur and the signals gradually become more out of phase. The result is a random interference which is characterised by a dephasing time T_2. The decay due to dephasing is shorter than the decay time in equation 2.6 and tends to dominate over that of the natural decay of the atomic transition. The modification of the frequency response is such that $\Delta\omega_a = 1/\gamma + 2/T_2$. Typical times of T_2 for semiconductor lasers are 0.1 ps [Agrawal 91].

2.2.4 Optical gain

Optical gain is a concept which is possible in a device with a sufficient number of carriers when population inversion occurs and from the concept of lineshape the gain is expected to possess a frequency spectrum. Table 2.1 lists the gain bandwidth of some common laser materials.

Gain medium	Bandwidth
He-Ne	1.5 GHz
Argon ion	6 GHz
Nd-YAG	12 GHz
Ruby	60 GHz
RD 6G Dye	10 THz
GaAs	60 THz
Ti-sapphire	150 THz

Table 2.1 Bandwidth of some laser gain media.

Semiconductor laser amplifiers possess specific gain properties. The value of gain per unit length is very high, in the region of 100/cm due to the efficient pumping process in semiconductor materials. This is an order of magnitude higher than any other type of laser [Kawaguchi 94]. This property allows these devices to be made small, typically less than 1 mm. The gain curve has a bandwidth in the range of tens of nanometres. The gain near to threshold can be expressed in parabolic form using the following equation [O' Mahony 88]:

$$g(n,\lambda) = a_1(n-n_0) - a_2(\lambda - a_3(\lambda_0 - (n-n_0)))^2 \qquad (2.7)$$

where g represents the gain coefficient per unit length, n_0 the carrier density required to achieve optical gain, a_1, a_2 and a_3 coefficients of the material, λ the signal wavelength and λ_0 the peak gain wavelength. Figure 2.3 is a gain plot of an inverted system using equation 2.7 with the carrier density as a parameter, values used are $a_1 = 2.7 \times 10^{-20}\text{m}^2$, $a_2 = 1.5 \times 10^{19}\text{m}^{-2}$, $a_3 = 2.7 \times 10^{-28}\text{m}^4$, $\lambda_0 = 1.55 \times 10^{-6}\text{m}$.

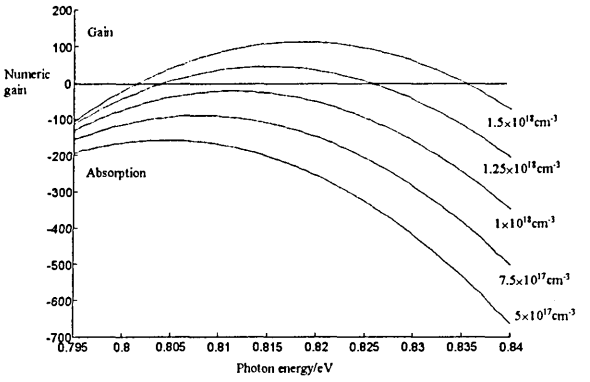

Figure 2.3 Gain coefficient v Photon energy.

A signal with Power P_{in} propagating over a length L will undergo amplification according to the following equation:

$$P_{out} = P_{in} \exp(g(n,\lambda)L) \tag{2.8}$$

When the device carrier concentration is below n_0 the signal is absorbed and this is represented as negative gain. With concentrations above n_0 stimulated emission occurs and amplification of the signal occurs. Values of gain coefficient can be calculated and are usually done numerically [Agrawal 86] and a relationship between gain and photon energy of the signal can be formulated. A useful linear relationship evolves from this giving:

$$g = a(n - n_0) \tag{2.9}$$

where the value of a is determined over a linear part of the gain/absorption carrier density curves i.e. $a \approx dg/dn_c$ (see figure 2.4), a signal is absorbed if $n < n_0$ and amplified if if $n > n_0$.

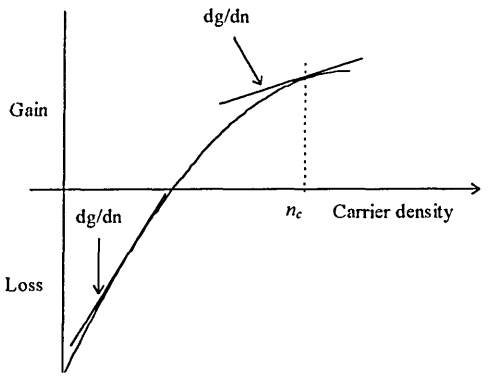

Figure 2.4 Gain and absorption curves for a semiconductor.

2.2.5. Theory of laser oscillation

Equation 2.7 shows that gain exists in a material with a population inversion. Consider the case where the material in question is placed between two mirrors with reflectivity r_1 and r_2 forming a FP cavity (see figure 2.5).

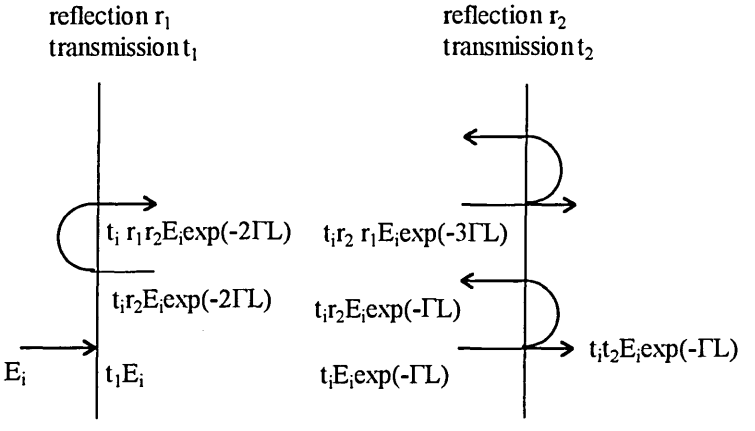

Figure 2.5 Laser oscillation between reflecting surfaces.

When an optical signal propagates along such a cavity it undergoes gain as defined by equation (2.9) and it also experiences losses with a coefficient α. A plane wave of wavelength λ is considered without any time dependence and is defined as E_i. On

entering the cavity the field just inside the left boundary is given by $E_i t_1$ where t_1 is the ratio of transmitted to reflected fields at the left mirror and t_2 the ratio of transmitted to reflected fields at the right mirror. The field will now travel from left to right undergoing gain and loss. The field at the right mirror is then:

$$t_1 E_i \exp\text{-}(\Gamma_i L) \tag{2.10}$$

where $\Gamma_i = (j2\pi NL/\lambda) + (g - \alpha)$ and N the refractive index of the material.

After progressive round trips along the cavity the outgoing wave is given as:

$$E_t = t_1 t_2 E_i \exp\text{-}(\Gamma_i L)(1 + r_1 r_2 \exp\text{-}(2\Gamma_i L) + r_1^2 r_2^2 \exp\text{-}(4\Gamma_i L) + \ldots) \tag{2.11}$$

This is a geometric progression which can be re-written as:

$$E_t = E_i \left[\frac{t_1 t_2 \exp(-\Gamma_i L}{1 - r_1 r_2 \exp(-2\Gamma_i L} \right] \tag{2.12}$$

For a laser to oscillate a finite transmitted wave E_t exists with zero input E_i. This corresponds with the denominator of equation 2.12 being equal to zero i.e.

$$r_1 r_2 \exp(-2\Gamma_i L) = 1 \tag{2.13}$$

Making the substitution $\Gamma_i = g - \alpha$ in equation 2.13 gives an amplitude requirement for oscillation as:

$$g = \alpha + (1/L)\ln(1/r_1 r_2) \tag{2.14}$$

To satisfy the phase condition the phase on returning must be a multiple of 2π i.e. $\frac{4\pi NL}{\lambda} = 2m\pi$, where $m = 1,2,3 \ldots$

from which $m(\lambda/N) = 2L$.

The analysis shows that a laser tends to oscillate at a frequency coincident with a longitudinal mode supported by a FP cavity. The frequency depends on the gain spectrum of the medium. If the material has a linewidth as described in section 2.2.2

then the frequency whose longitudinal mode is nearest to the gain peak frequency (ω_a in figure 2.2) reaches the gain requirement of equation 2.14 and the laser operates in a single longitudinal mode.

2.3. Semiconductor Laser Materials.

2.3.1 Concepts

A lasing device can be formed from a non-degenerate semiconductor *P-N* junction in which a population inversion is created by the injection of current into the junction (figure 2.6).

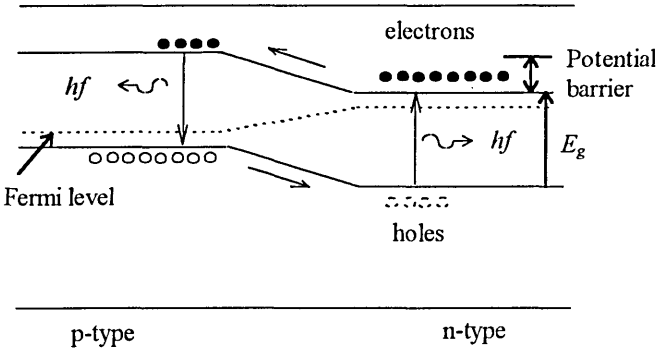

Figure 2.6 Semiconductor laser junction.

If a potential difference is applied across the device, the potential barrier is reduced and electrons can flow across to the p-type region with an increased energy causing population inversion. With electroluminescent materials, recombination of electrons and holes across the bandgap in the P-type material occurs with the release of a photon of energy E_g as in section 2.1.1. Similarly holes can populate the valence band in the N-type region and recombine with electrons to release a photon. Efficient laser devices require the use of a direct bandgap material [Senior 92], since this ensures a direct

transition across the energy gap with the possible emission of a photon. Indirect bandgap materials require the inclusion of a third particle (a phonon) with recombination times longer and non radiative recombination more likely. Non radiative recombination occurs as a result of energy released as lattice vibrations dissipated as heat. Examples of direct/indirect bandgap materials are given in Table 2.2.

Semiconductor Material	Direct/Indirect
GaAs	Direct
GaSb	Direct
InSb	Direct
Si	Indirect
Ge	Indirect
GaP	Indirect

Table 2.2 Direct and indirect bandgap Semiconductor materials.

2.3.2 Laser structures

Figures 2.7a, b and c show the evolution of semiconductor laser structures which differ in their complexity and efficiency of operation.

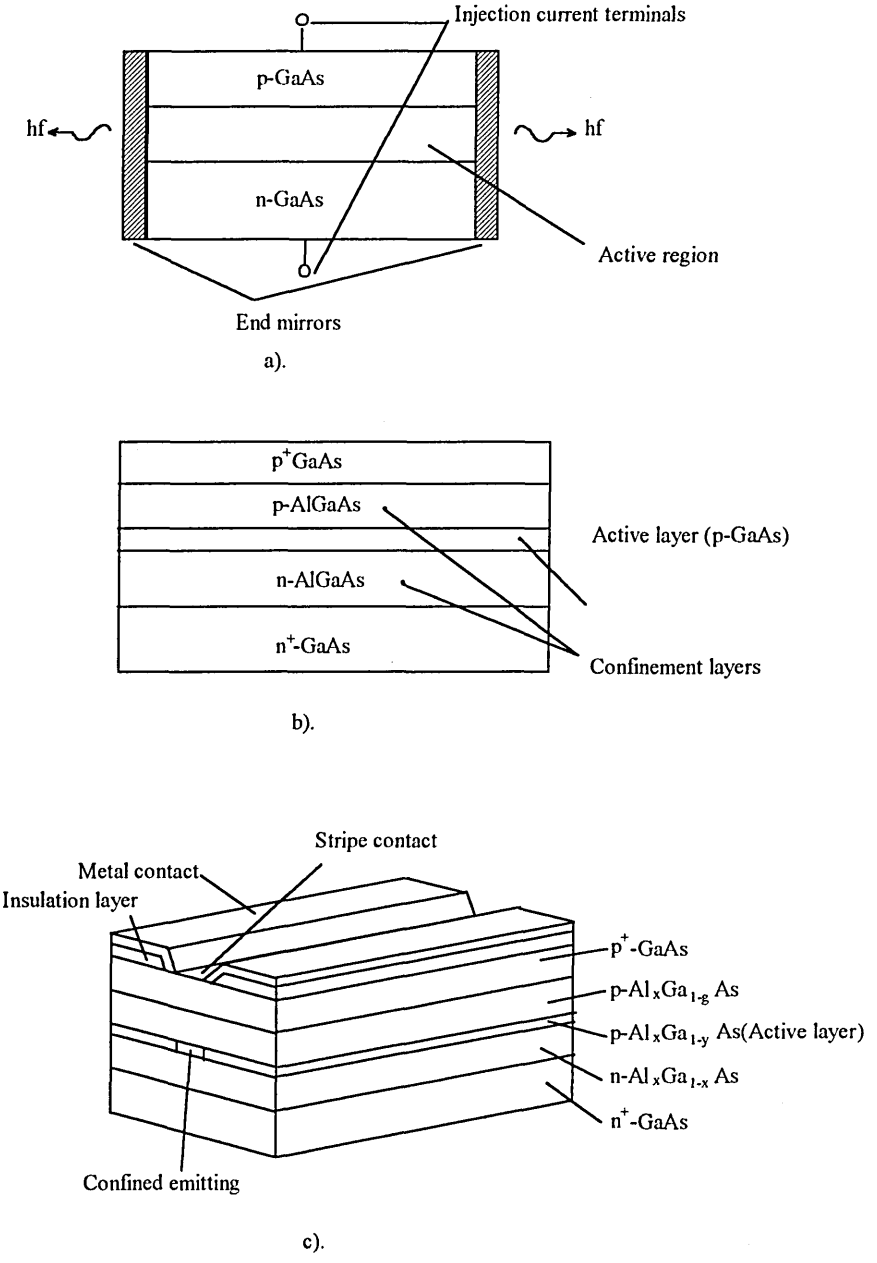

Figure 2.7 The evolution of semiconductor laser structures.

Figure 2.7a shows the basic structure of a homojunction laser. The shaded ends of the diagram depict partially reflective mirrors to form a FP device. In this device the refractive index step at the edge of the gain region is small and the signal light spreads out into the surrounding GaAs structure. The optical confinement is poor (large α), so, as shown by equation 2.14, a higher gain (and higher current) is required. The higher

currents result in higher operating temperatures. To overcome some of these problems double heterojunction (DH) structures are utilised. Figure 2.7b shows a diagram of a broad area GaAs/AlGaAs DH laser. This device gives improved optical and carrier confinement. The optical confinement is provided by wave guiding of the signal, achieved through a step index profile which is greater than the homojunction. This device requires lower threshold currents and can be operated with continuous wave output. A more reliable device is achieved with a stripe geometry DH laser as shown in figure 2.6c The active region does not extend to the edge of the material thus providing better confinement. Electrical contact is in the form of a stripe running along the device, the resulting emitting region being considerably reduced.

2.4 Laser Rate Equations

The interplay between the current injected carriers in a semiconductor laser is described by a set of laser rate equations. The foundation for these is demonstrated in figure 2.7.

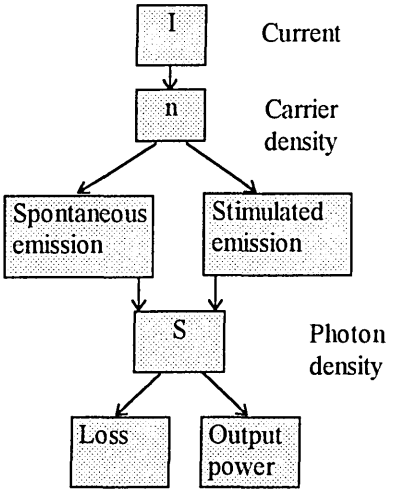

Figure 2.7 Interaction of photons and carriers in semiconductor laser.

With reference to figure 2.7 two rate equations can be written:

$$\frac{dn}{dt} = \frac{I}{eV} - g(n)Sv_g - \frac{n}{\tau_2} \tag{2.15}$$

$$\frac{dS}{dt} = g(n)Sv_g + \frac{S}{\tau_p} + \beta_{sp}\frac{n}{\tau_2} \tag{2.16}$$

Equation 2.15 and 2.16 describe the rate of change of carriers within the device (note: the effect is localised to one spatial position) . The first term on the right hand side of equation 2.16 describes the carrier input due to a current I into an active volume V, which confines current and photon input. The second term is due to stimulated emission in which photons, with a density S stimulate more photons reducing the carrier density (hence the negative sign), g is as equation 2.9 and v_g is the photon velocity. Spontaneous emissions also remove carriers as described by the third term. Equation 2.16 is a photon density equation. Production of stimulated photons is defined by the first term (which is the equivalent of the second term in equation 2.15). Some photons are lost and this is described by a lifetime τ_p in the second term. The third term describes spontaneous emissions which also produce photons but since only a fraction of these are supplied to the lasing mode an additional factor β_{sp} is required.

2.5. Summary.

The purpose of this introductory chapter has been to introduce various optical concepts which form the foundation for later work. The initial section was concerned with discussing atomic systems and introducing basic quantum electronics. The theory of an electromagnetic wave interacting with an atomic material explained the frequency distribution/gain of optical signals which lay the foundation for discussions on gain

dispersion in such a device. The laser rate equations have been introduced to describe the interaction between photons and carriers in a laser device.

Chapter 3

Optical Amplifiers

3.1 Introduction

This chapter is concerned with the use of Semiconductor laser amplifiers (SLAs) both in industry and in the laboratory. Initially a brief introduction to the use of SLAs in optical communication systems will be given. SLAs are basically divided into two types of device: the FP and travelling wave(TW). A description of each is given with the accompanying equations which describe the characteristics of the device under continuous wave input. The main emphasis of the chapter will focus on the travelling wave amplifier and will be the device described after the FP analysis. The concept of noise with origin stemming from amplified spontaneous emission is described. Its relevance to receiver generated noise will be shown by the noise equations. Pulse amplification in TWSLAs will be reviewed and experimental observations produced. The amplification of ultrashort pulses will be discussed.

3.2 Optical Amplifier Applications

With the continuing transition of telecommunication networks from electronic to optical it is envisaged that optical amplifiers are expected to play a significant role in future fibre networks [Potenza 96]. Their use may extend from discrete amplifier components to a more active part in switching and routing [Melle 96], WDM and OTDM [Ellis 93]. The high bandwidth of optical amplifiers (erbium doped fibre amplifiers (EDFA) have a bandwidth of 25 terahertz) means they can be included in a multi-wavelength multiplexed

signal [Yu and O'Mahony 95]. The EDFA amplifier is proving to be of considerable benefit in the amplification of signals along a network path. Its associate, the SLA may have a lower bandwidth ~ 5 THz, but is now finding applications at the transmit and receive end of an optical transmission system. SLAs possess several advantages, amongst them high gain (25dB) with low power consumption and possible monolithic integration with other optoelectronic devices. They can be manufactured as amplifier arrays [Hunziker et al 95] and their single mode wave guide structure makes them suitable for mono mode fibres. Some applications of optical amplifiers are described below.

3.2.1 Receiver Amplifier

Using an optical amplifier prior to signal detection increases the detection sensitivity, particularly for bit rates in excess of 1 Gbit/s. Used in this way it allows for the development of wideband sensitive receivers, which is important for multiwavelength network systems [Fan et al 95].

3.2.2 Inline amplifier

This is particularly applicable for transoceanic cable links. Booster amplifiers in transmission systems are used to boost the optical signal power. Lichtman [Lichtman 95] used a system of 270 EDFAs spaced 33 km apart over 8910 km in a 5 Gbit/s transmission. Although EDFAs are a popular choice for this application the use of $LiF:F_2^+$ and $LiF:F_2^-$ crystals for optical amplifiers has the advantage by allowing insertion into a network with no disconnection of the fibre [Kozlov et al 95].

3.2.3 Wavelength translator

Wavelength translators are components used in reconfigurable wavelength division multiplexing WDM systems [Bray and O'Mahony 96]. TWSLAs operated in saturation allow transmission over different network paths. See section 5.1.3.

3.3 Semiconductor laser amplifiers

3.3.1 FP Basics

Figure 3.1 shows a schematic of a typical SLA based on a normal semiconductor structure as discussed in the section on lasers.

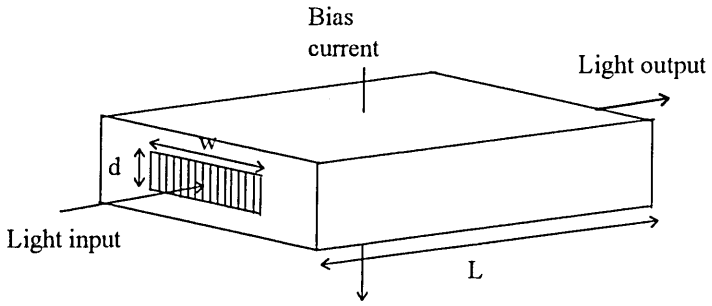

Figure 3.1 Structure of semiconductor laser amplifier.

The shaded region depicts the active area where the majority of the optical signal is confined. The active region is shown with width w, depth d, and length L. The cleaved ends of the device (facets) will possess a natural reflectivity R_1 and R_2 (typically 0.3 for normal lasers) due to the difference in refractive index between the semiconductor and its surroundings which is given by the Fresnel relationship:

$$R = \frac{(N_S - 1)^2}{(N_S + 1)^2} \tag{3.1}$$

where N_s is the refractive index of the semiconductor material (assuming the outer medium is air with refractive index equal to 1). For example $R \approx 0.3$ for a device wth $N_S = 3.5$ i.e. InGaAsP. Guiding of waves along the device is commonly performed using the index method where the active area has a higher refractive index than the surrounding semiconductor material (equation 3.1). Alternatively guiding can be achieved by imposing a gain differential between the active area and the rest of the semiconductor. Consider initially the single pass gain through a semiconductor device with no end reflections given as G_s. A common definition of a FP device is when the factor $G_s = (R_1R_2)^{1/2}$ is close to unity. Bias currents in such a device are set to just below the lasing threshold.

3.3.2 FP Analysis of SLA (Continuous wave)

In a FP cavity the optical signal consists of the superposition of two waves travelling in opposite directions and the phase of the signal needs to be included in the analysis. A travelling wave field inside the amplifier will propagate according to the following differential equation, [Marcuse 83]:

$$\frac{dE}{dz} = \frac{\pm Eg(z)}{2} - i\beta \pm E \tag{3.2}$$

where $\pm E$ is the field travelling in both directions of the amplifier, $g(z)$ the gain coefficient per unit length at position z and β the propagation constant equal to $2\pi N_S z/\lambda$ (note the 2 in the denominator accounts for the field gain being equal to the square root of the power/intensity gain). To solve such an equation, boundary conditions are introduced to describe cavity reflections and transmissions. Figure 3.2 shows a schematic of the fields within a FP device.

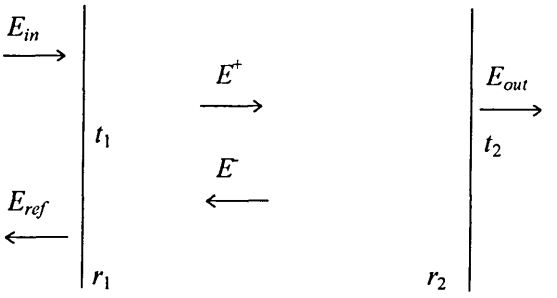

Figure 3.2 Boundary conditions for signal in Fabry Perot device.

An addition to a laser analysis is the inclusion of an input signal field E_{in}, E_{out} is the amplified field and E_{ref} the reflected field. Here boundary conditions are given as:

$$E^+(0) = t_1 E_{in} + r_1 E^-(0) \tag{3.3}$$

$$E_{ref} = r_1 E^-(0) + E_{in} r_1 \tag{3.4}$$

$$E^-(L_{FP}) = r_2 E^+ \tag{3.5}$$

$$E_{out} = E^+(L_{FP})\, r_2 \tag{3.6}$$

where L_{FP} is the length of the device. To solve equation 3.2 a simplification is used in that the gain along the cavity is independent of position and is given as g(z) = g. Equation 3.2 can then be integrated to give [Adams et al 85]:

$$E^{\pm}(z) = K^{\pm} E_0 \exp\left[\pm\frac{gz}{2} \mp iBz\right] \tag{3.7}$$

Applying the boundary conditions to equation 3.7 gives the constants K^+ and K^- and E_{out} resulting in the equation for power gain in a FP amplifier (assuming $R_1 = R_2$ where R (= r^2) is the power reflection coefficient) [Henning et al 85]:

$$G = \frac{(1-R)^2 G_s}{(1-RG_s)^2 + 4RG_s \cdot \sin^2\left(\dfrac{2\pi N_{eff} L_{FP}}{\lambda_s}\right)} \tag{3.8}$$

Here λ_s is the signal wavelength and N_{eff} the effective refractive index of the TWSLA material. In the above analysis the amplifier is assumed to reach steady state conditions, the signal is assumed to occupy one frequency which is at the peak of the amplifier lineshape (see section 2.2.2) and spontaneous emission effects are ignored. The frequency response of an FP cavity from equation 3.8 is uneven and contains ripples due to the occurrence of standing waves at integer multiples of the device length. The ripple depth is measured as the difference between the peaks and is given by :

$$M_r = \frac{1+\sqrt{R_1 R_2}\,G_s}{1-\sqrt{R_1 R_2}\,G_s} \tag{3.9}$$

3.3.3 Travelling wave semiconductor laser amplifier (TWSLA)

With reflectivity at the ends of a semiconductor laser amplifier R_1 and R_2 set to zero in equation 3.8, the power gain reduces considerably to $G = G_s$, i.e. the single pass gain. Without the rapid accumulation of field strength due to multiple reflections the gain in a TWSLA device is lower than that obtained with the FP method. The reduction in gain is compensated somewhat by an increase in bandwidth, reduced sensitivity to temperature variations and a greater tolerance to bias current fluctuations [O'Mahony 88]. In addition it has low sensitivity to signal polarisation and superior gain saturation properties. The main method of reducing end reflectivity is to apply an antireflection coating to the ends of the device. However in practice the facets still retain some reflectivity and in reality TWSLAs are termed near TWSLAs (NTWSLA). With this method, residual facet reflectivities around 10^{-5} are obtainable [Ruiz-Moreno and Guitart 93]. A further advantage obtained with reducing facet reflectivity is that passband ripple is lower. Figure 3.3 shows a typical ripple response for FP and TWSLA devices.

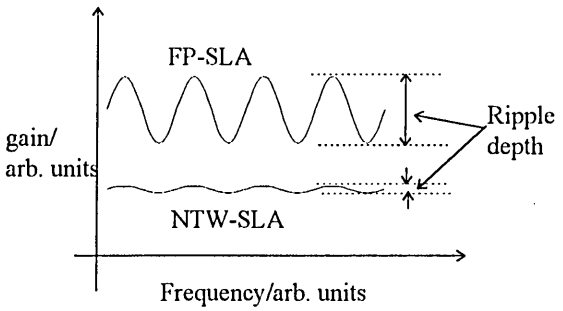

Figure 3.3 Ripple response of FP-SLA and NTW-SLA.

Gain ripple is a function of frequency and results from the frequency dependent term in equation 3.8 Passband ripple proves to be a disadvantage in multi-wavelength systems such as WDM transmission where different channels will receive different amplification due to the uneven response. Multi-wavelength systems utilise the flatter spectral response of TWSLAs as in [Singh et al 96]. However the cost and complexity of producing anti-reflection coatings is high. An alternative method has been developed by Kelly [Kelly et al 96] which uses facets which are cut at an angle to the waveguide direction. This method has produced reflectivities of 10^{-5} with an amplifier gain of 25 dB at a wavelength of 1.55μm

3.3.4 Analysis of TWSLA Continuous wave

Assuming zero reflectivity occurs in a TWSLA then the phase information is not needed. The field equation (equation 3.2) then becomes

$$\frac{dI^{\pm}}{dz} = \pm g(z) I^{\pm} \tag{3.10}$$

which is now described in terms of the signal intensity I. An equation of charge conservation describes the interaction between the signal and carriers in the steady state i.e:

$$P_c = R_{sp} - \Gamma g I / E_P \tag{3.11}$$

where P_c is the pumping term due to the bias current, R_{sp} the spontaneous recombination rate, Γ the confinement factor which describes the fractional intensity coupled into the guided mode and E_p the photon energy of the signal. The simplified boundary conditions are now:

$$I_{in} = I^{+}(0) \tag{3.12}$$

$$0 = I(L) \tag{3.13}$$

The steady state solution for the TWSLA is found by solving equations 3.10 and 3.11 subject to the boundary conditions 3.12 and 3.13.

3.3.5 Noise characteristics of TWSLAs

The origin of optical noise in an optical amplifier is from the spontaneous emission of photons and contributes to the signal to noise ratio in an optical amplifier system. Consider a point at the beginning of a TWSLA. Due to recombination of electrons there is a probability that spontaneous emission will occur and this equals the probability of stimulated emission by a single photon [Yariv 75]. There is also a possibility that this photon will stimulate further emissions and, being of a random nature, this will have no coherence with the signal photon and is therefore a noise process. The propagation equation for the noise power P_n is given as:

$$\frac{dP_n}{dz} = a(n(z) - n_o)P_n(z) + an(z)h\nu \tag{3.14}$$

The first term in the right hand side of equation 3.14 corresponds to amplification of the stimulated emission process and the second term is noise added per unit length. Integrating equation 3.14 over the device length gives the power output due to amplified spontaneous emission (ASE) as:

$$P_{ASE} = (G_s - 1)n_{sp1}h\nu \tag{3.15}.$$

where n_{sp1} is termed the population inversion factor (equal to $n/(n - n_0)$). Any losses along the device are ignored. Spontaneous emission noise is considered to be white with a single sided power spectral density [Singh et al 96]. Figure 3.4 demonstrates the origin of the ASE component. [Tiemeijer et al 96].

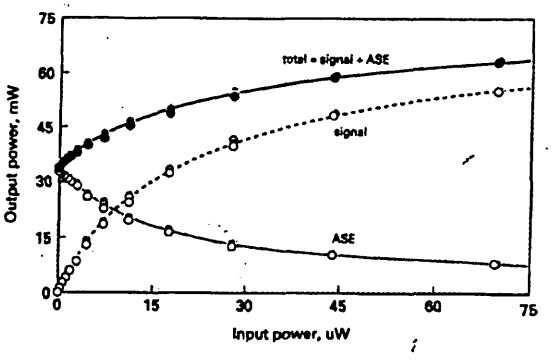

Figure 3.4. Signal and ASE power in a TWSLA. [Teimeijer et al 96]

The ASE power is of the same order as the signal power for low input powers but is reduced at higher powers as the device gain is reduced, as the ASE gain dependence shown in equation 3.15. The signal gain and ASE 3 dB points taken from [Teimeijer et al 96] have similar values (15.6 dBm (36.3 mW) and 15.1 dBm (32.4 mW) respectively). At the photodetector of an optical communication system the ASE will beat with itself and other signals. The noise components are given in Bray [Bray 96] as the mixing of various signals within the detector:

Spontaneous - spontaneous:

$$N_{spont\text{-}spont} = B_e/(B_o)^2 \times (2B_o - B_e) \times (e^2/(hv)^2) \times (P_{ASE}) \qquad (3.16)$$

Spontaneous - signal:

$$N_{spont\text{-}sig} = (4B_e/B_o) \times (e^2/(hv)^2) \times (P_s + \Delta p) \times (P_{ASE}) \qquad (3.17)$$

Shot noise:

$$N_{shot} = 2 \times B_e \times (e^2/hv)(P_s + P_{ASE}) \quad (3.18)$$

Thermal noise:

$$N_{th} = \bar{I}^2_{th} \quad (3.19)$$

where B_e is the electrical bandwidth of the photodetector, B_o the optical filter prior to detection which is to bandlimit the ASE, Δp is the noise power added from previous stages and P_s the signal power.

3.4 Carrier non-linearities in TWSLAs

3.4.1 Intraband and interband transitions

It is convenient to describe the non-linearities associated with SLAs as either interband or intraband, see figure 3.5 which shows the energy bands in a direct bandgap semiconductor.

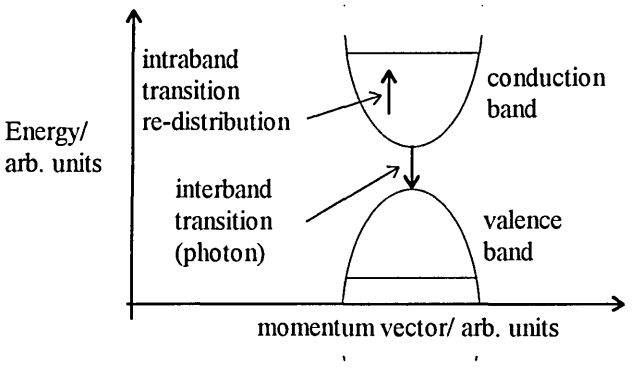

Figure 3.5 Interband and intraband transitions.

Interband non-linearity is concerned with the changes in electron concentration between the conduction band and the valence band within a material. Intraband non-linearity is concerned with the changes in electron energy distributions rather than their numbers. The manner of change is such that the concentration of electrons in the conduction or

valence band remains the same whereas the distribution of electrons within the energy band is altered. These effects are more pronounced in ultrashort pulse amplification (see section 3.7).

3.4.2 Non-linear gain effects

It is instructive initially to consider an absorptive medium (see figure 3.6).

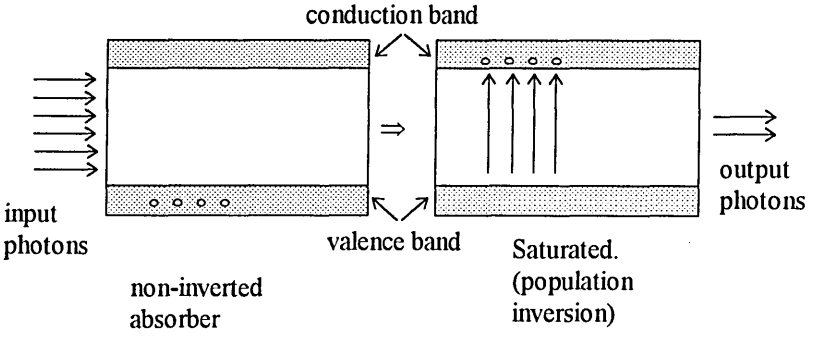

Figure 3.6 Absorption saturation in a semiconductor.

When a strong signal is sent through such a medium absorption immediately takes place with a corresponding increase in the population inversion. A point is reached where the rate the material absorbs energy is less than the power input and saturated absorption occurs. The point to note is that the shape of the signal is changed by the rate of absorption since the leading edge of the signal (which saturates the absorber) will be absorbed more (attenuated) than the trailing edge. Energy transmission is increased in the saturation region due to inverted carriers during the absorption process and distortion of the signal takes place. In an absorber with an energy gap between conduction bands of E_a and an active area A, a common definition of the saturation power is given as [George and McCall 94]:

$$P_{sat} = E_a A/(\Gamma \tau_2 a). \tag{3.20}$$

Saturable amplification is described fundamentally by the same physics as saturable absorption except for a change of sign between the two processes (the signal is now amplified instead of absorbed). In this case the pump(current) will replenish any stimulated emissions in the amplification process. If the pump injects carriers at a rate greater than that used by the signal then the carrier density does not change. If the stimulated emission rate is greater than the pump rate the carriers are reduced and the gain is reduced leading to a gain dependant on signal power given as [Singh 96]

$$G = G_{ss}exp(-(G-1)P_{in}/P_{sat}) \tag{3.21}$$

where G_{ss} is the small signal gain of the amplifier and P_{sat} is defined in equation 3.18 and describes the value for a steady state gain reduction of 1/2. Figure 3.7 shows a plot of gain v output power using equation (3.21), depicting the saturation of gain due to signal power.

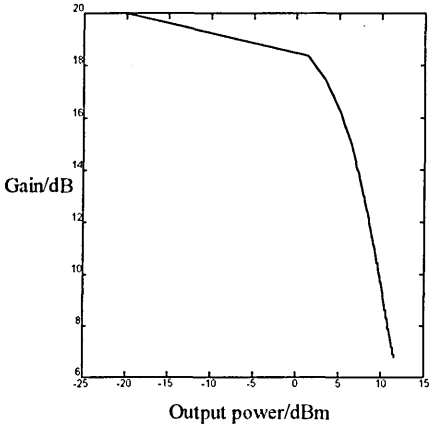

Figure 3.7 Gain saturation in TWSLA.

The saturation is also wavelength dependent [Innoue et al 87] due to the wavelength dependence shown in figure 2.3.

3.5 Picosecond pulse amplification in TWSLAs

With transmission systems demanding data rates in excess of 150 GBit/s (see table 1.2) pulse requirements are for very short duration with high frequency components. The high gain high bandwidth of TWSLAs compared to FP devices is particularly suited to this application. In this section the amplification of pulses with a width of a picosecond or greater are examined. The special treatment required for subpicosecond pulses follows in a later section. The use of TWSLAs for pulse processing has led to a number of applications for their use, e.g. optical sampling [Jinno et al 94], non return to zero (NRZ) to return to zero (RZ) format conversion [Noel et al 95] , logical operations (AND gate) [Nesset et al 95] and address recognition [D'Ottavi et al 95]. These examples highlight the increasing use of an optical amplifier to perform some of the functions on optical signals which were previously the domain of electronic methods.

3.5.1 Pulse response TWSLA (Experimental observations)

3.5.1.1. Regular pulse input at rates > recombination time

Initial investigations of TWSLAs centred around a steady state time response. The first measurements on the dynamic response of a TWSLA were made by Marshall [Marshall et al 87]. The pulses used there had a FWHM of $\approx$ 50 ps which were amplified at low rates (100 MHz) to a peak power of 100 mW. Antireflection coatings were applied to this device which gave facet reflectivities of $\approx$ 0.08%. Even at this low level of reflectivity TWSLAs still exhibit residual cavity modes, in this case ripple depth was 3 dB of the modal gain which peaked at 25 dB. The input consisted of regularly spaced pulses (10 ns apart). Increased pulse repetition rates (2.5 and 5 ns spacing) gave identical gain curves as the 10 ns case. In all instances the pre-pulse carrier density

settles to the zero input value. Further investigations in an experiment by Wiesenfeld [Wiesenfeld et al 88] used pulses considerably shorter (7.9 ps) than before. The pulse separation was above the relaxation time (i.e. a pulse repetition rate of 200 kHz giving a time of 5 μs between pulses). In this case the pulses were characterised by their energies rather than powers. This is more appropriate for widely separated pulses whose effect on the carrier density is independent from adjacent pulses. Pulse saturation power would be misleading with different average pulse powers giving different values of gain saturation. The amplifier device gain is measured against a value of energy saturation which is the value of a single pulse when the gain begins to reduce. Distortionless pulse output was observed when the condition $E_{in} < E_{sat}$ (where E_{sat} is the saturation energy given by P_{sat}/τ_2) was satisfied and no gain saturation occurred. With E_{in} approaching E_{sat} gain saturation was apparent. The pulse input width for increasing energy was kept constant for this experiment therefore increasing the input energy is equivalent to increasing the pulse peak power. The gain v output energy curve was described as linear over a region where $E_{in} << E_{sat}$ with a response given by [Wiesenfeld et al 88]:

$$G = G_0 - 4.34E_{out}/E_{sat}. \tag{3.22}$$

Further experiments on pulse amplification were carried out by Eisenstein [Eisenstein 88] at repetition rates of 4 GHz and 1 GHz where gain compression occurred for the same pulse energy in each case. The recovery time was 250 ps for this amplifier giving independent pulse amplification for both frequencies. Using data rates around the reciprocal of the relaxation time ensures no intersymbol interference occurs between adjacent pulses as each pulse experiences a gain which has fully recovered from the previous pulse, giving a maximum data rate of 4 GBit/s in this case. Figure 3.8 shows

an amplified 4 GHz distortion free pulse which would result in no intersymbol interference [Eisenstein et al 88].

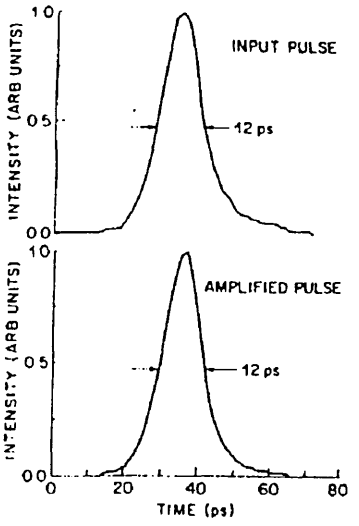

Figure 3.8 Distortion free pulse at low data rate [Eisenstein 88].

The point to note in the above experiments is that operation at data rates higher than $1/\tau_2$ produces identical gain for each pulse even under gain saturation.

3.5.1.2 Modulated pulse input in saturation region

The previous experiments used a periodic pulse input. An interesting feature of dynamic input to TWSLAs is when modulated data is input to the amplifier. It is observed that the power gain can increase momentarily when a signal contains a train of ones interspaced by zeros. The experiment of Ligne [Ligne et al 90] satisfied this condition with pulse rates at 1 Gbit/s and 4.8 G bit/s with τ_2 = 2 ns. A pulse train consisting of 011111010 was input to the amplifier. Common to both data rates the amplifier output was non linear with significant overshoot occurring on the pulse following a series of zeros (bit 2 and 8). Stable conditions of the amplifier were achieved after a series of 1s (bits 2 to 6), (figure 3.9).

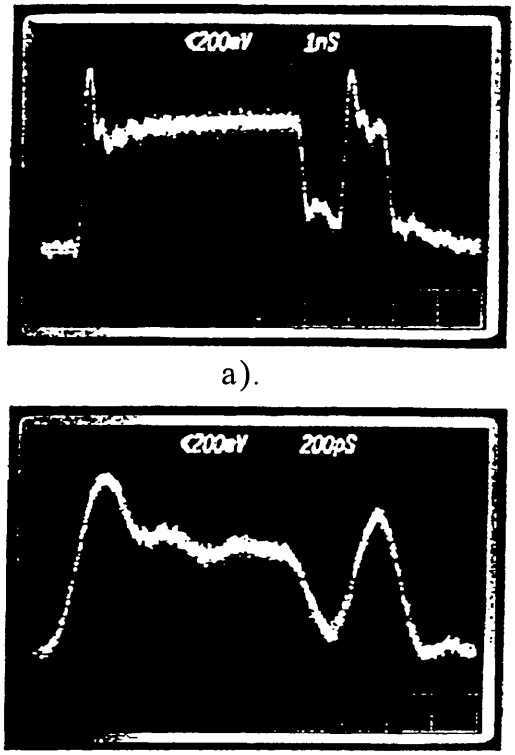

Figure 3.9 High data rate pulses to saturated TWSLA [Ligne 90].

With the lower data rate (1 Gbit/s figure 3.9a) the long period of the first bit allows for stability conditions to be reached over a one data pulse and a longer period for carrier relaxation when a zero is received. Figure 3.9b for a data rate of 4 GBit/s shows the second overshoot is lower than the first, the reason being that the short pulse period requires a larger number of pulses for stability to be reached. If the amplifier was operated in the unsaturated region all bits would receive equal amplification for all data rates. The TWSLA when operated in the saturated region gives an uneven response for different bits of the signal due to the variation in carrier density associated with the saturation region. Similar experiments by Inoue and Yoshino [Inoue and Yoshino 96] have showed pulse distortion is evident for modulated bit rates (7.5 Gbit/s) under gain

saturation of the device, see figure 3.10 which shows pulse distortion in the closed eye diagram.

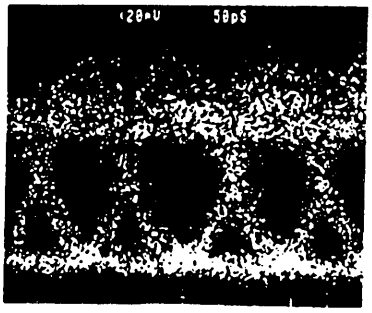

Figure 3.10 7.5 Gbit/s pulse amplification in saturated device [Inoue and Yoshino 96].

In the modulated data rate case it is clear that consideration must be given to the effects of saturation and the timing between data pulses, although the average gain of a train of pulses may yield a certain value a different value occurs for different bits.

3.6 TWSLA Dynamics

3.6.1 Simplifications.

To understand many of the characteristics of pulse amplification e.g. pulse broadening, pulse compression, gain saturation and self phase modulation it is necessary to analyse the dynamics of TWSLAs. The approach is based around the fundamentals of a continuous wave analysis. The previous analysis of TWSLAs described the equations used for continuous steady state analysis (section 3.3.4). For pulse inputs with varying frequencies and bit patterns the TWSLA needs to be described as a function of position and time. This section outlines and justifies the simplifications which can be applied to the analysis for a particular application.

3.6.1.1 Homogenous broadening

A comprehensive rate equation was presented by Marcuse [Marcuse 83] which describes the interaction of light at different frequencies with the conduction and valence band electrons i.e:

$$\frac{dn_v}{dt} = P_c - \frac{n_v}{\tau_2} - A_C S(n_v - n_{ov}) \tag{3.23}$$

where n_v is the density of conduction band electrons and n_{ov} the density of valence band electrons and A_C the stimulated emission coefficient. It is noted that a subscript v occurs throughout which relates to the frequency of the signal within the device. This equation implies that a number of rate equations are required to describe the interaction of a photon at a particular frequency with the carriers. This is of less importance when the photon is from a particular input signal with a defined wavelength such as a continuous wave. More significant in this analysis is the presence of noise in the amplifier or for pulse signals which have a finite bandwidth. The wavelength dependence can be described by a distribution function which describes the fractional interaction of electrons with photons at a particular frequency f_v. The inclusion of a distribution function for conduction electrons gives:

$$D_v = \sum_{v=1}^{N} n_v \tag{3.24}$$

and for valence electrons:

$$D_{ov} = \sum_{v=1}^{N} n_{ov} \tag{3.25}$$

An important consideration of laser amplifier analysis is the broadening of the interaction of photons and electrons which will be described . In experiments by

[Mukai 87] the gain spectrum for TWSLAs was examined. The work highlighted an important factor concerning these devices. It was found that the amplifier had a frequency response function $G = G_o(\omega_s, S_I)$ where ω_s is the signal frequency and S_I is an additional strong light signal at a single wavelength input to the TWSLA. The gain function at a particular value of current gave a similar shape to one with a higher current and the signal S_I. Figure 3.11 illustrates the TWSLA spectra [Mukai et al 87].

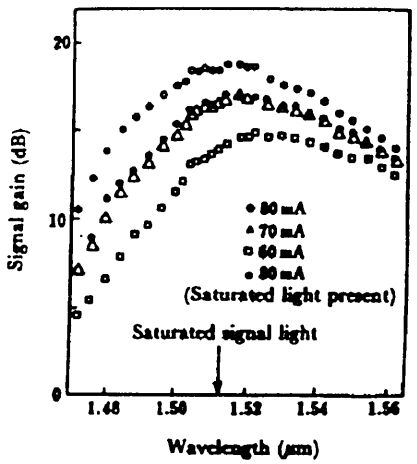

Figure 3.11 Gain spectra of TWSLA [Mukai 87].

Note the plots Δ which indicate one signal source and ● which also includes a signal at 1.51 μm. The overlap of the two plots indicates that light input of any frequency will interact with electrons in a similar way as current input does. Returning to the rate equation term for electrons the distribution functions can now be normalised to one i.e.:

$$\sum_{v=1}^{N} n_v(n_{ov}) = 1 \tag{3.26}$$

for both conduction and valence band electrons. The phenomenon of spectral hole burning in which a photon at a particular wavelength can "burn" a hole in the electron

structure is precluded and equation 3.23 is reduced essentially to a single equation for all frequencies [Gillner 92].

3.6.1.2 Electronic band structure

Homogenous broadening introduces one of two approximations to the non-linear analysis. A second simplification involves the concept of a band structure. Energy levels in a semiconductor exist in bands (i.e. the term conduction band) [Brian 90]. Relaxation times within the bands in which the electrons are distributed are very fast with times of the order of 50 fs [Gomatam and DeFonzo 90]. The response of fast intraband times is less pronounced as the input pulse moves into the picosecond region [Hong et al 94].

3.6.2 Equations for TWSLA dynamic analysis

The major difference in the analysis of dynamic gain non-linearities and any effects due to phase, velocity and group velocity dispersion are that the pulse widths are assumed long and device lengths short so that the latter effects can be ignored. These effects tend to dominate more in subpicosecond amplification [Hall et al 1990]. The task now is to develop a differential equation for a signal with intensity $I(z,t)$ travelling through an amplifier with an inverted population electron density given as $n(z,t)$. Refer to figure 3.12 which describes the propagation of a signal through a segment of a TWSLA.

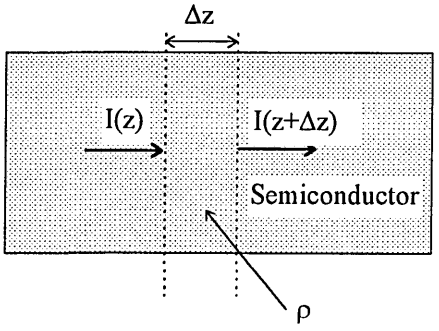

Figure 3.12 Diagram for the calculation of dynamic signal input to a TWSLA.

A simple energy conservation equation then assists in describing the effect and is written by considering a short length segment Δz within the amplifier. The following statement can be written:

Rate of change of stored energy in the segment Δ_s	=	Power into one end of segment - power out of other end of segment.	+	Net rate of stimulated emission within the segment

Algebraically this may be written as:

$$\frac{\partial E_{tot}(z,t)}{\partial t} = \partial I(z,t)A_d - \partial I(z+\Delta z,t)A_d - \sigma n_i(z,t)I(z,t)\Delta z A_d \tag{3.27}$$

where E_{tot} is the total energy within the segment, A_d the area of the segment, σ the stimulated gain coefficient. If ρ is the energy density of the device the following equation can be written:

$$\frac{\partial \rho A_d \Delta z}{\partial t} = \left[\partial I(z,t) - \partial I(z+\Delta z,t) - \sigma n(z,t)I(z,t)\Delta z\right]A_d \tag{3.28}$$

Now if the photons move with a velocity of c_d then:

$$I(z,t) = c_d\sigma \tag{3.29}$$

giving:

$$\frac{\Delta z \partial I(z,t)}{\partial t}\frac{1}{c_d} = I(z,t) - I(z+\Delta z,t) - \sigma n(z,t)I(z,t)\Delta z \tag{3.30}$$

Taking the partial differential coefficient of equation 3.26 with respect to z gives

$$\frac{\partial I(z,t)}{\partial t}\frac{1}{c_d} + \frac{\partial I(z,t)}{\partial z} = \sigma n\ (z,t)I(z,t) \tag{3.31}$$

which is the propagation equation for the movement of photons within an amplifying medium with an inverted population.

A simplified carrier density equation can be written as:

$$\frac{\partial n(z,t)}{\partial t} = \frac{\Gamma a}{E_P}(n(z,t) - n_o)I(z,t). \tag{3.32}$$

Equations 3.31 and 3.32 form a set of coupled differential equations which describe the evolution of a time and space varying input to a semiconductor device.

3.6.3 Pulse propagation dispersive effects

It is now possible to generate ultra short pulses (less than a picosecond) particularly in modelocked lasers [Nakazawa and Yoshida 96] which can be amplified to large energies in laser amplifiers [Tang et al 96]. This section introduces some of the fundamental properties of linear pulse propagation which are of concern when propagating through dispersive media [Radzewicz et al 96] and the amplification of ultrashort pulses [Kao et al 96]. The concepts include phase and group velocity, and group velocity dispersion.

3.6.3.1 Dispersive systems analysis

Gaussian pulses provide a mathematically convenient method of analysing dispersive systems and an example of such a pulse can be written as:

$$E_d(t) = \exp(-a_1 t^2)\exp j(w_o t + b_1 t^2) \tag{3.33}$$

where ω_o represents the carrier frequency (optical frequency) a_1 describes the Gaussian pulse shape and b_1 the frequency chirp present. The instantaneous intensity of such a pulse can be written as:

$$I(t) = |E_d(t)|^2 = \exp(-2at^2) \tag{3.34}$$

If $a_1 - jb_1$ in equation 3.33 is written as Γ_1 then the Gaussian pulse spectrum is given by:

$$\tilde{E}_d(\omega) = \exp\left[\frac{(\omega - \omega_o)^2}{4\Gamma_1}\right]. \tag{3.35}$$

If the propagation constant of a travelling wave system is now introduced as:

$$\beta = 2\pi N_d/\lambda \tag{3.36}$$

where N_d is the refractive index of the medium of which the pulse is propagating at a wavelength λ, β is actually a function of frequency and can be written as a truncated Taylor series containing terms up to the second order [Radzewicz 96],

$$\beta(\omega) = \beta_o(\omega_0)+\beta_1\times(\omega-\omega_0)+1/2\ \beta_2(\omega-\omega_0)^2 \tag{3.37}$$

if ω_0 is a centre frequency value of narrow band signals then:

$$\beta_1 = d\beta(\omega)/d\omega \tag{3.38}$$

and

$$\beta_2 = d^2\beta(\omega)/d\omega^2 \tag{3.39}$$

both β_1 and β_2 are evaluated at $\omega = \omega_0$. The propagation constant at a distance z is $\beta(\omega)z$ which modifies equation 3.33 to:

$$E_d(t,z)= \exp j(-\beta(\omega)z).\ \exp(-a_1t^2).\ \exp j(w_ot+b_1t^2) \tag{3.40}$$

taking the inverse fourier transform of $E_d(z,\omega)$ gives:

$$E_d(z,t) = \int_{-\infty}^{\infty}\exp\left[\frac{-(\omega-\omega_0)^2}{4\Gamma_d(z)} - j\beta_1 z(\omega-\omega_0) - j\beta_0(\omega_0)z\right]\exp j\omega t.d\omega \tag{3.41}$$

where Γ_d is the modified Gaussian pulse parameter given by:

$$\frac{1}{\Gamma_d(z)} = \frac{1}{\Gamma_1} + 2j\beta_2 z \tag{3.42}$$

It is possible now to bring out terms $\omega_o t$ and $\beta(\omega_o)z$ to the front of the integral in equation 3.41:

$$\begin{aligned} E_d(z,t) &= \left(\frac{\exp j(\omega_o t-\beta(\omega_c)z}{2\pi}\right)\times \\ &\int_{-\infty}^{\infty}\exp-\frac{-(\omega-\omega_o)^2}{4\Gamma_d(z)}.\exp j(\omega-\omega_0)(t-\beta_1 z)d(\omega-\omega_o) \end{aligned} \tag{3.43}$$

Note: the change of variables $\omega \equiv \omega - \omega_o$, and $t \equiv t-\beta_1 z$. Comparing with equation 3.35 the integral gives a Guassian pulse with modified shape $\Gamma_d(z)$ [Siegman 86]:

$$E_d(z,t) = \exp j(w_o t - \beta(w_o)z).\exp(-\Gamma_d)(t - \beta_1 z) \quad (3.44)$$

From equation 3.44 the first exponential is identified as the phase velocity and the second exponent the group velocity. The phase velocity determines the phase of the carrier wave as it propagates over a distance z, the group velocity determines the delay of the pulse envelope at a distance z. More important is the group velocity dispersion (GVD) determined by the parameter $\Gamma_d(z)$. Hence, from equation equation 3.42, pulses transmitted over a medium are affected in shape by the parameter β_2. It is therefore necessary to appreciate the value of the dispersion parameters in systems which possess a variable value of β_2. In the previous description β relates to optical fibre transmissions. GVD in an optical fibre produces the effect known as pulse broadening [Kao 96] whereby the spectral wings of a pulse propagate at different speeds from the centre frequency [Agrawal 91]. A detrimental effect is intersymbol interference as pulses overlap each other over long fibre systems. Figure 3.13 shows how a broadened pulse can overlap into an adjacent pulses.

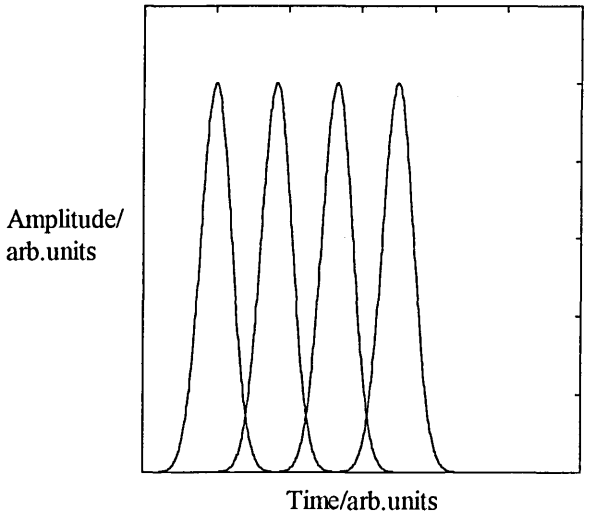

Figure 3.13. Broadened Gaussian pulse.

A typical measure of dispersion is the length of transmission possible before the FWHM of a pulse increases by $\sqrt{2}$ of its initial value. Typically for transmission through glass fibres with a refractive index n = 1.5 the $\sqrt{2}$ broadening lengths range from 1 cm for a 100 fs pulse to 10 km for a 100 ps pulse

3.6.3.2 Pulse broadening and gain dispersion in amplifying devices

A semiconductor laser amplifier will possess a finite band width and thus a frequency dependent gain [Eisenstein and Jopson 86]. The gain curve of such a device is described by a Lorentzian atomic type transition with the following format (see section 2.2.2)

$$g(\omega) = \frac{g_o}{1+\left[\frac{2(\omega-\omega_0)}{\Delta\omega_0}\right]^2} \tag{3.45}$$

which can be approximated to the following [Agrawal 91]:

$$g_o - g_o\left(\frac{2}{\Delta\omega_0}\right)^2 \times (\omega-\omega_0)^2 \tag{3.46}$$

where $g(\omega)$ is the frequency dependant gain and is known as the gain dispersion, g_o is the gain at the centre frequency , ω_o the centre frequency and $\Delta\omega_0$ the line width of the atomic transition system. When subjected to a gaussian input pulse with initial parameter Γ_0 the modification after propagating through an amplifier a distance z is [Siegman 86]:

$$\frac{1}{\Gamma(z)} = \frac{1}{\Gamma_0} + \frac{16 g_0 z}{\Delta\omega_0^2} \tag{3.47}$$

The net result is broadening of an optical pulses after propagating through an amplifier with a finite bandwidth. As an example of pulse broadening in an atomic transition consider a pulse with a Gaussian parameter $\Gamma_0 = a_0$ (no initial chirp , $b_0 = 0$) input to a system with a finite bandwidth. The gain dispersion equations 3.46 and 3.47 convert to the pulse width broadening equation [Siegman 86]:

$$\tau_p^2(z) = \tau_{po}^2 + \frac{(16\ln 2)\ln G_0}{\Delta\omega_c^2} \tag{3.48}$$

where $G_0 = \exp(2g_0 z)$ (the gain after two passes through the amplifier at the centre frequency), τ_{po} the initial pulse width and τ_p the pulse width after propagating a distance z. With an amplifier of gain (multipass) 10^5 and linewidth frequency bandwidth 120 GHz then $\tau_p^2 = \tau_{p0}^2 + (15\text{ ps})\times\tau_p^2$ which indicates that an ideal delta function at the input will broaden to a 15 ps pulse at the output. A 50 ps input pulse will broaden to $\sqrt{(50ps)^2 + \approx (15ps)} \approx 52ps$. The above analysis shows that GVD is more significant with decreasing pulse width and increasing device length [Agrawal 91].

3.7 Ultrashort Pulse Amplification In TWSLAs

The amplification of ultrashort optical pulses in semiconductor laser amplifiers has been the subject of considerable research in the previous years [Delfyett et al 91], [Uskov et al 94], [Lenz et al 96] and [Juodawlkis et al 96]. Their possible applications to high speed communication and logic systems are increasingly being recognised. For pulses which are in the range of tens of picoseconds the results are well recognised and theoretical analysis have been developed (see chapter 7).

3.7.1 Pump probe method.

The mechanism for the study of ultrashort pulse amplification uses a pump probe signal input which will be described here for reference. Pump probing is an experimental method for analysing the dynamics of optical systems. The pump consists of a short duration pulse injected into the laser/laser amplifier, the photon density is usually in the range of that for lasing to occur. A second pulse, the probe, with a much smaller intensity

than the pump pulse is injected into the device after a certain time delay and is assumed to have a negligible effect on the carrier density. A polariser at the output separates the probe beam which is detected by a photodiode. The delay between the pump and probe is the independent variable and the intensity of the probe after passing through the device is the dependent variable in the analysis. Figure 3.14 shows a schematic of the set up commonly used.

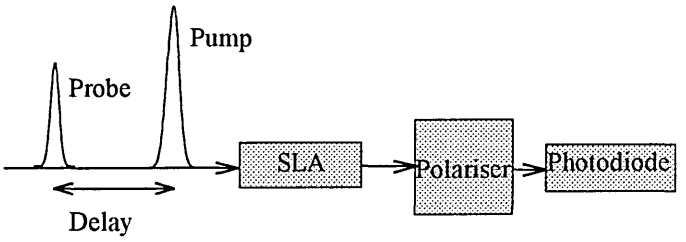

Figure 3.14 Pump probe experimental set up.

3.7.2 Temporal response

Early experiments on subpicosecond pulse dynamics were performed on GaAlAs diodes by Stix et al [Stix et al 86]. In this experiment a dye laser was pumped by a krypton laser where 8 ps pulses were reduced to 0.4 ps using 35 m of polarising preserving single mode fibre. The outcome of the experiment was a noticeable rapid decrease in the device transmission with a fast recovery of the order of 0.9 ps (see figure 3.15). Further experiments on fast pulses by Hall et al [Hall et al 90] yielded an ultrafast component in InGaAsP optical amplifiers not noticed previously. They were able to identify two components in their data corresponding to time constants of $\approx$ 650 fs and 200 fs.

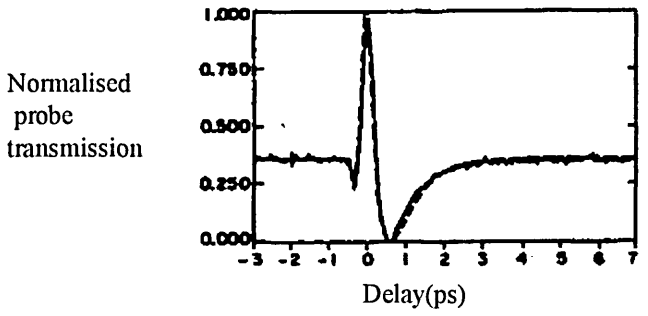

Figure 3.15 Pump probe transmission of 180 fs pulses. [Hall 90].

The transmission also has the long lasting component attributable to carrier recombination.

3.7.3 Gain saturation.

The appearance of these components led to intensive effort on subpicosecond gain dynamics in optical amplifying devices. The dependence of the gain dynamics on pulse widths had not been studied until Lai et al [Lai et al 90] measured the gain saturation properties of a laser amplifier (InGaAsP). The gain response was measured for different pulse widths over a range of 15 ps to 150 fs with a separation between pulses of 10 ns which is considerably longer than the slow population recovery normally associated with InGaAsP TWSLAs. Each pulse received high gain simulating the effect of a single pulse input. They produced autocorrelation traces of the pulse output which gave no visible indication of distortion even under saturation conditions. The interesting feature to evolve from these experiments was from the gain characteristics. The gain for small signal values was approximately equal for varying pulse widths. For higher values of output energy it was apparent that the smaller pulse saturated the TWSLA at a lower value, the 3 dB gain reduction was approximately 40 fJ and 150 fJ for 15 ps and 150 fs pulses respectively. In common with previous experiments fast components were

identified using pump probe measurements. The speed of the responses in this experiment were fitted to experimental data to be 700 fs and an additional ultrafast component at 250 fs.

3.7.4 Analytical description of gain saturation of ultra-short pulses

Concerning the slower component the mechanism is now being established as carrier heating [Hong 94]. To explain the carrier heating process the semiconductor material is assumed to attain an elevated lattice temperature with signal input. Two methods can introduce this effect: stimulated emission of below average energy value electrons and free carrier absorption. A reduction of gain follows an increase in lattice temperature as less carriers are available for stimulated emission gain. The heated carriers will cool back to the lattice temperature when the signal has propagated on a time scale comparable with pump probe experiments. Note the gain dynamics associated with carrier heating have a sign which is always the same and do not follow the region in which the amplifier is operating (absorption, gain or transparency). Uskov et al [Uskov et al 92] has developed a differential equation to describe the carrier heating effect and related this to the gain equation of semiconductor devices via the carrier temperatures. The equation is:

$$\frac{\partial Ti}{\partial t} = h_i\left(\mu_i - E_i + \frac{\beta_i}{g}h\omega_0\right)v_g S - \frac{T_i - \mathrm{T}_c}{\tau_h, i} \tag{3.49}$$

where $i = c,v$ are subscripts for conduction and valence band electrons T_c is the electron temperature, T_v the hole temperature, T_L the lattice temperature, β_i the free carrier absorption coefficient and $h\omega_0$ the photon energy. If U_c and U_v represent the energy density of electrons and holes, the other parameters in equation 3.49 are:

$$\mu_i = (\partial U_i/\partial n)_{Ti} \tag{3.50}$$

and:

$$h' = (\partial U_i/\partial T_i)_n, \tag{3.51}$$

E_i is the carrier energy (measured from the band edge). Equation 3.49 accounts for carrier heating through carrier heating and stimulated emission (see figure 3.16).

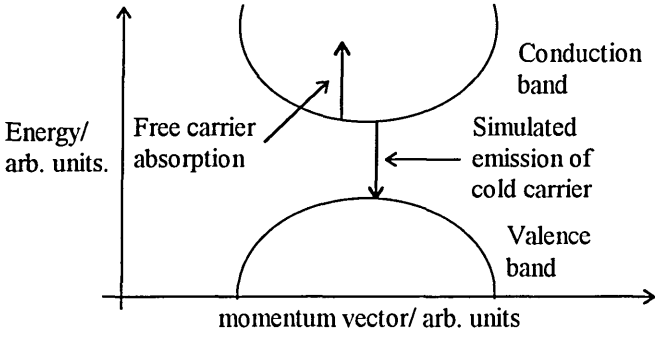

Figure 3.16 Carrier heating processes.

Stimulated emission removes electrons near the band edge which are termed cold carriers (low band energies) at energies E_c and E_v and as μ_i (characteristic energy) $> E_i$ carrier heating occurs. In free carrier absorption carriers are transferred to higher energies within the band increasing the total energy density. The carriers thermalise (i.e. they assume Fermi-dirac distributions through intraband scattering). Cooling of carriers is through the second term on the right hand side with a time constant τ_h. An accompanying gain expression can be written as:

$$g \approx (g_0 + g_N \Delta n + g_{TC} \Delta T_c + g_{Tv} \Delta T_v) \frac{1}{1 + \varepsilon_{shb} S} \tag{3.52}$$

where g_0 is the zero signal gain g_N carrier density gain coefficient, n_b the carrier density with zero input signal, $\Delta n = n - nb$, $\Delta T_i = T_i - T_L$. ε_{shb} is a non linear coefficient to account for spectral hole burning which is a process whereby a signal at a specific energy

creates a dip in the spectral characteristics. The lattice temperature T_L will attain a higher temperature than the conduction and valence band electrons. Consequently g_{Tc} and g_{Tv} will have negative values. A reduction in gain thus occurs. Using the temperature equation (3.49) the gain equation (3.52) a rate equation (3.32) and a propagation equation (3.31) the amplification due to ultrashort pulses can be computed. The results of such simulations are shown in figure 3.17 for pulse duration 10 ps (upper curve) 100 fs (lower curve). The lower saturation energy of the shorter pulse can be identified.

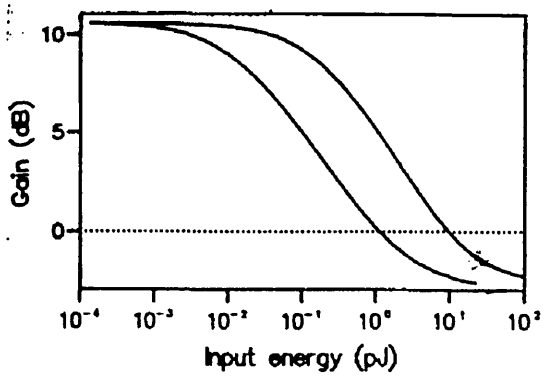

Figure 3.17
Gain of TWSLA energy with different pule width input.[Uskov et al 92]

The above analysis provides an account of the gain saturation process of ultratfast dynamics and shows pulse width dependence on saturation. The dynamics of the process have also been studied comprehensively in [Mark and Mork 92] with a theoretical model showing ultrafast components as well as the fast component due to carrier heating.

3.8 Summary

This chapter has gone some way towards describing semiconductor laser amplifiers for use in communication systems. Architectures of amplifiers discussed are divided into

two types: FP and travelling wave with no distinct line between the two types. Signal inputs range from continuous wave to quasi-continuous through to pulsed operation. Analysis of noise due to spontaneous emission for the travelling wave cases is described. Phase and group velocity is discussed with a derivation of group velocity which can be utilised in systems with atomic resonances present. Particular emphasis is placed on ultrashort pulses. It is found that significant departure from previous dynamics occurs with this fast mode of operation. In particular, two time constants are evident which are described as an ultrafast and a fast component. An analysis developed to account for carrier heating is presented together with the differential equations which model the gain saturation properties due to different pulse widths. The inclusion of faster time constants in TWSLAs is important for high data rate systems where sub-picosecond pulses are used.

Chapter 4.

Optical switching and routing

4.1 Introduction

One of the most important areas for study in modern optical communication systems currently is the utilisation of the fibre capacity. Optical signals may be transmitted at different wavelengths and/or they may be separated in time. This chapter will look at the various methods of switching and routing of wavelength and time dependant channels. Popular structures for switching and routing are based around interferometers, directional couplers, waveguide digital optical switches (DOS) and mechanical reflection devices. Within these architectures, various physical mechanisms allow the switching of an optical signal, including: sound waves, electric field, mechanical switching and controlling light signals.

4.2 Mach Zender Interferometers

A typical Mach Zender device is shown in figure 4.1.

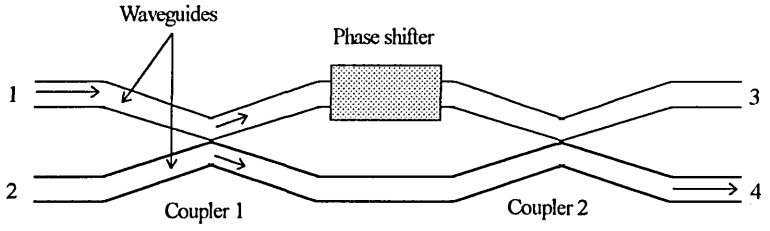

Figure 4.1 Mach Zender interferometer.

The waveguiding in figure 4.1 consists of two optical fibres with coupling formed by placing the waveguides in close proximity to each other. The first coupler passively splits the power of the two signals equally into the two guides. To operate the Mach Zender interferometer a phase shift has to be imposed on the signal passing through the phase shifter arm. When a phase shift of π is imposed by the phase shifter on the signal, transmission (after interfering at port coupler 2) is via port 4. Port 3 output occurs when the phase shifter phase is zero and both arms undergo equal phase shift. The switching speed of the switch is determined by how fast the phase shift can be turned on and off at the phase shifter. One of the major disadvantages of Mach Zender devices is the difficulty in manufacturing devices with equal length arms. Using fused fibre technology for the waveguides, the problem can be overcome somewhat by manufacturing the device on similar lengths of fibre and forming the couplers at two points on the fibre by fusion. Initial investigations on this configuration have been performed by Shipley [Shipley et al 87]. The switch configuration in figure 4.1 was used with a different component for the phase shifter. The methods of producing the phase shift are outlined in 4.2.1. - 4.2.4.

4.2.1 Thermo-optic

By heating the fibre in one arm of the switch a phase shift ϕ is produced which obeys the following differential equation:

$$\frac{d\phi}{l_f dT} = k\left(\frac{n_f}{l_f}\frac{dL}{dT} + \frac{dn_f}{dT}\right) \tag{4.1}$$

where l_f is the heated length of fibre, n_f the fibre index and k the propagation constant. With electro resistive heating producing the thermal effect the power output of the switch follows a periodic response given by:

$$P_o = P_i cos^2(\pi P/2P_\pi) \tag{4.2}$$

where P_π is the electric power required for a π phase shift. Switching speeds were slow due to the long time constant of the heating effect. Modulation frequencies of ≈ 25 Hz were achieved with a heating power of 25 mW.

4.2.2. Stress-optic phase shifter

This method introduces a differential phase shift by longitudinally stressing the fibre in one arm. The phase shift $\Delta\phi$ introduced by a force F acting over a fibre length L and cross section A can be derived from the following equation:

$$\Delta\phi = \frac{\beta FL}{AY}\left(1 - \frac{n^2}{2}((1-\mu)P_{12} - \mu P_{11})\right) \tag{4.3}$$

where P_{11} and P_{12} are Pockels coefficients, μ Poisson's ratio, β the optical propagation coefficient and Y the Young's modulus for silica. The phase shift obtained for this method is slow due to the mechanical nature of the method and its use is restricted to the routing of signals.

4.2.3 Electro-optic method

A recent electro-optic method of phase shifting has been demonstrated by Wooten [Wooten et al 96] which uses $LiNbO_3$ waveguiding technology and switching performed by an electrical signal. See figure 4.2.

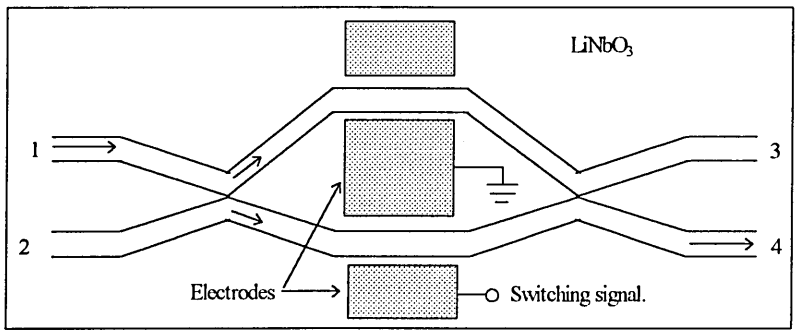

Figure 4.2 Electro-optic Mach Zender interferometer.

This device also possesses wavelength selectivity and can switch signals with a pass band of ≈ 0.4 nm, an insertion loss of 19 dB and a crosstalk of less than -22 dB. The arms of the device are manafactured with different propagation lengths with a signal path difference of ΔL. The frequency dependent output is due to the unbalance and is given by:

$$T = \cos^2[\pi/2(\nu/\Delta\nu + V/V_\pi)] \tag{4.4}$$

where V_π is the voltage required for switching to occur and the frequency spacing is given as:

$$\Delta\nu = c/2\pi N_s \Delta L \tag{4.5}$$

where N_s is the refractive index of the $LiNbO_3$ substrate. Switching speeds of this device gave an improvement over previous methods but were still limited to 20 MHz However sub-picosecond speeds using this method were proposed by [Wooten et al 96] with optimisation of the switching electronics. The switching voltage was 7.6V.

4.2.4. TWSLA devices

A novel type of all optical Mach Zender device incorporating an TWSLA has been demonstrated by Kang [Kang et al 95]. In each arm of the interferometer a TWSLA is placed asymmetrically with respect to the other (see figure 4.3).

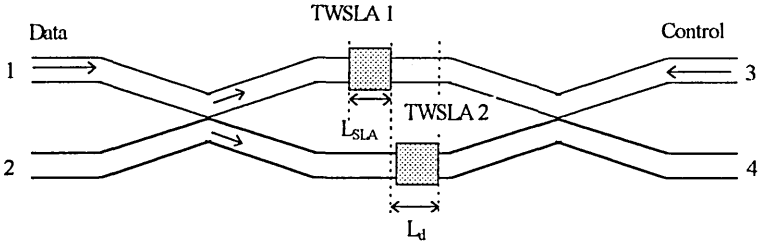

Figure 4.3 Asymmetric TWSLA Mach Zender device.

An additional control signal is fed into port 3 of figure 4.3. The control pulse reaches TWSLA2 in the lower arm first which changes the optical property of TWSLA2 inducing a change in its refractive index and hence the phase of a signal propagating through the device. This switches the signal to port 4 when the phase shift of the TWSLA2 equals π. The control pulse reaches TWSLA1 in the upper arm after a time delay L_d/c given by the asymmetry of the TWSLAs and switches the pulse to port 3 when TWSLA1 has a phase change of π. An advantage of this configuration is that the control and data signal which move in opposite directions can operate with identical wavelength and polarisation with no discrimination needed. The resolution of the switch is related to the length and refractive index of the TWSLA (L_{SLA}, N_{SLA} respectively) and is given by $2L_{SLA}\,N_{SLA}\,/c$. For this experiment a switching speed of $2\times500\times10^{-6}\times3.3\,/3\times10^{8}$ = 11 ps was obtained. The time required before switching can be performed again is determined by the relaxation time of the TWSLA and was found to be 1 ns with a contrast ratio between the on and off state of 5 : 1. This configuration permits integrated assembly and has been demonstrated in a 4×1.5 mm device by [Strass 96]. This had switching speeds of 20 Gbit/s with an extinction ratio of 10 dB. A similar device (size 9 ×1.3 mm) [Leuthold et al 96] produced an extinction ratio of 20 dB. Note that this device also had an overall gain of ≈ 5 dB (which is a feature of this configuration) compared with the previous Mach Zender devices which exhibited an overall insertion loss for the data signal.

4.3 Directional Coupling.

4.3.1 Semiconductor directional couplers

Directional couplers consist of closely spaced waveguides which couple light through their overlapping evanescent fields or mode tails (inset figure 4.4). These devices are of current interest and can be implemented using InGaAsP waveguiding technology making them suitable for integration. Figure 4.4 depicts such a device.

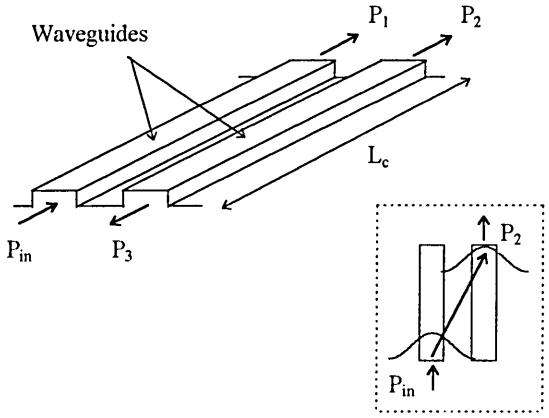

Figure 4.4 Directional Coupler.

The input signal cross couples signal P_{in} to P_2 when:

$$L_c = \pi/4\kappa \tag{4.6}$$

and splits equally when:

$$L_c = \pi/2\kappa. \tag{4.7}$$

where L_c is the waveguide length and κ is a coupling coefficient of the device. A device which can selectively filter and reflect a particular wavelength via P_3 was demonstrated by Alferness [Alferness et al 88] using a Bragg grating placed at the output port which is tuned to the reflected wavelength of the device. This device has a fixed bandpass spectrum dependent on the Bragg wavelength. An enhancement on this technique using

the concepts of a grating assisted coupler was provided by selectively tuning the switch electronically [Shibata et al 96] (see figure 4.5).

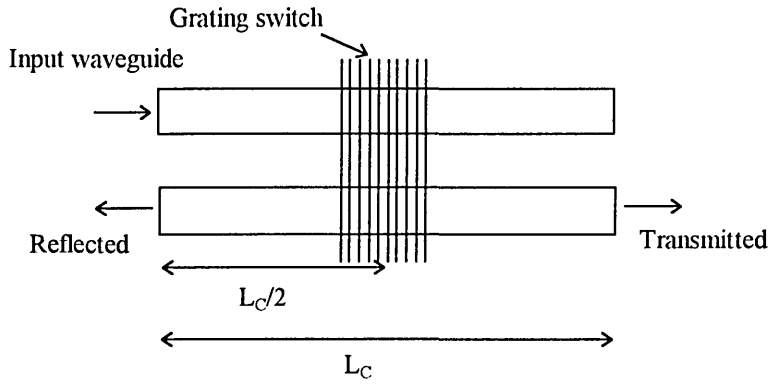

Figure 4.5 Wavelength selective directional coupler.

It is a monolithic device and has a waveguide structure which will allow the integration with other devices such as laser diodes, photo-detectors and optical switches. Wavelength routing is provided by a waveguide system which is dependent on the current injected into the device which follows the simple relationships $\lambda_B = k_I I^{1/2}$, and $\lambda_B = k_n n$ where λ_B is the Bragg wavelength, k_I and k_n are constants of the device and I the current. Shibata [Shibata 96] used this configuration to demonstrate a wavelength selective router. The device reflects signals according to figure 4.6a and transmits signals as in figure 4.6b. Switching times obtained were 1 ns.

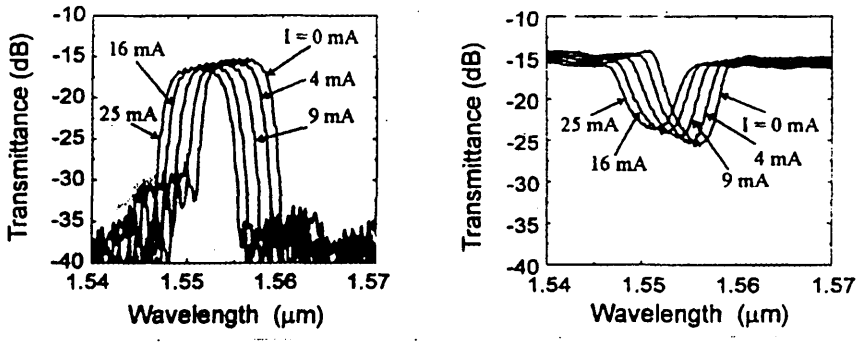

Figure 4.6 Reflection and transmission of wavelength router.

For example in a 1 × 2 device when two signals are input to the device at 1.549μm and 1.555μm and zero current the 1.555μm signal is reflected and the 1.549μm signal transmitted. A control current of 25 mA input to the grating would route the signals to the opposite ports.

4.3.2 Thermo-optic switching directional couplers

Polymer waveguide technology is now considered to be a highly attractive technology. It is a low cost method of producing thermo-optically controlled switches and possesses a number of advantages including low crosstalk, low switching power polarisation and wavelength independence and is insensitive against switching bias and working temperature. Figure 4.7 shows a typical device.

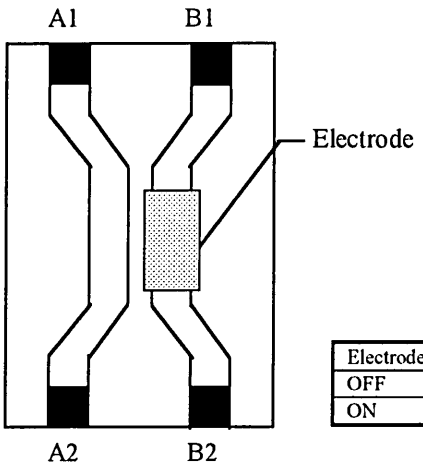

Electrode	Signal
OFF	A1 to A2, B1 to B2
ON	A1 to B2, B1 to A2

Figure 4.7 Thermo-optic directional coupler.

A 2×2 switch was demonstrated by Keil et al [Keil et al 95]. Operating at a wavelength of 1550 nm the switch uses low cost polymethyl methacrylate (PMMA) technology. A voltage is applied to the heating electrode to switch the signal paths as shown in figure 4.7. Power consumption is around 30 mW (0.5V, 60 mA) and the extinction ratio is 32 dB. Switching times are limited to around 1 ms.

4.4. Digital Optic Switch

One of the main features for realising the DOS was polarisation independent switching for the uncontrolled state of polarisation of incoming light when non-polarising maintaining fibre is used. A comparison of DOSs and directional couplers is given in table 4.1.

Type of switch	Directional coupler	Digital optical switch
Principle	Interferomic device	Mode converter
Main advantages	No extra loss	Polarisation independent 3 dB splitter.
Main drawbacks	Polarisation dependant Optical bandwidth limited.	Compromise between angle and required index change.

Table 4.1 Comparison of directional coupler and DOS.

The technique upon which the DOS is based is known as the vanishing waveguide method using a 'Y' configuration (figure 4.8).

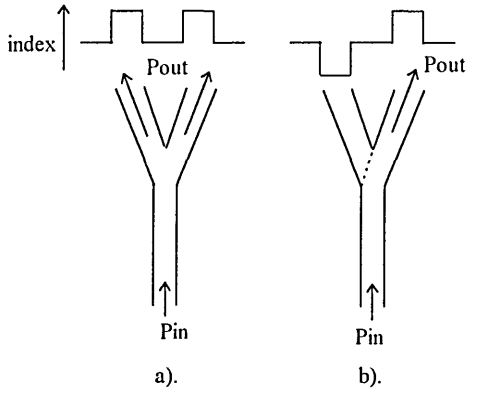

Figure 4.8 Digital optical switch.

In the state shown in figure 4.8a the input signal splits equally between the two output guides. Raising the refractive index of one guide with respect to the other guide switches the input power over to one guide (figure 4.8b).

4.4.1. Semiconductor DOSs

Yanagawa et al [Yanagawa et al 90] constructed a DOS using GaAs/GaAlAs technology where the output guides are built around a *pn* junction. Forward biasing one of the output guides gives a carrier density change equal to:

$$N = (I\tau w L)/e \qquad (4.8)$$

where I is the injected current, τ the carrier lifetime, e the electron charge, t the thickness of the n layer in which the pn junction is diffused, w waveguide width and L the electrode length. This directs the signal to the other output by raising the refractive index of the switched section. The state as in figure 4.8a is obtained with zero current to the device. Switching times obtained with this device were 10 ns with a crosstalk of -20 dB and currents of 280 mA and 340 mA for 1300 nm and 1550 nm wavelengths respectively. Reported use of an alternative method using silicon DOSs have realised switching times of 200 ns. [Liu et al 94]. The carrier non-linearity in a semiconductor is a promising mechanism for an optical switching devices. However because of the finite relaxation time (as discussed in section 2.2.2) the recovery time of these devices is relatively slow. The switching time of a device presented in [Yanagawa et al 90] is limited to a speed of $\approx$ 1.1 GHz. Various attempts to overcome this have been proposed and some are described below.

(i) ***sweeping out the photo generated carriers from the active area***

LiKamWa and Miller [LiKamWa and Miller 91] demonstrated that the relaxation time can be reduced from 1.5 ns to 550 ps by sweeping out photo generated carriers in a semiconductor with the application of an electric field. An alternative technique combines the architecture of a 'Y' junction waveguide and an optical control signal to speed up switching and has been demonstrated by Kan'an in [Kan'an et al 96]. Here the signal enters one guide with two possible exits decided by the application of a control signal. Figure 4.9 shows the device structure and signal paths in relation to the control pulses.

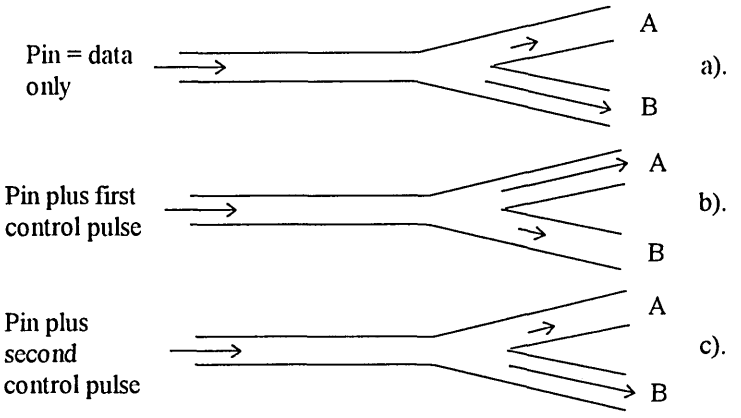

Figure 4.9 DOS with control signal.

By adjustment of the lateral position of the data signal an unequal split of the data between the output guides is obtained in the absence of a control signal (figure 4.9a). Two control pulses are used for faster switching. The first is used to switch the signal to channel A by causing an index asymmetry and a change in power division between the output guides. A second control pulse causes a spatial mirror image in the index change due to the first control switching the signal back to channel B. The active structure is a multiquantum well GaAs/AlGaAs device grown on a GaAs substrate. The material exhibited an exciton resonance at around 828 nm and experiments were carried out using a centre wavelength of around 875 nm. Experimental results on real devices are shown in figure 4.10 [Kan'an 96].

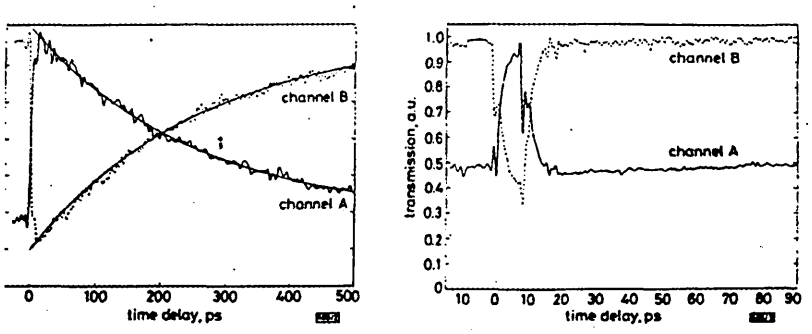

a). b).

Figure 4.10
Switching characteristics of DOS. a). One control pulse b). Two control pulses.

By varying the delay of the signal with respect to the control the split between output ports was seen to decay on a time scale of around 225 ps (figure 4.10a) which seems to place a limit on the switching speed of $\approx$ 4 GHz. Absorption of carriers is the reason for the switching non-linearity. The resolution of the switch is determined by the separation between the two pump pulses. In this experiment 200 fs pulses were used with a separation of 9 ps (figure 4.10b) and an energy per pulse of $\approx$ 9 pJ. The switching window had a rise time of 2 ps which was attributed to cooling of thermalised carriers.

(ii) Operating AlGaAs at photon energies at half the bandgap

A new technique which also addresses the problem of the slow relaxation was proposed and demonstrated by Villenewue [Villenewue et al 95]. The trade off for this effect is the high power levels required. Directional non-linear couples using this method require powers up to 42W (pulse energy 31 pJ). Lower powers were realised in this experiment by minimising the effective area of the waveguide.

(iii) Using semiconductor in a Mach Zender interferometer

Placing the semiconductor in a Mach Zender has allowed switching speeds of 90 Gbit/s to be achieved (section 4.2.4.).

4.4.2. Polymer DOSs using thermo-optics

Commercially available PMMA is used as the waveguide material for Polymer DOSs as in the thermo-optic directional couplers with standard polymer waveguide technology used to fabricate the waveguide onto silicon. The 2×2 switches are based on four equal waveguides in the formation of a symmetric × crossing (see figure 4.11).

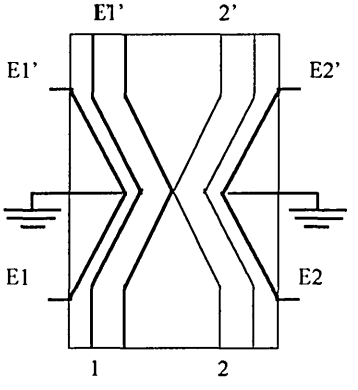

Figure 4.11 Polymer DOS.

Four heating electrodes control the device two on the input guides and two on the output guides. The heated input electrode excites the odd mode whereas the unheated input excites the even mode. The switch operates in the cross or bar state by appropriate heating of the electrodes as in table 4.2.

Heated electrodes	Signal path
E1 and E1' or E2 and E2'	1 to 1' and 2 to 2'
E1 and E2' or E1' and E2	1 to 2' and 2 to 1'

Table 4.2. Switching configurations of polymer DOS.

In an experiment by Kiel [Kiel et al 96] fixed heating powers of 45 mW were applied to the input side whilst the output heater power was varied. At 45 mW a digital output from the switch was obtained which can be maintained up to a heating power of 100 mW, showing good tolerance to variation in input voltage and temperature. As expected with thermal devices, the response time is again slow ($\approx$ 1 ms) making them more suitable for routing of high data rate signals rather than high speed switching. Typical values obtained by Kiel et al [Keil et al 96] when operating at λ=1.35μm or 1.55μm gave a crosstalk of <-25 dB with a switching power of $\geq$45 mW showing that wavelength independence is evident. Device lengths are around 25 mm.

An alternative method for manufacturing polymer waveguides is in the use of "oversize polymer rib waveguides" as in [Moosburger et al 96]. This structure is based on a guided rib structure initially developed by Marcatili [Marcatili 74]. The guides can be implemented in semiconductor material systems and have a particularly decisive advantage in being single mode in spite of their large size and large index step between core and cladding. To fabricate the devices standard semiconductor technology can be used. Waveguides are formed by etching grooves into a silicon substrate. The polymer waveguide material is the commercially available Cyclotene 3022™ a substance originally designed for electronic applications. It has low intrinsic optical loss when operating around 1.3μm. The switch is implemented in a typical 1×2 Y waveguide formation (see figure 4.12).

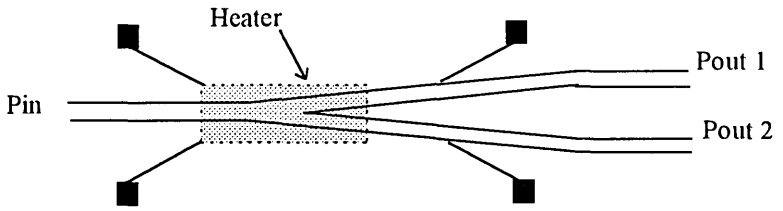

Figure 4.12 'Y' junction polymer thermo-optic switch.

With unheated branch arms equal power splitting of the signal is obtained (known as the broadcast function). On heating one arm the light is switched to the opposite path ($dn/dt < 0$). Insertion loss for the straight through path was ~2.5 dB which compares favourably with the thermo optic switch using PMMA of 6 dB [Kiel et al 96]. The power supplied to the heaters is relatively high approaching 100 mW when the switching characteristics maximise giving an extinction ratio of around 20 dB over a wide operating power (up to ≈200 mW) at an ambient temperature of 25°C. Around 170 mW the extinction ratio remains at 20 dB even up to 100°C ambient temperature. This is due to the high thermal stability of Cyclotene 3022™ which is useable up to 350°C. The polymer does exhibit wavelength characteristics and at 1.5μm the straight through path has an increased insertion loss of ~4 dB. The extinction ratio was better than 20 dB for any thermal power above ~ 190 mW.

4.5 Acousto Optic Switching

The acoustic optic filter relies on an acoustic controlling signal to change the optical properties of a material. The switch contains an acoustically generated birefringent grating by inputting an acoustic signal into the waveguide of an optical signal. Signals input to the device are flipped orthogonally with respect to TE-TM polarisation and the

signal is frequency shifted by an amount equal to the acoustic frequency. The polarisation conversion is wavelength dependent so the effect can be used for optical filtering using output polarisers [Jackel et al 96].

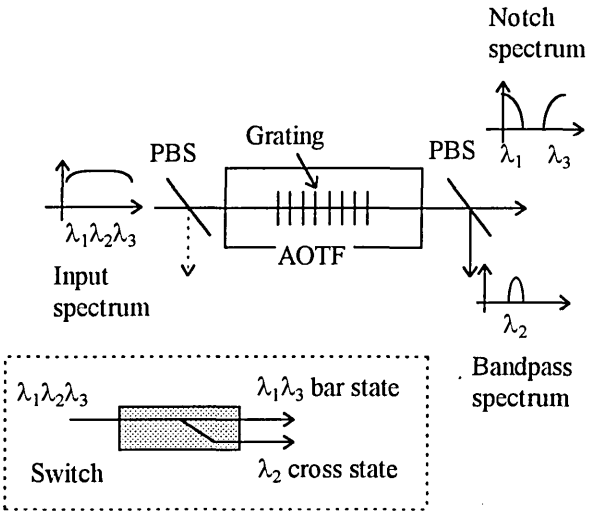

Figure 4.13 Acoustic optic tunable filter.

To perform optical switching an arrangement as in figure 4.13 was demonstrated by Smith et al [Smith et al 96] which depicts a 1×2 acousto optic tunable filter (AOTF). Polarisation beam splitters (PBS) are placed on the input and output to separate the wavelength dependent polarisation generated by the AOTF. The switch can be set in the cross state for an arbitrary spectral band; the remaining spectrum is in the bar state and split by the polarisation beam splitter. An acoustic wave input to the AOTF will cause the birefringence to compensate for the TE-TM mismatch unless $L_b \approx \Lambda$, where L_b is the beat length (= $\lambda/\Delta n$), Λ acoustic period (= V_s/f_s), λ is the signal wavelength, Δn the waveguide effective birefringence index, V_s the acoustic velocity, f_s the acoustic frequency. The bandwidth of the conversion process is $\Delta\lambda/\lambda = L/L_b$ where L is the device length. The switching speed of these devices is equal to the acoustic transit time which is the time to establish the birefringent grating and is given as $\tau_s = L/V_s$. Current AOTF

switch technology has allowed the fabrication of monolithic devices on Lithium Niobate. Typical values for this technology are τ_s = 6 ms, Δn = 0.08, L_b = 20 μm, $\Delta\lambda$ = 1.5 nm, f_s = 175 MHz, V_s = 3.7 km/s, L = 2 cm. For a typical switch [Smith 96] crosstalk is indicated at -15 dB for an 8 nm spacing. The demands of future networks is suggesting low crosstalk values ≤ -30 dB [Goldstein et al 94]. The conclusion of [Jackel 96] is that passband qualities need improving in AOTF devices before they can be used in this application.

4.6. Opto-Mechanical Reflection Switching

Opto-mechanical switches are desirable for reconfiguring fibre-optic networks because of their low insertion loss and high isolation properties. Conventional fibre routing devices are made in waveguide,(higher cross coupling loss [Lee et al 95]). Opto-mechanical devices remove the problem of coupling across different waveguides and use a technique known as free space switching. The construction is based around four fibres (2×2 switch) in the form of a cross (see figure 4.14).

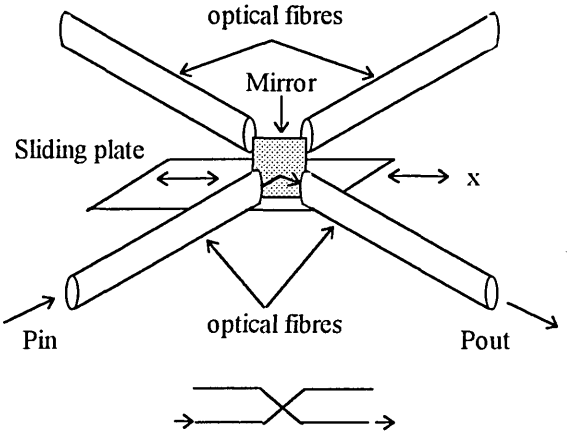

Figure 4.14 Opto-mechanical reflection device.

A space exists at the centre of the cross and the switch is configured to reflect light from two fibres to any of the other two fibres. The current method for producing opto-mechanical switches is by manually assembling bulk optical elements which is a costly method. A machining technique known as bulk micromachining was used by Dautartas [Dautartas et al 92] where the switch is machined on a Si substrate with the hybrid mounting of bulk optical elements and the use of a wafer binding technique. Monolithic integration is difficult and substantial assembly is required. Micromachining techniques were further developed when Lin [Lin et al 94] machined various surface mounted three dimensional micro-optical elements specifically for free space applications. The advantage of such a technique is the resulting light weight and possibility of integration with other micro optical elements and interface electronics. Lee [Lee et al 95] used this technique to implement a free space fibre optic switch. At the centre of the switch is a moveable three dimensional mirror with four fibre optic guide rails providing the input output paths. Obviously switch speed is slow with manual switching between states (micro actuators may be integrated onto the device for speed increase and automation). Fabrication techniques are similar to that used for micro-Fresnel lenses [Lin et al 94]. The low coupling losses measured for cross and bar state are 2.8 dB and 3.1 dB respectively; crosstalk between the two states is 26.1 dB. The higher loss for straight through signals may be attributable to the presence of below 100% reflectivity of the mirror ($\approx$ 93% for this method).

4.6 Electrostatic Mechanical Switching

The reason for the development of electrostatic switching was two fold, a) to overcome the relatively high power consumption of thermo-optic devices and b) to overcome the

polarisation sensitivity of electro-optical switches. The electrostatic switch consists basically of two electrodes which are placed adjacent to a silica cantilever bearing a moving waveguide [Ollier et al 95]. Figure 4.15 illustrates the principle.

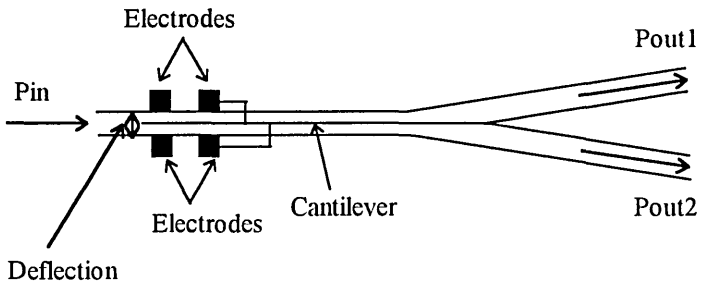

Figure 4.15 Electrostatic mechanical switch.

An electro-static force deflects the cantilever between the two outputs. In this version the switch is operated with a typical voltage of 270V at 1550 nm with an insertion loss of 6.3 dB and an isolation between signals of 24.2 dB and a switching time of 600μs. The moving waveguide contains metal which induces polarisation problems. Increasing the cantilever to metal distance to overcome this led to an increase in the voltage required. A new type of electrostatic microswitch was developed by Ollier and Mottier [Ollier and Mottier 96]. The idea was to remove metal from the moving waveguide and use an electrostatic comb instead of a two electrode configuration taking advantage of the electrostatic instability phenomenon [Petersen 77]. The use of this structure reduces the voltage required for switching since the electrostatic force is proportional to the number of electrode pairs. Also any polarisation or temperature dependence is removed with the absence of metal on the waveguide. The overall effect is to isolate the electro mechanical and optical functions. The switch operates within the wavelength range 1.3μm to 1.55μm with a mean insertion loss and isolation of 3.8 dB and ≈32 dB respectively with

an operating voltage is ≈ 28.3V. Switching time is 800μs which is typical of micro-mechanical devices.

4.6 Switching Architectures

Previous work in this chapter has focused on switches which are single discrete devices and can function on their own switching up to two input signals to two output ports. For optical networks systems many signals may need switching or re-routing and the switch must be able to switch multi input signals to a number of output choices. This section will illustrate examples of current switching architectures which have been implemented using some of the techniques previously discussed.

4.6.1 Mach Zender thermo-optic.

An optical path cross connect system which in principal takes in M fibre input signals (see figure 4.15).

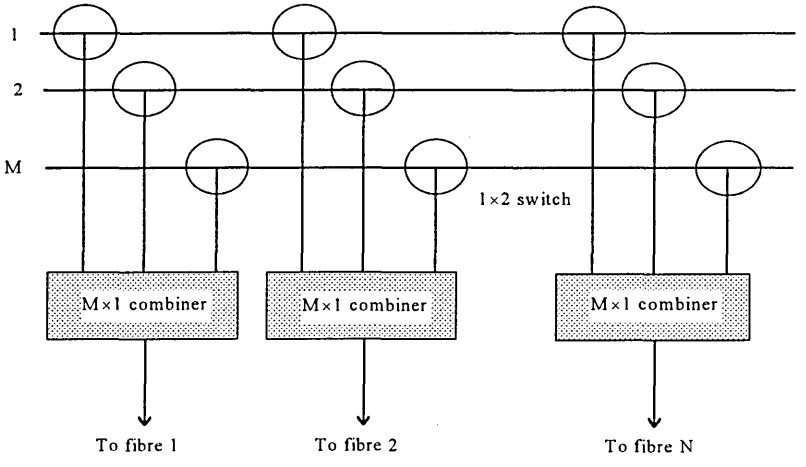

Figure 4.15 Optical path cross connect system thermo-optic Mach Zender.

In this configuration a set of M input fibres can be delivered to any of N destination fibres. The main switching section is centred around 1×2 Mach Zender switches which

re-rout the signal from the existing path. Thermo-optic switching is used as previously discussed in a Mach Zender configuration. The switches have the characteristically high power requirement of this method with 0.55W per switch being required. Other system components were passive devices using star couplers giving an overall on off ratio of 42 dB and an insertion loss of 12.5 dB [Koga et al 96]. With the switch in figure 4.15 used as a module a set of 16 switches were used to re-route any of eight channels to a choice of sixteen outputs.

4.6.2. Electro-optic directional coupler

Directional couplers have been used to demonstrate a 16 × 16 guided wave optical switching system [Murphy et al 96]. The system is built around 2×2 directional couplers based on lithium niobate and uses a method of connection known as the extended shuffle network. Figure 4.16 shows how two modules are constructed from the 2×2, switches, a 16×16 and a dual 1×8, (4.16a and 4.16b respectively). These are connected to form the composite switch (figure 4.16c, note the 1×8 modules are connected in a 1×7 configuration).

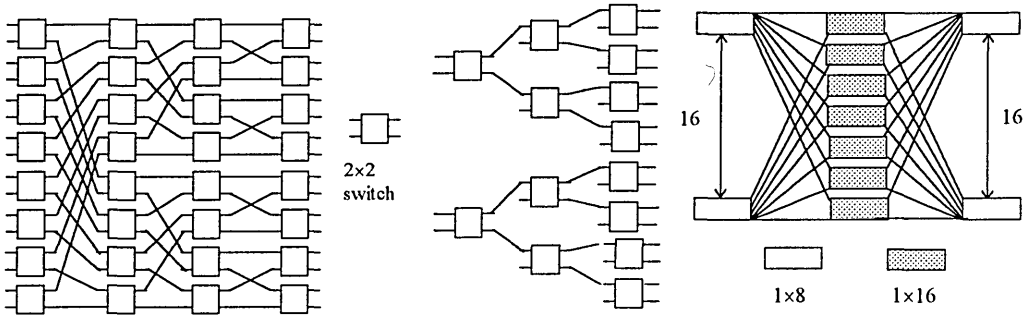

Figure 4.16 16×16 electro-optic switch matrix.
a). 16×16 module b). 1×8 module c). 16×16 switch

The array operates at 1.55μm and is polarisation independent. Cross talk values are -28 dB and it operates with a voltage of 12V and a total power consumption of 90 W which includes 2 W for a set of indicator LEDs. Insertion loss varies (depends on signal path) between 18.8 dB and 28.4 dB. Okayama and Kawahara [Okayama and Kawahara 94] also developed a prototype switch on directional couplers which has a 32×32 input output configuration. See figure 4.17.

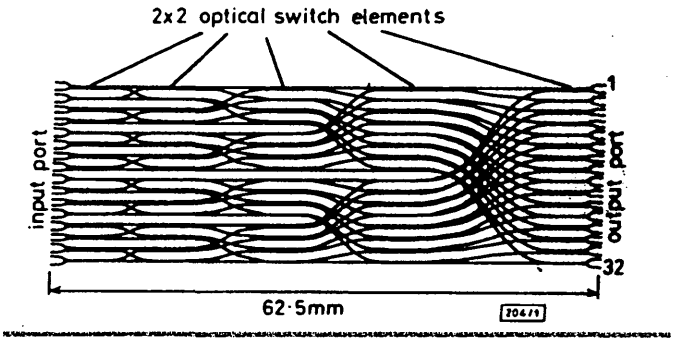

Figure 4.17 32×32 switch matrix Kawahara [Okayama and Kawahara 94].

The device structure was based on an architecture known as the modified banyan network [Murphy et al 93] in which small switches are connected together to form larger matrixes. Each switch element is built around a 2×2 switch based on a $TiLiNb0_3$ directional coupler configuration [Okayama et al 91]. Previously the largest switch array of this kind was demonstrated by Duthie [Duthie and Wale 91] which was a 16×16 matrix. Each switching element can be fabricated to an individual length of 6 mm. A 32×32 device has a typical length of 62.5 mm. At each switch element there are two waveguide crossings which contribute to crosstalk and excess loss. For this configuration one signal path encounters a maximum of 26 crossings with a total relative loss of ~ 11 dB (indicating ~ 0.4 dB per waveguide). A feature of this type of array is that there is a wide swing of signal attenuation between the two extremes of physical output due to the

waveguide crossings encountered. Lithium Niobate is currently the popular choice for switch arrays because of the maturity of the technology [Murphy 96].

4.6.3 Lithium niobate DOS.

O'Donnell [O'Donnell 92] has constructed 1×16 and 1×32 switch matrices using DOSs based on Lithium Niobate to take advantage of a single tolerant voltage with high fabrication tolerance and wavelength independence. The switches were operated at 1.3μm. The results for each configuration are given in table 4.2.

	1×16	1×32	1×32 as 1×16
Insertion loss.	8.5 dB	9.6 dB	9.6 dB
Extinction ratio.	16.5 dB	16.8 dB	28.8 dB
Drive voltage.	±65V	±65V	±65V

Table 4.2. $LiNb0_3$ DOS switch architectures.

The third configuration used a 1×32 matrix operating as a 1×16 switch which gave improvements in extinction ratio and allowed less complex electronics.

4.6.4 TWSLA array

Optical switching using low gain semiconductor laser amplifiers was proposed by Chien [Chein and Winston 96]. An array of 40 TWSLAs switching units with 8.3 dB couplers was configured to give an 8×8 switching arrangement with a cascade of five TWSLA switches in line. Each switch unit is based around a 2×3 waveguide coupler, two low gain TWSLAs and a header processor to form a modular 2×2 switch. The small signal gain of each TWSLA is adjusted to compensate for the total loss of the switch. For this architecture typical losses originate from (for a 8×8 array) $5\times L_c + 5L_f + L_c$ where L_c is switch unit coupler loss, L_f TWSLA facet loss, L_c output coupler loss. Typical values indicate a total loss of $5\times2 + 5\times5 + 3 = 38$ dB total loss. Five amplifiers then require a

gain of 38/5 = 7.6 dB. With amplifiers operating at low gain, spontaneous emission noise is reduced. The switching time of such a configuration is ≈ 3.4 ns using a pulsed current input between 0 and 34 mA. With low gain operation the fabrication process is simplified with the amplifiers less dependant on the facet reflectivities required.

4.7 Summary

This chapter has presented a review of current technologies for the switching of signals in the optical domain. The major techniques for fabricating switches and waveguides have been identified and the physical processes to effect switching. Initial emphasis is on a basic switching unit which has two inputs and two outputs. Switches are characterised by excess loss, crosstalk/extinction ratio between the wanted and rejected paths. Switching times are given to assess the data rate possible for the device and are summarised in table 4.3. Switching architectures built up from some of the switches are viewed and characterised.

Device	Switch speed
Mach Zender, thermo-optic	25 Gbit/s
Mach Zender, TWSLA	90 Gbit/s
Mach Zender, electro-optic	20 MBit/s
DOS, thermo-optic	1 kBit/s
DOS, semiconductor	1 GBit/s
Acoustic-optic	160 Bit/s
Electro-static	1.25kbit/s

Table 4.3. Switching speeds of optical switches

Chapter 5

Optical Multiplexing /Demultiplexing.

5.1 Introduction

This chapter reviews the current research in optical domain multiplexing and demultiplexing. The work is largely concerned with optimising the use of the large bandwidth available over a fibre communication channel. The main effort is currently centred around the two concepts, WDM and TDM,which have been used extensively in electronic communication systems. The chapter will begin with a brief introduction to WDM. Following this the main emphasis will be on TDM systems. The focus of this chapter will then move towards a system known as the asymmetric semiconductor laser amplifier loop mirror (ASLALOM) which will be the main topic of the modelling and simulation techniques discussed in later chapters.

5.2 Wavelength division multiplexing

5.2.1 Concepts

To produce a WDM signal individual signals to be transmitted are each modulated onto a carrier wave using differing wavelengths (figure 5.1).

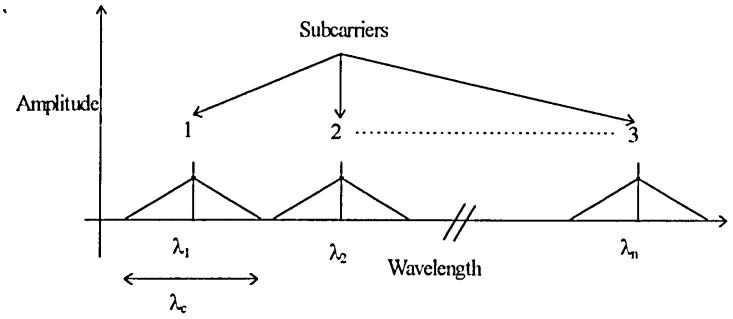

Figure 5.1 Typical WDM spectrum.

Each signal is allocated a bandwidth of λ_c and the subcarrier wavelengths are designated $\lambda_1 ... \lambda_n$. The composite signal containing all channels is then modulated onto a main carrier and transmitted. Table 5.1 lists typical WDM capacities currently under investigation.

No. of channels	Data rate/ Gbit/s	Distance/ km	Reference
4	10	1587	Taga 96
8	10	1000	Taga 96
8	5	6000	Bergano and Davidson 96

Table 5.1 Typical WDM systems under investigation.

WDM systems have the advantage in that they use commercially available components. Their main rival, optical time division demultiplexing OTDM, is still confined to the laboratory and present systems are only operating at moderate line rates (currently around 10 Gbit/s). Non-linearities in the fibre also impose limitations on WDM system performance e.g. the effect due to Stimulated Raman Scattering (SRS) leads to a conditional equation for the power per channel for a particular signal to noise ratio (SNR) degradation. For example, for 0.5 dB degradation [O'Mahony et al 95]:

$$P < 10.28 \times 10^{12} / [N(N-1)\Delta f L_{eff}] \qquad (5.1)$$

where N is the number of channels with a spacing of Δf and L_{eff} is the effective length of the system in km. For example with a transmitter power of 0 dBm, operating wavelength of 1550 nm and wavelength spacing 4 nm the maximum number of channels for distances > 1000 km is 5.

High capacity systems also require closely placed channels which in turn are affected by the effect known as four wave mixing (FWM) where two signals with different frequencies beat together to produce new frequencies which may fall into the slot occupied by another channel. Fig. 5.2 shows the maximum power transmission length for experimental systems due to FWM [O'Mahony 95].

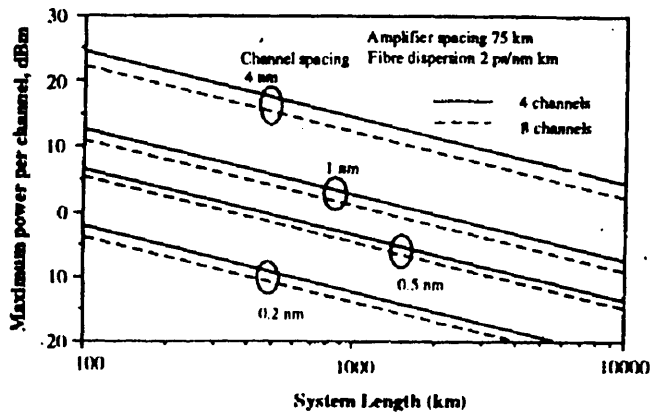

Figure 5.2 FWM effects in WDM systems [O'Mahony 95].

For example a 0 dBm system with channels spaced 1 nm apart can be transmitted over 2000 km. To increase this distance to 10,000 km the channel spacing must be increased to 4 nm.

Cross phase modulation (XPM) between different signals travelling along the same fibre, where one signal modulates the other by changing the refractive index of the fibre, also limits the number of channels [Wang et al 95]

5.2.2 Implementation of a WDM network

Figure 5.3 shows a typical WDM network together with the node architecture.

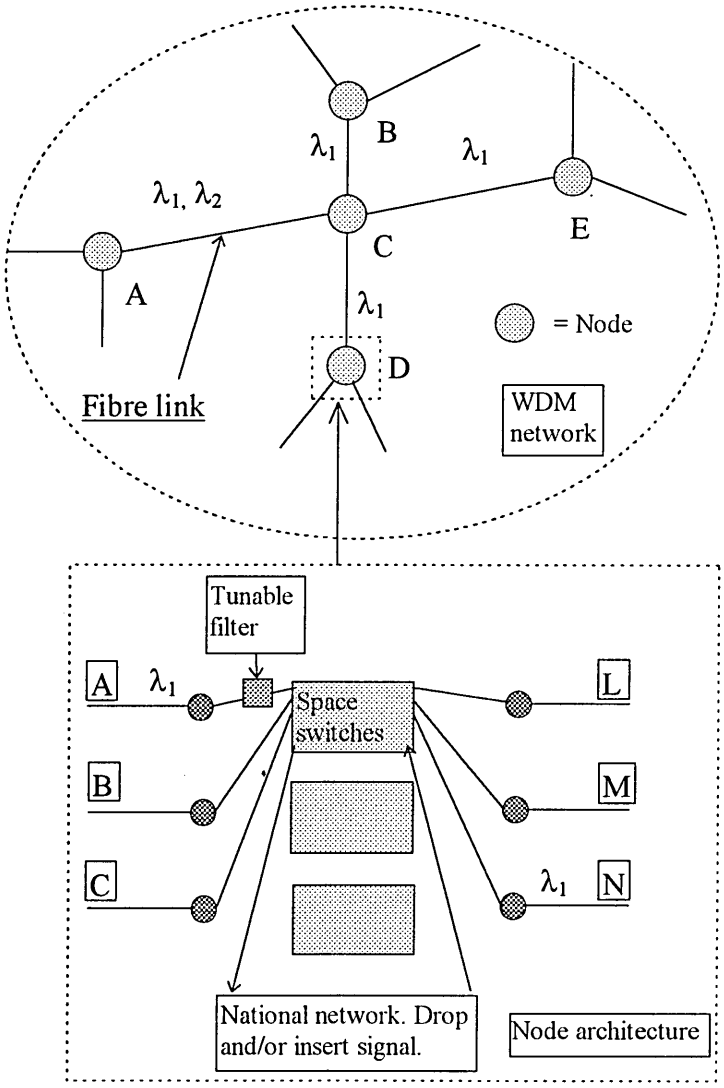

Figure 5.3 WDM Network and node architecture.

The nodes in figure 5.3 could represent a City network infrastructure [O' Mahony 95]. In the typical system shown, consider the problem of establishing a link between A and E where the sub-carrier wavelength used is λ_1. If additionally a link is needed between A and C then this needs to be at a different wavelength from λ_1 to enable discrimination

over the shared section A to C. The advantage of this system is wavelength re-useability as demonstrated by the link C to D which can use the wavelength λ_1 since route A to E and B to D have no common path. The essence of such a system is in the node architecture shown boxed in figure 5.3 [Hill et al 93]. Here a channel λ_1 from an adjacent node is WDM onto any connecting node by initially filtering out the appropriate wavelength and then, by using space switching, the channel may be re-routed to any outgoing fibre or it can be dropped off to the national network at that node.

5.3 Optical Time Division Multiplexing

The limitation placed upon WDM by fibre non-linearities has generated interest in OTDM systems whereby a single wavelength has been used to support capacities up to 100 Gbits/s over 200 km [Kawanishi et al 94]. Appropriate clock frequencies can readily be implemented using electronic components which are commercially available. Demonstration of a 40 Gbit/s (2 x 20 GBit/s) all optical multiplex/demultiplex transmission system over a distance of 560 km has been shown experimentally by Lee et al [Lee et al 96]. Although OTDM is demonstrated in this reference as a point to point communication system its potential capacity makes it a promising candidate for network systems. At the moment the drawback of OTDM systems is that only one channel is demultiplexed from the system at any one time [Sokollof et al 94].) Due to the device complexity complete demultiplexing has only been reported on a small scale (section 5.3.4.2) and most current demultiplexers are single output devices. Bodkter [Bodtker 95] has outlined theoretical architectures for the possible demultiplexing of more than one channel.

5.3.1 Concepts of OTDM

In an OTDM system each user is allocated a channel which is transmitted at a rate which can be switched by electronic methods. Figure 5.4, shows an OTDM timing diagram in which the frame separation is t_x and the channel separation is t_c. The interleaving is performed sequentially as opposed to a packet data method in which blocks of data are given individual time slots. A clock pulse inserted at the beginning of each frame synchronises the switching of a particular channel in an OTDM demultiplexer.

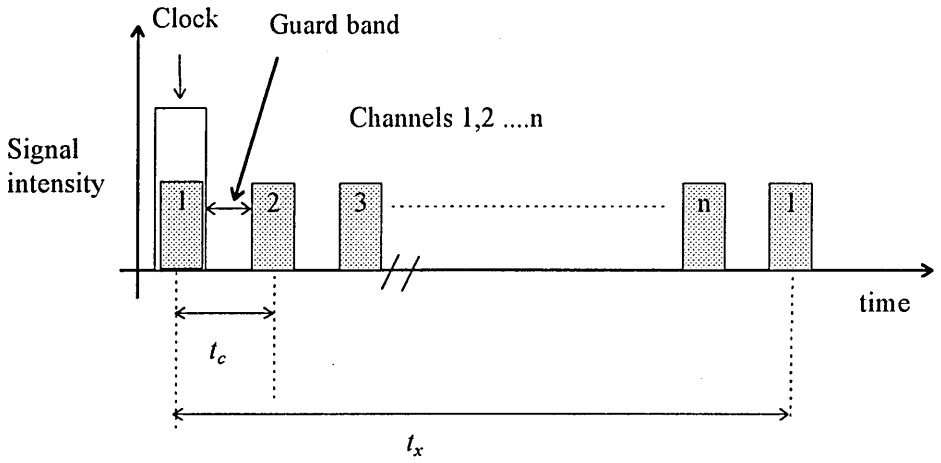

Figure 5.4 OTDM timing diagram

A significant advantage can be gained from OTDM systems by arranging for the transmitted pulses to be short compared to the shortest period on any line. This will result in reduced interchannel crosstalk. Sokolloff [Sokollof et al 93] has implemented a system which uses 5 ps pulses at a data rate of 50 Gbit/s thus allowing a guard band of 7.5 ps between adjacent pulses.

5.3.2 OTDM processing nodes

When OTDM is implemented in a network the system must allow for the retrieval and insertion of data into the network infrastructure as in the previous example on WDM.

Figure 5.5 shows a typical processing node consisting of a number of functional blocks [Spirit and Blank 93].

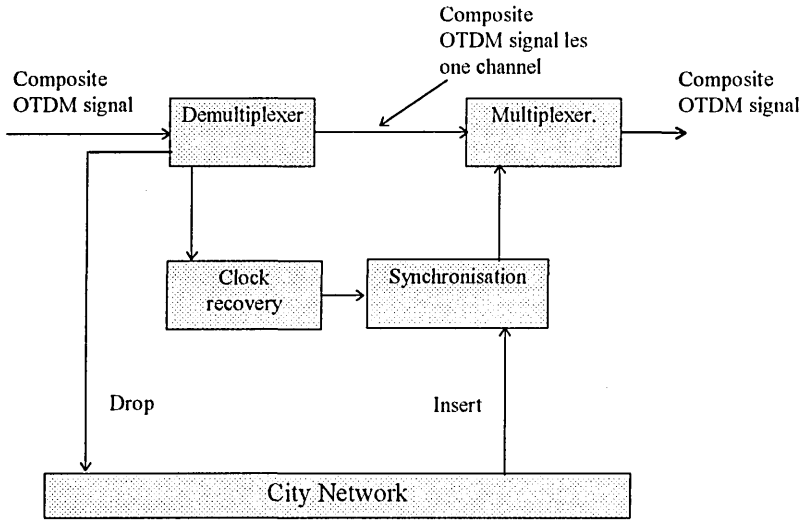

Figure 5.5 OTDM processing node

The network data enters the node at the demultiplexer. The demultiplexer selects ('drops') the particular channel requested at that node. The frame is now one channel less and at this point the node may insert another frame in the vacant time slot. Note that the channel may come from this node or from a remote one. An essential requirement of an OTDM system is synchronisation. To synchronise demultiplexing and multiplexing stages, circuitry is required to recover the clock signal from the composite data stream. The clock signal, in conjunction with the synchronisation block, ensures that data is removed/inserted into the correct time slot. Ellis [Ellis et al 94] has demonstrated the feasibility of this concept practically by dropping and inserting a 10 Gbit/s channel within a 40 Gbit/s OTDM signal. Electronic clock recovery is used to provide synchronisation throughout the system.

5.3.3 Optical time division multiplexing techniques

5.3.3.1 Passive Multiplexing

The first method of multiplexing discussed employs a passive technique where the interleaving of the TDM signals is achieved using the time delay associated with the propagation through a device. Figure 5.6 depicts an experimental system for a 20 Gbit/s NRZ data link [Wickens et al 91].

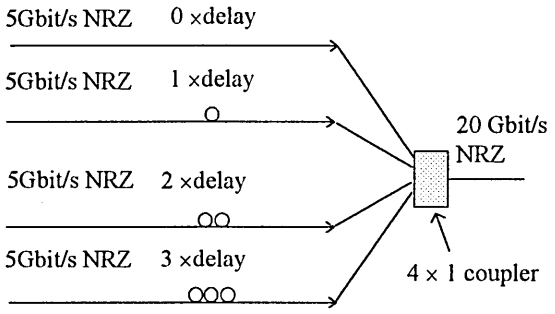

Figure 5.6 Passive multiplexing system.

A four channel system is shown with data rates per channel of 5 Gbit/s. To place each data channel in its appropriate time slot a fibre stretcher delay is placed in each line (the delay is provided by the length of fibre). Delays of 0, 1, 2, and 3 times the required pulse separation place the channel in its appropriate time slot. The four channels are then combined using a passive 4 x 1 fibre coupler to give a 20 Gbit/s OTDM output. The system is based around single mode fibre components and semi integration is possible if silicon waveguiding technology is used. A similar passive method has been used to implement multiplexing of a system at 40 Gbit/s over 560 km of dispersion shifted fibre [Lee et al 96] and a 200 Gbit/s multiplexed transmission over 100 km by [Kawanishi et al 96]. Further progress in passive optical multiplexing has been demonstrated in principle by [Lee and Shu 95] in which high repetition rate optical pulses at over 1 Terahertz have been produced. This method uses a combination of two passive fibre

couplers (16 x 16 and 8 x 8) connected to form fibre loops configured in parallel. With the use of fibre switches it has the potential for use in high speed TDM systems. Active research into improving bit rate-distance product in the area of OTDM by various workers [Kawanishi et al 95], [Morioka et al 96], [Kawanishi et al 96] have shown that OTDM systems are becoming a challenge to current network technology. Figure 5.7 shows a graphical history of the development of the progress of laboratory OTDM transmission systems.

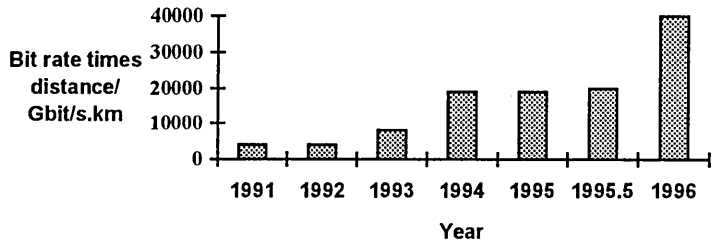

Figure 5.7 Development of OTDM transmission systems.

5.3.3.2 Active multiplexing

Although passive multiplexing offers less complex implementation, active multiplexing has a certain advantage. Conventional systems may operate with a NRZ format but for ultra high speed systems in an OTDM network RZ format is preferable. An active multiplexer can provide the dual function of multiplexing and NRZ to RZ conversion. The active multiplexer architecture is shown in figure 5.8 where 'TX' represents a 2×2 electro-optic switch.

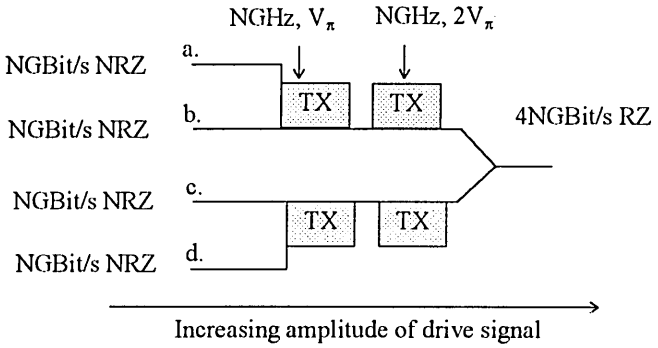

Figure 5.8 Active multiplexing system.

The central component is an electro-optic switch which has a transfer function for one arm of the switch given by:

$$E = 0.5(\exp(jV/V_\pi)) + \exp(j\pi)) \tag{5.2}$$

where V_π is the voltage required for switching. The corresponding drive signal is represented in voltage and frequency as $V = V_0\sin(\omega t)$ for a sine wave input where $2V_0 = V_\pi$ for the first stage, and $V_0 = V_\pi$ with a bias point of V_π for the second stage. Figure 5.9 shows the channel (a) output waveform, with a sinusoidal input as determined from equation 5.2. Note the RZ signal of the second stage.

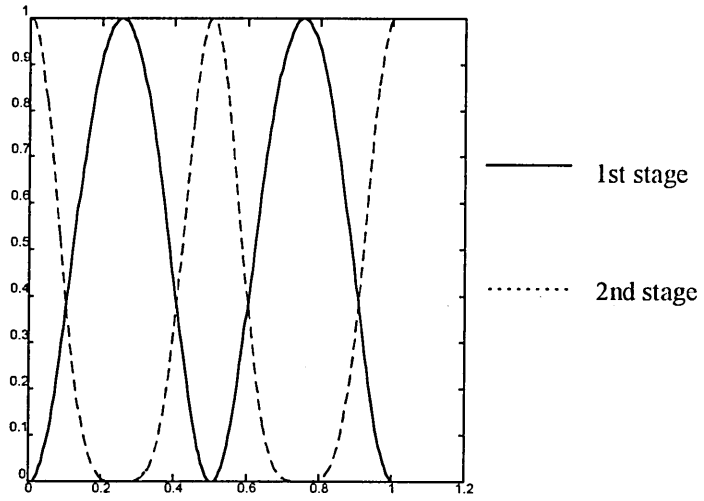

Figure 5.9 Output from active multiplexer stages.

An active system having multiplexed 4×3 GHz mode locked signals to 12 Gbit/s has been demonstrated by Blank [Blank 88]. The advantages of this configuration are that only simple sinewaves are needed to drive the switches available with current electronics technology, the required frequency is the same at all stages of the multiplexer. A disadvantage is that the corresponding drive signal amplitudes are quite high, the first level of multiplexing requiring a 12V 3 GHz signal with a 24 V 3 GHz signal needed for the second stage.

However, experimental systems currently use a passive method of multiplexing. Examples can be found in references [Morioka et al 96] and [Kawanishi et al 96] which use planar silica waveguide technology, and [Lee et al 96] which uses fibre couplers.

5.3.4 Optical time division demultiplexing techniques.

To implement OTDM research efforts have basically centred around the following techniques:

- Four wave mixing (FWM)

- Non-linear loop mirror NOLM
- Semiconductor laser amplifier loop mirror SLALOM
- Asymmetric semiconductor laser amplifier loop mirror ASLALOM

5.3.4.1 Demultiplexing using FWM.

FWM demultiplexing is achieved by the mixing of two signals of different wavelengths in a non-linear medium. The non-linearity in this case arises from the third order non-linear susceptibility $\chi^{(3)}$ of an optical fibre such that the polarisation P induced on an electric field propagating through the fibre obeys the relationship:

$$P = \varepsilon_0 \chi^{(3)} E^3 \tag{5.3}$$

where ε_0 is the vacuum permitttivity of the medium and E is the electric field. The latter consists of two signals given by the complex propagating waves with propagation constant k_i and frequency ω_i which are given by:

$$E_s = \exp j(\omega_s t - k_s z) \text{ and } E_c = \exp j(\omega_c t - k_c z) \tag{5.4}$$

The signals mix according to:

$$P = \varepsilon_0 \chi^{(3)} (E_s + E_c)^3 \tag{5.5}$$

where the subscripts c and s represent the control and the channel to be demultiplexed. The mixing of the two signals takes place in a long length of fibre in which the control signal propagates alongside the selected channel introducing a non-linearity into the fibre (figure 5.10).

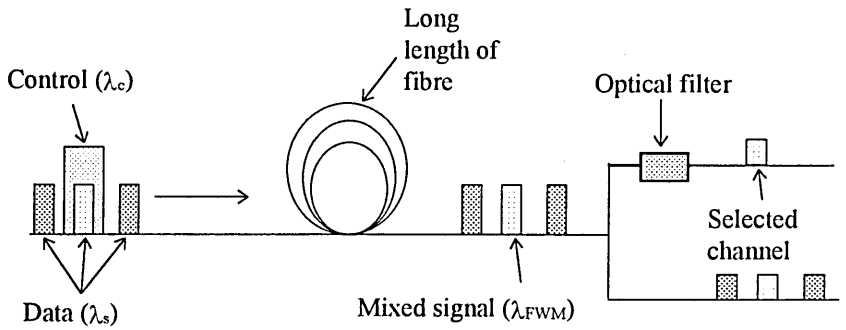

Figure 5.10 Block diagram of FWM demultiplexer.

FWM causes a new component to be generated with a frequency given by:

$$c_f/\lambda_{FWM} = 2c_f/\lambda_s + c_f/\lambda_c \tag{5.6}$$

where c_f is the speed of light in the fibre. Filtering of the FWM component is then needed to demultiplex that channel. The rise time of the non-linear effect is fast (a few femtoseconds) but long interaction lengths are required to generate the non-linearity, thus precluding the possibility of integration. In an experiment by Andrekson [Andrekson et al 91] 14 km of dispersion shifted fibre were needed to generate the required non-linearity. The signal used had a wavelength of 1.531 μm and the control 1.48 μm with respective powers of 4.3 dBm(17 mW) and 5.2 dBm (33 mW). Alternatively the control power can be increased with smaller lengths of fibre, as demonstrated by Morioka [Morioka et al 94] who used 3 km of fibre but needed an increased pump power of 380 mW. The reduced length of the fibre also reduces pulse broadening which occurs due to fibre dispersion in long haul OTDM transmission systems. An equalising circuit has also been used to compensate for the fibre dispersion by Takiguchi [Takiguchi et al 96]. This method offers a trade off between fibre length and control power/circuit complexity. The dependence of the FWM effect on fibre

length and control signal power can be seen from the following equation which gives the power of the FWM component [Hedekvist 95]:

$$P_{FWM}(L) = \frac{1024\pi^6}{N_f{}^4 \lambda_{FWM}^2 c^2}(3\chi^{(3)})^2 \frac{P_s(0)P_c(0)}{A_{eff}^2} e^{-\alpha L} L_{eff}^2 \eta \qquad (5.7)$$

where N_f is the refractive index of the fibre, λ_{FWM} the wavelength of the FWM component, $P_s(0)$ the signal power, $P_c(0)$ the control signal power, (on entry to the fibre), A_{eff} the effective mode area of the fibre, α the fibre loss, L the fibre interaction length, η a factor which describes the phase matching of the signals. The fibre effective length is given as:

$$L_{eff} = (1 - e^{-\alpha L})/\alpha \qquad (5.8)$$

Although the method has successfully demultiplexed high bit rate systems (100 Gbit/s to 6.3 Gbit/s [Morioka et al 94]) it continues to be an inefficient method as power is wasted in the unused frequency components of the four wave signal. Figure 5.11 shows results from [Kawanishi et al 94] which illustrate the power spectrum resulting after the FWM of two signals.

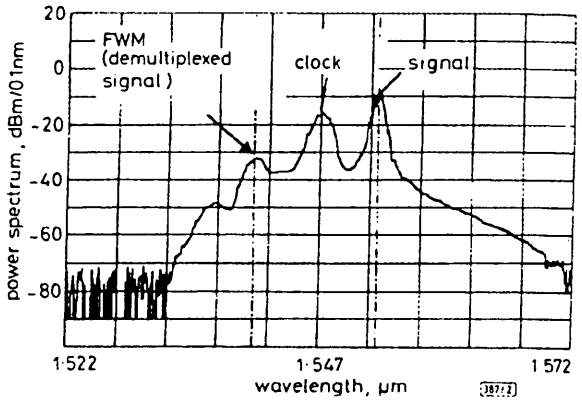

Figure 5.11 Power spectrum of FWM [Kawanishi et al 94].

This experiment demultiplexed a 6 mW input signal with an output power of 0.41 mW indicating a conversion efficiency of only 7%. The graph clearly indicates the FWM process (note the clock in figure 5.11 is equivalent to the control signal) whereby the signal (data) of wavelength 1.5528 μm mixes with the control signal of wavelength 1.547 μm to produce a FWM. Substituting the above experimental values in equation 5.6 gives:

$2\times(3\times10^{8}/1.547\times10^{-6}) - 3\times10^{8}/1.5528\times10^{-6} = 1.947\times10^{14}$ Hz

from which resultant FWM component wavelength is:

1.947×10^{14}Hz $\Rightarrow 3\times10^{8}/1.947\times10^{14} = 1.541\mu$m.

5.3.4.2 Non linear optical loop mirror (NOLM)

In this method of switching an inherent non-linearity of optical fibres is used known as the Kerr effect. This effect results from variations in the refractive index of the propagation medium as a result of variations in optical intensity. The phase velocity of any light beam passing through the fibre will be affected by its own intensity and the intensity of any other beams present. When the intrinsic third order non-linearity of silica fibres is used the signal phase shift can be expressed as:

$$\Delta\phi_{signal} = \frac{2\pi}{\lambda_{signal}} n_2 L I_{signal} + 2\frac{2\pi}{\lambda_{signal}} n_2 L I_{control} \qquad (5.9)$$

where n_2 is the Kerr coefficient, I_{signal} the intensity of the signal to be switched, $I_{control}$ the intensity of the beam used to switch the signal, λ_{signal} is the signal wavelength and L the length of the fibre. To construct a fibre loop mirror the architecture of a fibre loop reflector is used which is based on a Sagnac interferometer. The loop itself consists of a long length of fibre, which may be a kilometre or more, which is necessary to produce the non-linear effect. A schematic of the system is shown in figure 5.12.

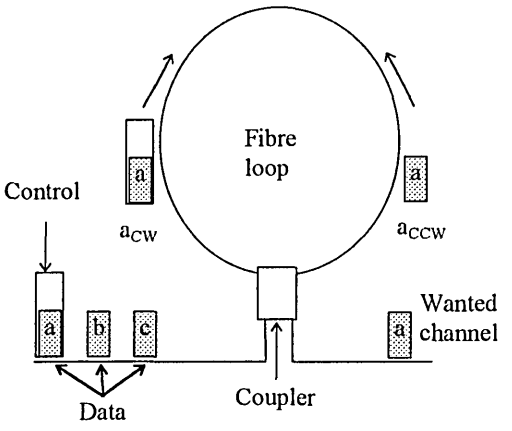

Figure 5.12 Non linear optical loop mirror.

The loop has as its input the high frequency data stream plus a control pulse at the frame rate. The data splits at the coupler and propagates around the loop in contra directions (clockwise a_{CW} counterclockwise a_{CCW}) and recombines at the coupler. In the absence of a control pulse the pulse exits via the input port. If a particular pulse in the loop (in this example a_{CW}) is straddled by a control pulse then that pulse experiences cross phase modulation according to the second term on the right hand side of equation (5.9) and undergoes a phase change. The result back at the coupler is a difference in phase between the a_{CW} and a_{CCW} pulse and the pulse exits at the output port. In an early experiment 100m of dispersion shifted fibre was used in the loop, which required a peak power of 10W for the control [Blow et al 90]. Nelson [Nelson et al 91] found a significant power saving could be achieved by increasing the length of fibre to 6.4 km, allowing the peak control power to be reduced to 160 mW. A data rate of 100 Gbit/s has been demultiplexed to a channel rate of 6.3 Gbit/s [Uchiyama et al 94] using 3 km of fibre and a control power of 425 mW. Note that the value of n_2 in equation 5.9 for silica fibres is 3.2×10^{-20} m^2/W which is one of the lowest value for any solid state material.

From this, it may appear that silica is a poor choice for non-linear optics but this is compensated by the low absorption of silica which allows the use of long lengths to achieve the required effect. As a general rule 1W switching power requires 1 km of fibre.

As is the case with Four wave mixing, the long fibre length creates a dispersion problem. To minimise the effect of dispersion between the control and signal pulses the wavelength chosen for the control and signal in [Nelson 91] were 1.53μm and 1.56μm respectively. As the dispersion minimum in this case occurs at 1.545 μm this ensures that the phase velocity difference between the two signals was minimised and the propagation speed for both was identical. To prevent propagation of the control pulse with the CCW pulse the coupler was fabricated so that the control pulse propagates CW only. The coupling ratio for the data signal wavelength is set at 50:50 and at 100:0 for the control signal. If low switching energies are used then the long lengths of fibre used can cause various problems, one of which is an attenuation loss. Another is polarisation instability which arises because of birefringence in the fibre [Desruelle et al 95]. In essence orthogonal components of the signal travel at different speeds along the fibre. The result is a time delay between the components after travelling the fibre loop. The control pulse may 'walk over' more than one data pulse. The result is that pulses adjacent to the wanted channel undergo a phase shift and may be partially demultiplexed. Compensation for this effect requires the addition of extra components such as wave plates, Faraday mirrors and polarisation beam splitters. Another method would be to cross splice the fibre halfway along its axis to 'speed up (slow down)' the 'slow (fast)' component on the first half of the fibre. An example of the latter can be found in [Uchiyama 94]. Environmental instability of the fibre (e.g. temperature) is a problem which also occurs.

It is difficult to implement this technique as an integrated circuit because of the long fibre loop required.

5.3.4.3 Semiconductor laser amplifier loop mirror (SLALOM)

An enhancement of the fibre loop mirror was reported by O'Neill [O'Neill and Webb 90] who demonstrated that the inclusion of a TWSLA in a loop mirror could provide self switching of optical pulses (see figure 5.13).

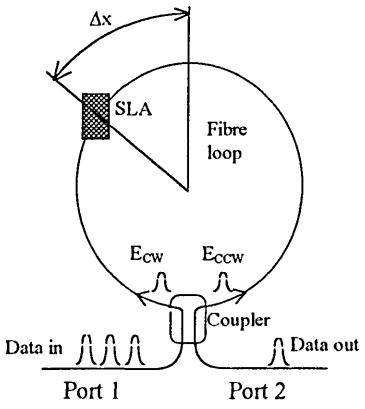

Figure 5.13 Architecture of SLALOM.

In this case a data signal with a power of 250μW gave self routing of pulses in a much reduced loop length of only 17m. The loop used in this case included a non-reciprocal element which had a gain and phase response G_H and ϕ_H in the CW direction and G_L and ϕ_L in the CCW direction respectively. This was implemented using a split device which had amplification/attenuation in the CW direction and attenuation/ amplification in the CCW direction. The output from port two of the loop is given as the sum of two fields:

$$\frac{Ee^{j\omega t}}{2}\left(G_H e^{j\phi_H} + G_L e^{j(\phi_L+\pi)}\right) \tag{5.10}$$

The non-linearity in this case is provided by the modification of the refractive index of the TWSLA due to an input signal saturating the device. It is found that the refractive index in a semiconductor material is related to the carrier density linearly providing the

signal remains around the band energy of the material. Pumping of an TWSLA by a high power optical signal depletes the number of hole electron pairs giving an intensity dependent refractive index which is characterised by the steady state relationship [Adams et al 95]:

$$N = \frac{N_0 - G_s(K_N)P / P_{SAT}}{a(1 + P / P_{SAT})} \tag{5.11}$$

where N_b is the refractive index near the band edge P signal power, N_0 is the refractive index with no optical signal propagating through the device , K_N is a parameter which defines the rate of change of refractive index with carrier density and is a constant for signals operating at the band gap of the material. The effect in this case is termed strong and slow, which permits slow switching with small pulse energies. The TWSLA in the loop is providing a non-linearity in much the same way as the long length of fibre did in the NOLM. Consider the case where the TWSLA is displaced slightly off the loop centre (figure 13) then the effects of contrast enhancement can be demonstrated. Figure 5.14 shows the timing diagram of a contrast enhancement system.

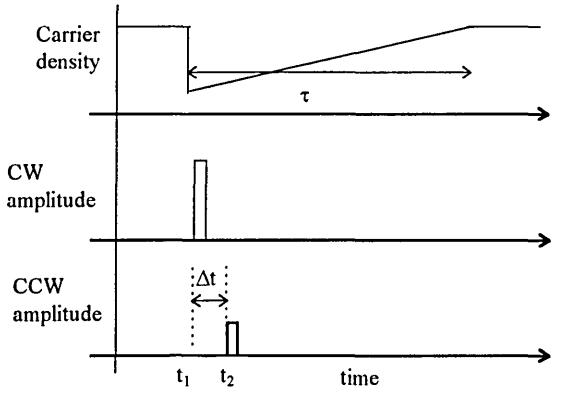

.**Figure 5.14** SLALOM timing diagram (contrast enhancement).

A data signal is fed into the loop via port 1 which splits into CW(E_{cw}) and CCW(E_{ccw}) fields each equal to half the power of the original signal. The CW pulse reaches the

TWSLA at a time t_1 and quickly depletes the carrier density. The CCW signal reaches the TWSLA at a time later (t_2) determined by the off centre displacement of the TWSLA Δx. If the CCW signal reaches the TWSLA before the carrier density has recovered (which is the case in figure 5.14), then it experiences a gain and phase change due to the reduced carrier density of the device. On returning to the coupler the CW and CCW signals will have different amplitude and phase values. Interference between the two signals now occurs at the coupler and a signal exits via port 2. O'Neill [O'Neill 90] used a 10 ns pulsetrain at a repetition rate of 100 MHz which self routed to port 2 of the loop at a pulse power of $\approx$ 150 μW with equal power outputs at port 1 and port 2. At a power input approaching 250μ W the power ratio changed abruptly to 2 (port 2 : port 1). The abrupt change demonstrates the loop's ability to perform switching between ports at a particular power level. Eiselt [Eiselt 92] used a similar set-up to demonstrate optical correlation between adjacent pulses in a data stream. The SLALOM has to wait a period equal to the recombination time (0.5 - 1 ns) before it can switch again resulting in a switching speed between 1 - 50 Gbit/s. This method also has no provision to select a particular pulse in a data stream of equal power pulses. Transmission is dependent on the power of the input pulse.

5.3.4.4 Asymmetric semiconductor laser amplifier loop mirror (ASLALOM)

To take advantage of the fast switching afforded by the NOLM and the low power/ small size of the SLALOM Sokolloff [Sokoloff 93] developed a loop architecture incorporating an TWSLA with an additional coupler in the loop (see figure 5.15).

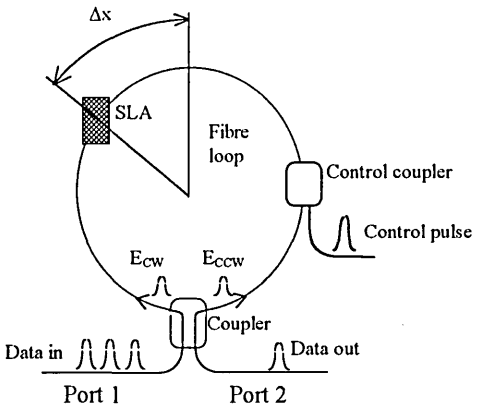

Figure 5.15 Architecture of ASLALOM.

The purpose of the additional coupler is to introduce a relatively high power control pulse into the loop.

Operation of ASLALOM.

The data signal train enters the coupler at port 1 and splits into CW and CCW pulses. With no control pulse applied the TWSLA assumes a constant refractive index. Low power signals input to the TWSLA undergo linear amplification with an associated time delay due to the refractive index of the material, (the power of the data signal is assumed to be non-saturating and has a negligible effect on the TWSLA index properties). In this mode of operation both CW and CCW pulses undergo equal propagation delays and the pulse is reflected and re-emereges via port 1. A high power input pulse to the control coupler causes saturation of the TWSLA and a corresponding change in the gain and refractive index. The modification will have a finite duration, due to the device recombination time.

Three situations are of interest when analysing the ASLALOM with a control pulse.

1) Both CW and CCW signals enter the loop and reach the TWSLA far in advance of the control pulse. With the TWSLA being in its unmodified state the pulses propagate

through the loop with identical propagation characteristics and the pulse exits via port 1 therefore, no switching action has occurred.

2) Both pulses enter the loop after the control pulse has propagated through and will each experience the TWSLA in a state of optical modification. Once again both pulses propagate with the same time delay and with no relative phase shift taking place the pulse again exits from port 1.

3) The control pulse reaches the TWSLA after the CW pulse but before the CCW pulse. The CCW pulse has further to travel before reaching the TWSLA and reaches the TWSLA a time t_{asy} seconds later. Figure 5.16 shows the timing diagram associated with the ASLALOM demultiplexing action.

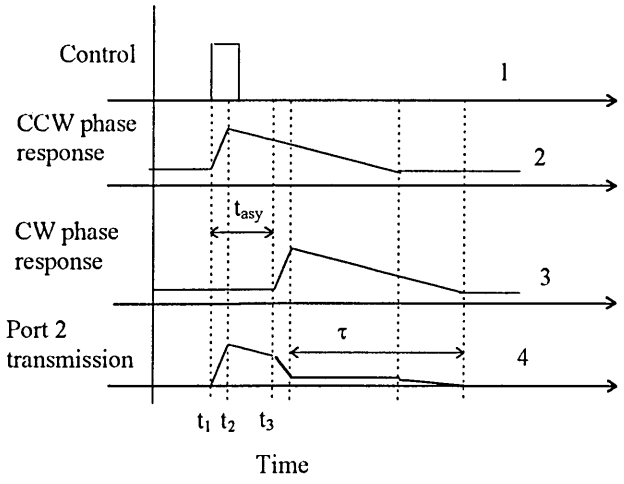

Figure 5.16 Timing diagram for demultiplexing of data in ASLALOM.

Graph 1 shows the control signal which is input to the system at a time t_1. The TWSLA is saturated by the control pulse and undergoes a gain and index change with a relatively short rise time (≈ few ps) and reaches a peak at t_2. A CCW data signal which is coincident with the control signal in the amplifier experiences the phase of the amplifier as shown in graph 2 of the CCW signal, graph 3 shows the CW signal whose phase

change occurs at *t3*. The timing in these graphs is such that a CCW data pulse reaches the TWSLA at the point where the index changes. Note that at this point the CW pulse will have passed through the amplifier at a time increment $\tau_{asy} = 2\Delta x / c_{loop}$ earlier (c_{loop} is the velocity of light in the fibre loop). The CW graph is thus a delayed version of the CCW graph by τ_{asy} seconds. The CW and CCW now have different refractive indices after traversing the loop. If the index change is sufficient to cause a relative phase change of π between CW and CCW pulses then interference occurs at the coupler causing transmission and not reflection and a pulse will then exit via port 2. Thus the difference in time between the two responses has opened a transmission window. A general condition of system operation is that the frame period T_{frame} of an OTDM signal has to be larger than the TWSLA recombination time and the bit period T_{bit} less than the recombination time i.e. $T_{bit} \ll T < T_{frame}$. It can be seen from graph 4 a time window of about $\Delta\tau_{asy}$ seconds has been created i.e. the time delay between CW and CCW signals. The switch definition is thus determined by how close the TWSLA is placed to the loop centre.

5.4. Summary.

This chapter has dealt with the progress of OTDM systems for multiplexing and demultiplexing. With reference to WDM systems which are currently examined in European and US networks, OTDM is seen as a viable alternative to WDM. However the components and systems are confined to the laboratory. As demonstrated, promising results are being produced for OTDM systems in a number of applications. It is of continuing importance to develop system models to complement the practical

work and use in the implementation of future networks. A major point to evolve from this review is the importance of the ASLALOM as a TDM component for future networks in terms of switching speed, power requirements and the possibility of integration with other optoelectronic devices. Table 5.2 summarises the main methods of OTDM demultiplexing.

Type	Control	NLE	Outputs	Data rate switched	Reference
FWM	380 mW, 5.3 ps	Optical fibre	1	100 Gbit/s	[Morioka 94]
NOLM	1.01 W Pk., 5.4 ps data	Optical fibre	1	100 Gbit/s	[Uchiyama 94]
SLALOM	250 pW, 10 ns data	TWSLA	1	50 Gbit/s	[O'Neill 90]
ASLALOM	800 0, 1 ps	TWSLA	1	250 Gbit/s	[Glesk 94]

Table 5.2 Optical demultiplexers.

Chapter 6.

Modelling Of A Travelling Wave Semiconductor Laser Amplifier

6.1 Introduction

This chapter describes work undertaken by the author in the development of computer models of TWSLAs. The models can be broadly divided into continuous wave input and pulsed input. The continuous wave model is further divided into an analytical solution and a numerical solution. The pulsed input model is described by a point element and a finite length model. The software package MATLAB™. was used for all simulations. Simulations of the various models are carried out and the results analysed.

6.2 Input Signal Modulation Time and Saturation Intensity

When modelling TWSLAs consideration must be given to the modulation time in relation to the carrier dynamics of the device and whether the amplifier is in the saturation region or not. When the amplifier is unsaturated the amplifier carrier density is constant and signals of any shape are amplified undistorted. Figure 3.7 depicts a typical gain curve showing the onset of saturation. In the saturated region the carrier density varies according to the light intensity and consequently signal gain and phase are significantly affected. Thus when the signal intensity approaches the saturation level signal distortion can occur and the signal amplifier dynamics need to be assessed.

Three situations are to be considered when signal saturation occurs.

(i) The temporal response of the input signals is much slower than the carrier lifetime.

In this case the carrier density will respond instantaneously to the input signal and no signal distortion takes place for pulse signals.

(ii) The change in light intensity is sufficiently faster than the recombination time, in this case the carrier density will settle to value determined by the average input power of the signal and again no signal distortion occurs.

(iii) The pulse rate is of the same order as the carrier lifetime. In this case the carrier density is allowed to recover between signals. The leading edge of the pulse receives high amplification due to the high carrier density. If saturation is regarded as instantaneous the carrier density quickly approaches saturation and pulse distortion occurs because of a different gain over the pulse width.

6.3 Continuous Wave And High Data Rate Models

6.3.1 Steady state simulations

For a high bit rate time division multiplexed system the data signal will satisfy condition (ii) above and a steady state solution can be implemented. The steady state method allows the carrier density to settle to a background value for the control signal.

The steady state solution arises from the following situations;

a) Continuous intensity signal with a slow variation in signal as mentioned in 6.2 (i) above, b) fast pulse stream as in 6.2 (ii) above.

In a pulsed data system the signal is modelled as a continuous intensity signal which, when given a pulse with power P(t), the equivalent signal wave power is:

$$P_{AV} = \frac{1}{T}\int_0^T P(t)dt = \frac{E_s}{T} \qquad (6.1)$$

6.3.2 Analytical solution

The carrier density rate equation introduced in chapter three, is used as an initial basis for the modelling of a TWSLA. The exact form is:

$$\frac{dn(z,t)}{dt} = \frac{j}{ed} - \frac{1}{\tau_2} - \frac{\Gamma a(n-n_o)I(z,t)}{E_p} \tag{6.2}$$

where n(z,t) is the space and time dependent carrier density and I the signal intensity. A simple analysis of a TWSLA can be performed with reference to a change in carrier density. In this instance polarisation, spontaneous emission noise and spectral analysis are not considered. A simple analytical solution can be written by considering a steady state signal. Re-writing the rate equation in terms of the initial carrier density with zero input n_i, and saturation intensity $I_{sat} = E/\Gamma a\tau$ gives:

$$\frac{n_i - n}{\tau_2} = \frac{n - n_0}{I_{sat}} I_c \tag{6.3}$$

and the carrier density settles to a value:

$$n = \frac{n_i + \dfrac{I}{I_{SAT}} n_0}{1 + \dfrac{I}{I_{SAT}}} \tag{6.4}$$

Subtracting this from the initial condition value gives:

$$\Delta n = \frac{n_i - n_0}{1 + \dfrac{I_{sat}}{I}} \tag{6.5}$$

In this case Δn is assumed constant throughout the device length. Equation 6.5. is a simple intuitive model and does not consider the signal amplification along the TWSLA.

6.3.3 Numerical solution

In this method the amplifier is divided into discrete lengths (see figure 6.1).

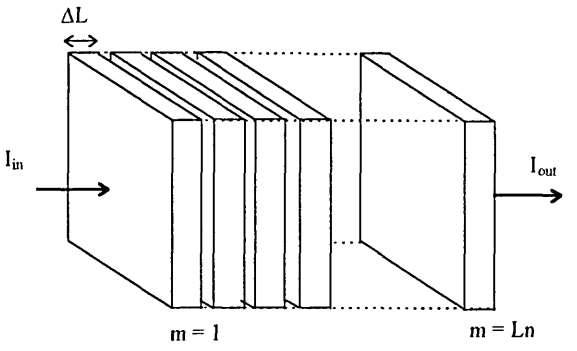

Figure 6.1 TWSLA segments for modelling purposes

Before signal input the carrier density in each segment is set to a value determined by the bias current of the device. The rate equation settles to a steady state and the initial carrier density throughout every segment of the device is given by:

$$n_i = \frac{j\tau}{ed} \tag{6.6}$$

Consider then a wavefront incident on the first segment $m = 1$. The signal is amplified over the segment length according to:

$$I_{m+1} = I_m \exp(\Gamma(a(n_{m=1} - n_0))\Delta l) \tag{6.7}$$

For very small increments in length the amplifier section is described as a single point and the rate equation is used to describe local effects of carrier density. The carrier density in the first section is then found by a numerical solution of the following equation to give a value for n at $m = 1$:

$$\frac{j}{ed} = \frac{n}{\tau} + \frac{\Gamma a(n - n_0)}{E}(I_{m+1} = I_m \exp(\Gamma(a(n_{m=1} - n_0)))\Delta l) \tag{6.8}$$

Equation 6.8 is solved numerically using a bisection algorithm [Lindfield and Perry 95] and gives the spatial information on carrier density at a single point m. For the next

segment the incident wavefront is an amplified version given from equation 6.7. The process is continued until the end segment is reached. The overall gain of the device is calculated by multiplying all the individual element gains i.e.;

$$I_L = I_m[\exp(n_m - n_0)\times\Delta L\times \exp(n_{m+1} - n_0)\times\Delta L \ldots \exp(n_{Ln} - n_0)\times\Delta L] \quad (6.9)$$

which can be written as the sum:

$$G = \exp\sum_{m=1}^{L_n} \Gamma a(n - n_0)\Delta L \quad (6.10)$$

Simulations using numerical solution

Figure 6.2 shows a plot of the carrier density normalised to the zero input value against the number of amplifier segments (L_n = 100) , the input is a pulse train with a frequency of 250 GHz and pulse width 1 ps satisfying condition 6.2 (ii). The TWSLA parameters are given in table 6.1.[e.g. Manning and Davies 94],

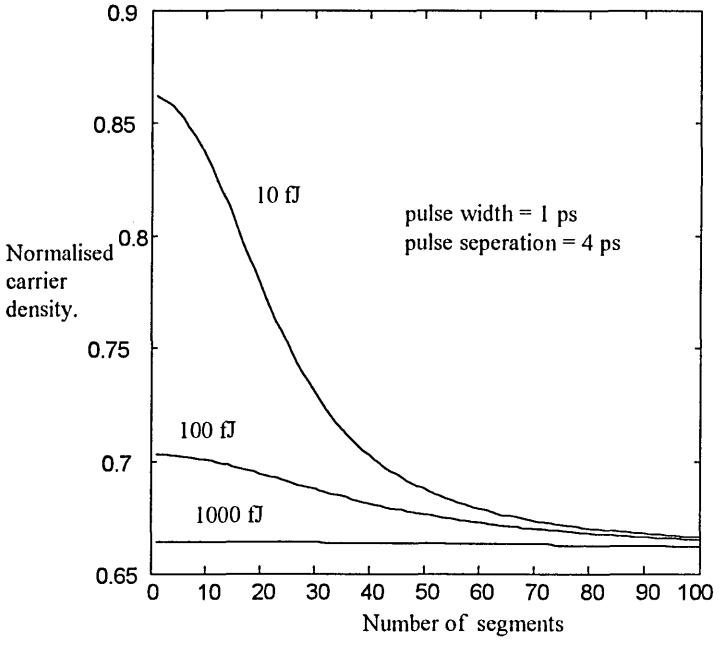

Figure 6.2 Discrete amplifier model carrier density v. segment number.

Parameter	Value
Γ (confinement factor)	0.3
j (current density)	$60\times10^{6}Am^{-3}$
a (gain coefficient)	$2.7\times10^{-20}m^{2}$
d (active layer depth)	$0.2\times10^{-6}m$
e (electronic charge)	$1.6\times10^{-19}C$
E (photon energy)	0.8 eV
L (amplifier length)	$500\times10^{-6}m$
n_0 (transparency density)	$1.0\times10^{24}m^{-3}$
w (active layer width)	$2.0\times10^{-6}m$

Table 6.1. TWSLA parameters

With low energy input (10 fJ) the carrier density reaches its lowest value towards the end of the device where the input signal will be considerably amplified. Increasing the input (100 fJ) brings the saturation point (say 0.67 kJ) nearer to the beginning of the amplifier. In both these cases the model describes an important point in that the carrier density is a function of position which is an important consideration in the ASLALOM analysis (section 7.5.3) . A further increase in energy (1000 fJ) brings about immediate saturation of the device with an almost constant carrier density along the length co-ordinate. A comparison with results given in [Gillner 92] show agreement with the shape of the plots in figure 6.2, and the point where the curve becomes flat (1000 fJ in figure 6.2) which occurs at the transparency density in both cases.

6.3.4 Analytical v numerical solution

The analytical model is a mathematically simple and a non-intense method computationally. However it does not give an accurate picture of the carrier dynamics because the input intensity is constant throughout the device length and assumes a constant carrier density along the length of the TWSLA. It is instructive however to compare this method with the numerical solution to assess its usefulness in simulations.

Figure 6.3 depicts the average carrier density in the amplifier when a continuous wave signal is input for both methods

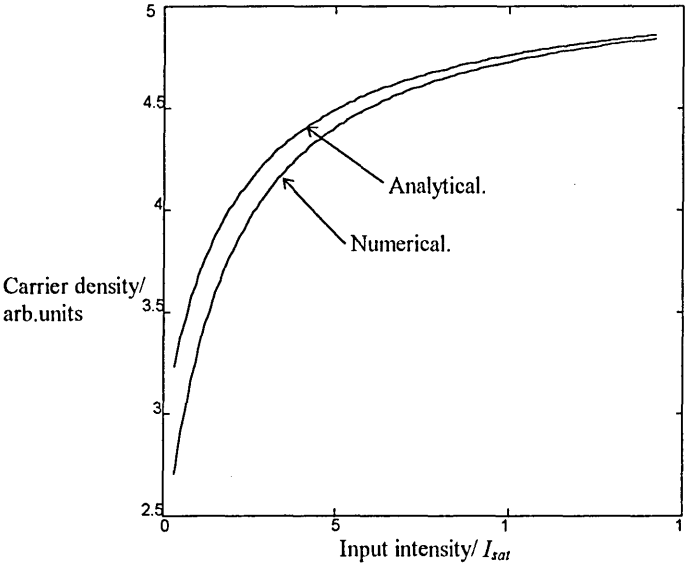

Figure 6.3. Analytical v numerical solution of rate equation.

From figure 6.3 it can be seen that the steady state carrier density is approaching equal values for both methods towards higher values of input intensity. An explanation of this can be given by realising that the carrier density and thus the gain at high values of input intensity is constant (see figure 6.2).

6.4 Dynamic (pulse) Input Analysis

6.4.1 Dynamic modelling of picosecond pulse inputs.

Referring back to figure 6.1 and considering the case where a point on a pulse wavefront is incident on an amplifier segment with a carrier density given as $n(z_{1m})$, the pulse point is amplified according to equation 6.7. If small segments are considered then the rate equation is used to describe the local effects of signal input but this time the rate equation is solved for a particular time increment, as opposed to the steady state

equation 6.8. The amplified signal is then input to the next segment where it again undergoes amplification according to the initial conditions present. At this moment a particular point on the pulse profile is all that is considered and this will propagate through the device taking a time equal to L/c_N, at intervals given by $\Delta L/c_N$. The pulse is continuous in time and space therefore the next point on the pulse profile will follow and undergo amplification, and cause stimulated emission as per the previous point but with the carrier density conditions imposed by the previous pulse point. The carrier density change is again calculated in each segment. Using this procedure each point on the pulse profile will describe the carrier density at successive amplifier points and times. The equations to describe pulse propagation are a density rate equation and a dynamic propagation equation which are re-written here:

$$\frac{dn(z,t)}{dt} = P_i - \frac{n(z,t)}{\tau} - \frac{\Gamma}{E} a(n-n_0) I(z,t) \tag{6.11}$$

$$\frac{\partial I(z,t)}{\partial z}\frac{1}{v_g} + \frac{\partial I(z,t)}{\partial t} = a(n-n_0) I(z,t) \tag{6.12}$$

6.4.2 Longitudinal averaging method (Point element model)

A simplification in the analysis of pulse amplification is to make a substitution of variable where $T \equiv z/v_g$ [Agrawal and Olsson 89] equations 6.11 and 6.12 can then be written as:

$$\frac{dn(z,T)}{dt} = P_i - \frac{n(z,T)}{\tau} - \frac{\Gamma}{E_p} a(n-n_0) I(z,T) \tag{6.13}$$

$$\frac{\partial I(z,T)}{\partial z} = a(n-n_0) I(z,T) \tag{6.14}$$

Next an average value of carrier density over the device length is defined as:

$$n_{av}(T) = \frac{1}{L}\int_0^L n(z,T)dz \tag{6.15}$$

where n_{av} represents the average value of carrier density in the device after a point on the pulse has propagated through and reaches the end segment of the amplifier at a time T. Substituting equation 6.14 and 6.15 into equation 6.13 gives:

$$\frac{dn_{av}(T)}{dT} = P_i - \frac{n_{av}(T)}{\tau} - \frac{\Gamma}{E_p}\frac{\partial(z,T)}{\partial T} \tag{6.16}$$

Equation 6.16 is then integrated over the device length and the mean value is found giving:

$$\frac{dn_{av}(T)}{dT} = \frac{P_i L}{L} - \frac{n_{av}(T)}{\tau} - \frac{\Gamma}{E_p L}(I_{out}(T) - I_{in}(T)) \tag{6.17}$$

Equation 6.14 can also be integrated over the device length by using the substitution $n = n_{av}$ where n_{av} is a constant thus:

$$I_{out}(T) = exp(a(n_{av}(T) - n_0)L \tag{6.18}$$

Substituting 6.18 into 6.17 gives

$$\frac{dn_{av}(T)}{dT} = P_i - \frac{n_{av}(T)}{\tau} - \frac{\Gamma}{E_p} I_{in}(T)(\exp(a(n_{av} - n_0)) \tag{6.19}$$

which can be used to solve for the average value of carrier density for each point of the input signal. In a similar way to the continuous analysis each point on the pulse profile $I(T)$ is input to equation 6.19. To compute the pulse temporal response the pulse is discretised into small time elements equal to Δt. Initially $I_{in}(\Delta T)$ is substituted into equation 6.19 which is then integrated to give the carrier density at a time ΔT . The method of solution then is to consider a Taylor series of the carrier density i.e.

$n(T + \Delta T) = n(T) + n'(T)\,\Delta T + \Delta T^2 n''(T)/2! + \ldots\, \Delta T^m n^m(T)/m! + \ldots$ (n(T + ΔT))

which can be substituted into equation 6.19 to find the carrier density at the next time interval ($T + \Delta T$). The process is continued until the last point on the pulse is reached. A

truncated form of a Taylor series can be used (Euler's method) which uses the derivative of n up to the first order i.e.

$$n(T + \Delta T) = n(T) + n'(T)\,\Delta T. \tag{6.20}$$

6.4.3 Point element model simulations

In the previous analysis the amplifier is effectively a point element approximation and any spatial information is ignored. Here the carrier density changes is assumed to occur instantaneously over the whole length of the amplifier. Therefore, the full modulation occurs over a time equal to the pulse width. This method leads to a simple analysis and simple solutions are afforded when the carrier density is assumed to be constant over the entire device length L. Simulations of pulse input will be investigated using an unchirped Gaussian pulse of the form:

$$P = \frac{E_{in}}{\tau_0\sqrt{\pi}}\exp\left(-\frac{t^2}{\tau_0^2}\right) \tag{6.21}$$

where E_{in} is the pulse input energy and τ_0 is related to the FWHM by $\tau_p = 1.665\tau_0$. This shape is characteristic of pulses generated from actively mode locked lasers [Guy et al 96] and is a method commonly used for OTDM signals e.g. [Morioka et al 94], [Nakazawa et al 95] and [Joergensen et al 96]. Figure 6.4 shows a typical pulse using equation 6.20.

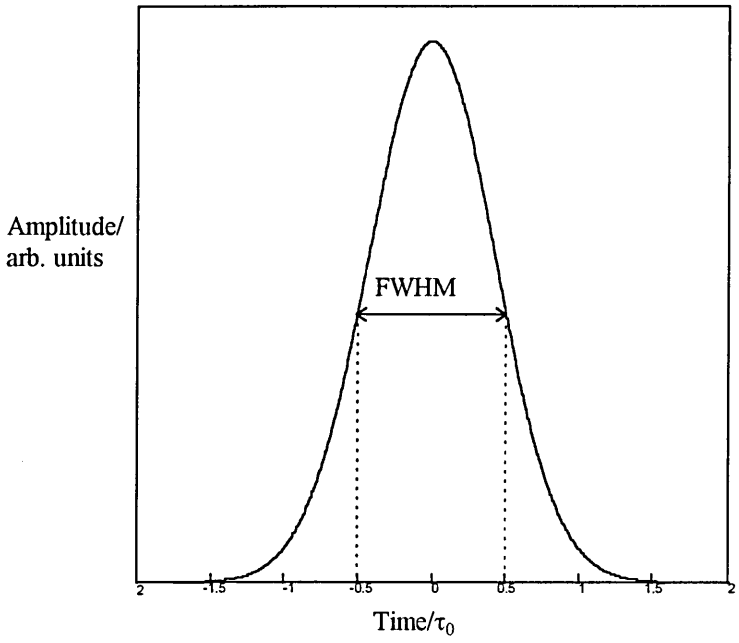

Figure 6.4. Gaussian pulse.

Using equation 6.19 and 6.20 a Gaussian input of the form of equation 6.21 with E_{in} = 800 fJ is input. TWSLA parameters are as in table 6.1. The temporal response of the carrier density normalised to the steady state is shown in figure 6.5.

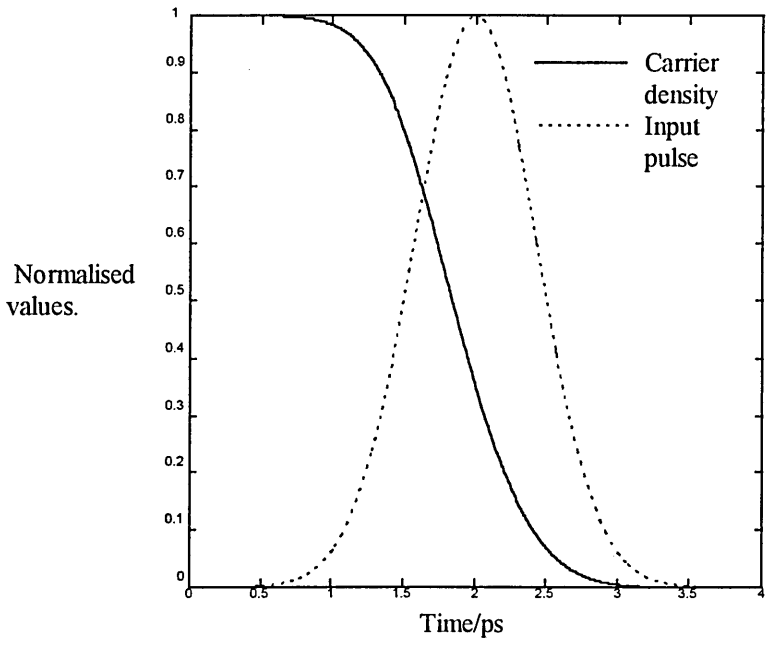

Figure 6.5 Carrier density response to pulse input.

The dynamics of figure 6.5. exhibit a turn on time of around 1.5 ps which is associated with the slope of the Gaussian pulse which has a FWHM of 1 ps. From experimental observations on gain dynamics a slope is evident on the pump probe results, for example a rise time of ≈ 4 ps indicated for 2 ps input pulses [Hong et al 94]. For InGaAsP amplifiers the rise time is shown to be ≈ 20 ps for a 15 ps pulse [Lai et al 90]. The slope is a feature of TWSLA dynamics and its effect on the response of an ASLALOM will be discussed in chapter 7.

Index of refraction and phase

Associated with the carrier density change is a variation in the refractive index of the material and is given by the equation [Lomax and White 91]:

$$N(T) = N_0 - \frac{dN}{dn}(n(T) - n_1) \tag{6.22}$$

where $N(T)$ is the refractive index, N_0 the refractive index with no signal applied, $n_{av}(T)$ the carrier density from equation 6.19, n_1 the carrier density with no signal applied and dN/dn the refractive index carrier density differential coefficient. The phase propagation of a wave travelling with a wavelength λ is found by making the substitution

$$\phi = \frac{2\pi NL}{\lambda} \tag{6.23}$$

giving:

$$\phi = \frac{2\pi L}{\lambda}\left(N_0 - \frac{dN}{dn}(n - n_1)\right) \tag{6.24}$$

For a guided wave system with a confinement factor Γ [Manning et al 94] the relative phase change is more appropriate for switching applications giving

$$\Delta\phi = \frac{dN}{dn} \cdot \frac{2\pi L(n - n_1)}{\lambda} \tag{6.25}$$

The value of *dN/dn* is actually a function of photon energy and Westbrook [Westbrook 86] gives values for different photon energies. In this case the wavelength of the input signal is assumed to be 1550 nm with a corresponding photon energy of 0.8 eV. The value of *dN/dn* for this energy is 2×10^{-26} m^3 [Manning and Davies 94]. Using equation 6.25 and the carrier density values as in figure 6.5 the temporal phase response is shown in figure 6.6.

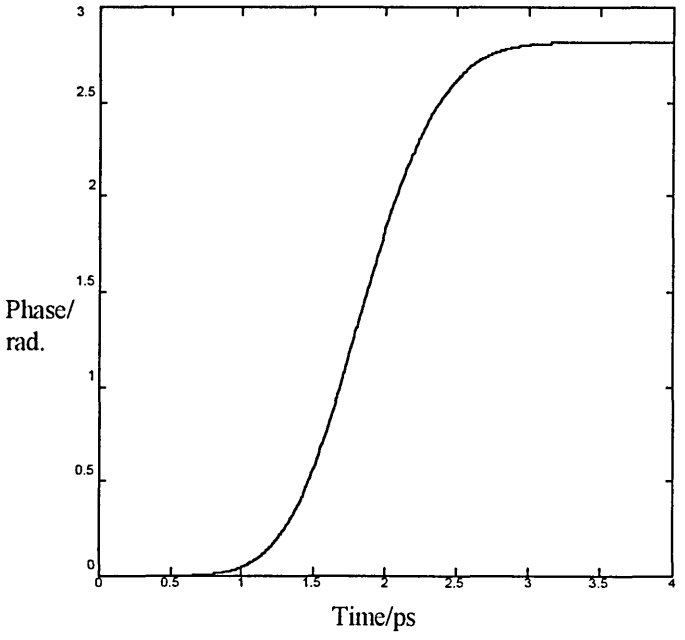

Figure 6.6 Phase response with pulse input.

The corresponding gain response is shown in figure 6.7. calculated from:

$$G(T) = \exp(\Gamma a(n_{av}(T) - n_0)L) \qquad (6.26)$$

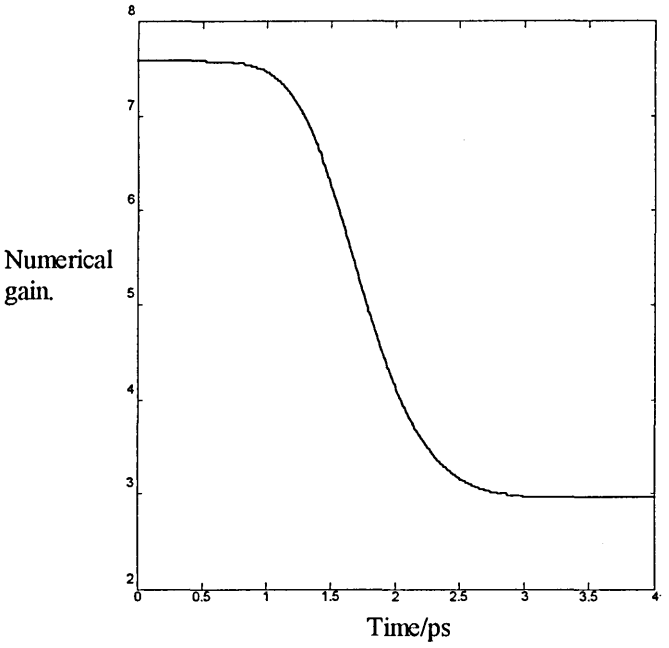

Figure 6.7 Gain response with pulse input.

A validation on the point element model presented can be made by comparing simulations from equations 6.19, 6.20, 6.21 and 6.26 with the results presented in [Eiselt 95]. Simulations are made with an unsaturated amplifier gain of 100 and a 50 fJ input pulse and show a saturated gain value of 30 which is within 16% of Eiselt's [Eiselt 95] value of 25. Phase response was not studied in this reference but as both gain and phase are functions of carrier density (equations 6.25 and 6.26). The phase response is assumed valid. The temporal response in both cases shows a relaxation time of the order of τ_2, the recombination time.

Pulse distortion

The pulse is amplified according to the carrier density dynamics and equation 6.26. The pulse shape in figure 6.8 shows the pulse entering the amplifier (input) and leaving (output).

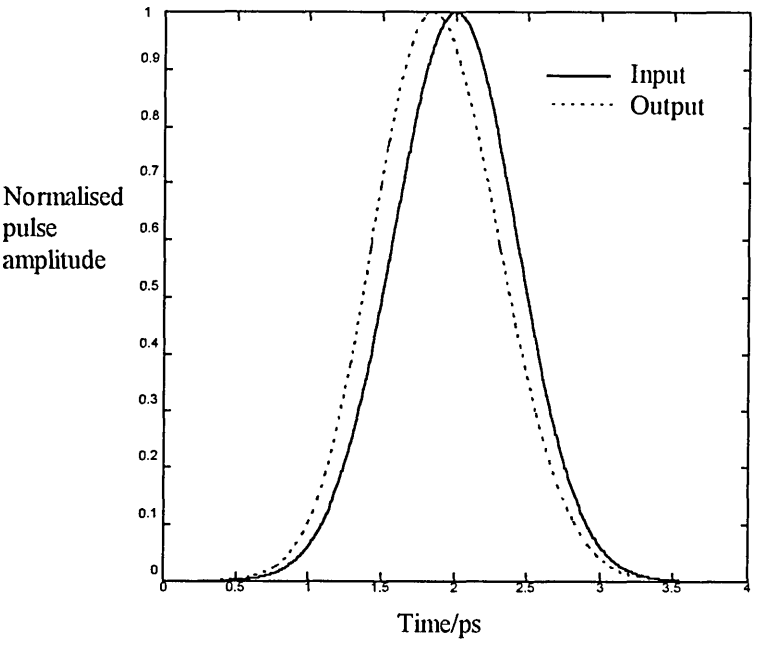

Figure 6.8 Pulse distortion in saturated TWSLA.

Pulse distortion is evident with the leading edge receiving a higher gain (≈ 7.5) due to the gain saturation and the trailing edge receiving a reduced gain (≈ 3) as it propagates through the TWSLA. The occurrence of pulse distortion is in agreement with predictions of leading edge pulse gain by [Agrawal and Olsson 89] and further validates the point element model.

6.4.4 Finite length model

The previous analysis treated the amplifier as a point element within the loop contributing an attenuation and phase shift at one spatial position. More accurate analysis must take into account the length of the device and the propagation of the pulse at a defined interval with the accompanying attenuation and phase shift at that position. Initially the amplifier is split into sections of equal length, $\Delta L = L/L_m$, where L_m is the number of segments, the carrier density in each section being stored as a matrix. The incoming pulse is also divided into sections with a time interval of $\Delta L/c_n$, where c_n is the

speed of light in the amplifier, also stored as a matrix. The pulse enters the amplifier at z = 0 with the leading edge element of the pulse matrix lining up with the first element of the carrier density matrix. The rate equation is in matrix form as:

$$\begin{bmatrix} \dot{n}_{(1,k)} \\ \dot{n}_{(2,k)} \\ \dot{n}_{(3,k)} \\ . \\ \dot{n}_{(m,k)} \end{bmatrix} = \frac{j}{ed} - \begin{bmatrix} n_{(1,k)} \\ n_{(2,k)} \\ n_{(3,k)} \\ . \\ n_{(m,k)} \end{bmatrix} [\tau_2]^{-1} - \frac{\Gamma a}{E} \left\{ \begin{bmatrix} n_{(1,k)} \\ n_{(2,k)} \\ n_{(3,k)} \\ . \\ n_{(m,k)} \end{bmatrix} - n_0 \right\} \begin{bmatrix} I_{(1,k)} \\ I_{(2,k)} \\ I_{(3,k)} \\ . \\ I_{(m,k)} \end{bmatrix} \tag{6.27}$$

Equation 6.27 is solved for the carrier density at each point along the amplifier length. The next step to be considered is the pulse propagation from one section to the other. For example the intensity matrix which experiences amplification such that $\mathbf{I}_{(k+1)} \rightarrow \mathbf{I}(k)\exp(\Gamma a(\mathbf{n}(\mathrm{k}) - n_0)\Delta L$ This process is continued until the whole pulse matrix has propagated through the amplifier length a time (t_n)equal to L/n_c plus the pulse width. The resulting carrier density matrix is written as:

$$\begin{matrix} n_{(1,1)} & n_{(1,2)} & n_{(1,3)} & . \\ n_{(2,1)} & . & . & . \\ n_{(3,1)} & . & . & . \\ . & . & . & n_{(L_m,t_n)} \end{matrix} \tag{6.28}$$

6.4.5 Finite length model simulations

Figure 6.9 shows the results of a pulse input of 800 fJ 1 ps to the TWSLA where the pulse energy is enough to saturate the device.

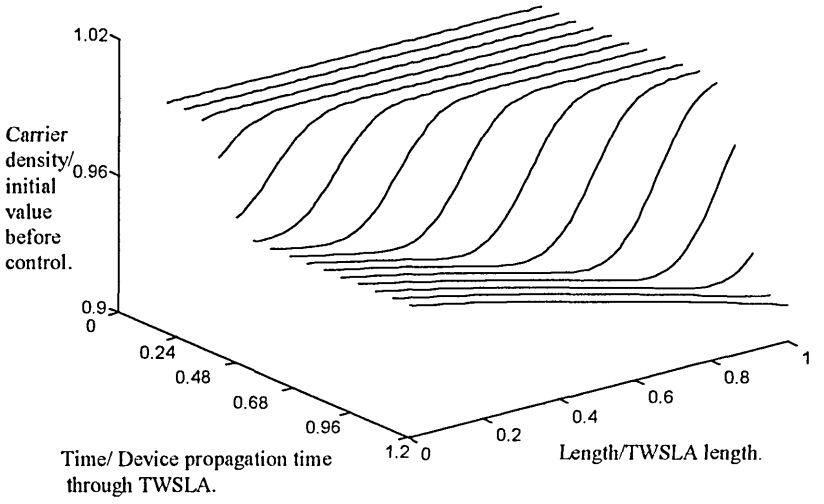

Figure 6.9 Finite length model of pulse input to TWSLA.

The plot gives carrier density information at any position and time. The plots show the carrier density over the length from a time zero when the front edge of the pulse meets the beginning of the TWLSA to a final time when the trailing edge of the pulse leaves the TWSLA. The results clearly identify the carrier depletion as the pulse propagates through the device. The plots give a pictorial representation of the carrier density with rows representing the length axis and columns the time axis. At the moment no practical results are available to compare with the finite length model. A validation will be reserved until the model is used in conjunction with an ASLALOM (section 7.5.3.4).

6.4 Summary

This chapter has presented various models of a TWSLA as developed by the author. The models are broadly divide into two categories continuous wave and dynamic (pulse) input models. The continuous wave proves to be the simplest and both an analytical and

a numerical method described. The analytic method is the simpler and becomes more accurate with high values of input power. The intention of the continuous model is to simulate a high data rate signal as in an OTDM system. A dynamic model is described next with a point element model which assumes the TWSLA has zero dimensions and occupies a single point in space and describes temporal variations only. The corresponding phase change due to the input is described with a refractive index equation dependent on carrier density. Comparisons with practical results are made in each case, the continuous wave model agrees in shape with regard to carrier density distribution along the amplifier length. The point element model is validated temporally with the fall time of the transmission response corresponding with practical results, also gain saturation is compared and is found to be within ≈16% of a reported value. A more comprehensive model is described next which includes temporal and spatial information of the TWSLA. Comparisons of this model are not made at this stage but will be addressed in chapter 7.

Chapter 7

Modelling And Simulation of ASLALOM

7.1 Introduction

This chapter describes models developed by the author to simulate the de-multiplexing action of the ASLALOM as introduced in chapter 5. For modelling purposes the ASLALOM can be described as three components a fibre coupler, a fibre loop and a non-linear element (TWSLA). Models of the TWSLA have been described in chapter 6. The first functional component to be modelled is the input-output coupler. The fibre loop will be assumed initially to consist of a simple time delay until a later section when polarisation and birefringence effects will be considered. Fundamental to loop operation is the asymmetry of the TWSLA and the effect of this will be considered highlighting the need for different TWSLA models. Equations to describe the special case of small asymmetry are developed in section 7.5.3. and loop performance will be investigated by looking at the switching resolution of the system and adjacent pulse crosstalk will be taken into account. The use of a high frequency control pulse is modelled which leads to the use of an ASLALOM with data input which can be used for wavelength conversion, and also looks at patterning. A novel application of the system for multi-channel output will be presented. A model is also developed to simulate the effects of polarisation and birefringence in an ASLALOM.

7.2 Modelling of fused fibre coupler

Fused fibre couplers play an integral part in all types of loop mirror. Coupling action takes place through the interaction of modes along a section of optical fibre. The coupling section is formed by heating a length of two adjacent fibres and elongating to form a tapered fibre with a narrowed length. Coupled mode equations are generally used to describe the coupling between the modes of the signal. Generally the coupler has polarisation [Schliep 94] and wavelength dependencies.

Consider an electric field at the input of a coupler. See figure 7.1.

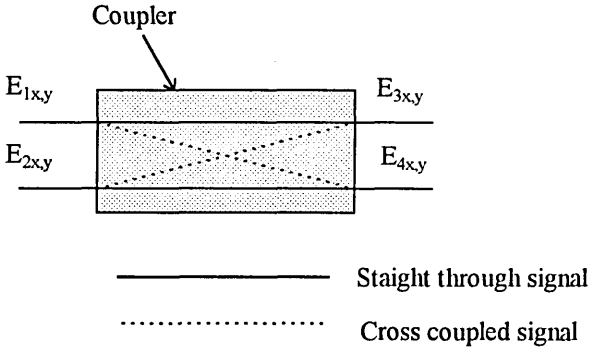

Figure 7.1 Ray diagram of fused fibre coupler.

The transfer function from coupled mode theory is as follows [Mortimore 88]:

$$\begin{bmatrix} E_{3x,y} \\ E_{4x,y} \end{bmatrix} = \sqrt{1-\gamma} \begin{bmatrix} \alpha_{(1,3)} & \alpha_{(2,3)} \exp(j\delta) \\ \alpha_{(1,4)} \exp(j\delta) & \alpha_{(2,4)} \end{bmatrix} \begin{bmatrix} E_{1x,y} \\ E_{2x,y} \end{bmatrix} \tag{7.1}$$

where $\alpha_{x(m,n)}$ and $\alpha_{y(m,n)}$ are field coupling coefficients of a signal propagating from port m to port n for the x and y polarisations of the electric field respectively and are related to the intensity coupling coefficient K by $\delta = K^{1/2}$, γ represents the proportion of power loss through the coupler, $\delta_{(x,y)}$ is the phase shift imposed on a cross coupled signal relative to the straight through signal and E_{mx} and E_{my} (m = 1,2,3,4) are the electric field

amplitudes at port *m* for the x and y polarisations. Initial experiments on fused couplers by Cassidy [Cassidy 85] demonstrated the couplers dependence on wavelength. Cassidy performed experiments on couplers using a white light source as an input signal and measured the light output from the coupler as a function of wavelength. These experiments showed that the coupler transmission has a periodic response with maximum and minimum values of wavelength for either port. The wavelength dependence can be described by a raised cosine function by making the following substitutions into equation 7.1:

$$\alpha_{(1,3)} = \alpha_{(2,4)} = \left(\frac{1}{2}\left(1+\cos\left(\frac{\pi(\omega-\omega_u)}{(\omega_u-\omega_l)}\right)\right)\right)^{1/2} \tag{7.2}$$

$$\alpha_{(2,1)} = \alpha_{(1,2)} = \left(1-\frac{1}{2}\left(1+\cos\left(\frac{\pi(\omega-\omega_u)}{(\omega_u-\omega_l)}\right)\right)\right)^{1/2} \tag{7.3}$$

where ω is the signal wavelength, ω_u and ω_l are upper and lower wavelength minima of the transmission spectra of the coupler which can be determined experimentally. Using equations 7.1, 7.2 and 7.3 the transmission response of figure 7.2 can be simulated.

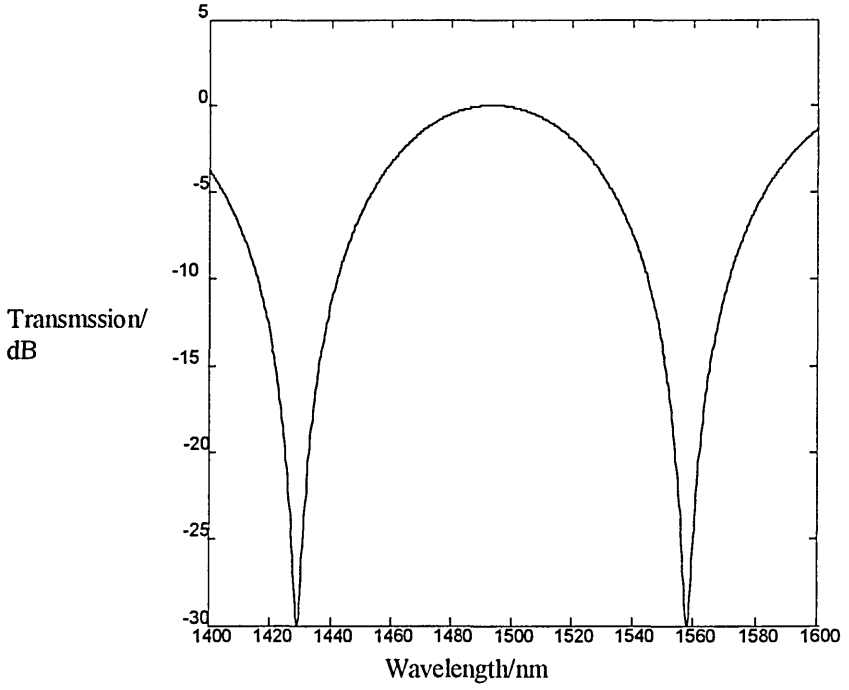

Figure 7.2 Simulated coupler transmission v. wavelength of signal.

In figure 7.2 ω_u and ω_l are chosen as 1429 nm and 1558 nm for the maxima and minima of the straight through transmission respectively which are the values given for a practical device in [Morishita 95]. The simulation of figure 7.2 shows excellent agreement with the coupler in [Morishita 95]. The detraction from an ideal coupler is shown as a small value of transmission (-30 dB) at the minimal transmission wavelengths. This is attributable to non-equal coupling coefficients and has been modelled by adjusting these accordingly.

7.3 Matrix Analysis Of Propagation Through ASLALOM

7.3.1 Matrix equation

For ease of understanding the loop mirror can be broken down into a series of propagation components with individual field transfer functions. Following the signal from the input port through the coupler around the loop and returning through the coupler the following equations can be written (see figure 7.3, note: the control pulse has been omitted). Here it is taken that the fields are representative of a travelling wave signal $E(z,t)$ of amplitude E_1, radian frequency ω, arbitrary phase shift φ and propagation constant k, i.e.,

$$E(z,t) = E_1 \exp(j(\omega t - kz - \varphi)). \tag{7.4}$$

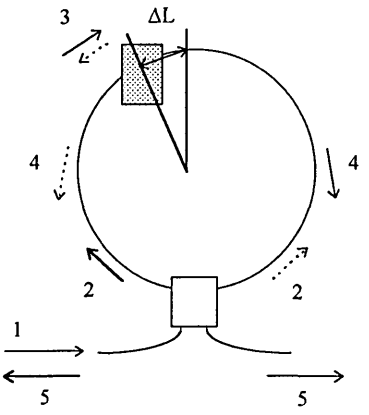

Figure 7.3 ASLALOM as series of propagation components.

The following equations can be written (port numberings as in figure 7.1):

1. Propagation through coupler (input)

$$\begin{pmatrix} E_3 \\ E_4 \end{pmatrix} = \begin{pmatrix} \alpha_{1,3} & \alpha_{2,3}\exp(j\delta) \\ \alpha_{1,4}\exp(j\delta) & \alpha_{2,4} \end{pmatrix} \begin{pmatrix} E_1 \\ E_2 \end{pmatrix} \tag{7.5}$$

2. Propagation through fibre to TWSLA

$$\begin{pmatrix} E_3 \\ E_4 \end{pmatrix} = \begin{pmatrix} \exp\left(\dfrac{j2\pi N_f (L-\Delta L)}{\lambda_s}\right) & 0 \\ 0 & \exp\left(\dfrac{j2\pi N_f (L+\Delta L)}{\lambda_s}\right) \end{pmatrix} \begin{pmatrix} E_3 \\ E_4 \end{pmatrix} \tag{7.6}$$

3. Propagation through TWSLA

$$\begin{pmatrix} E_3 \\ E_4 \end{pmatrix} = \begin{pmatrix} F_{CW} & 0 \\ 0 & F_{CCW} \end{pmatrix} \begin{pmatrix} E_3 \\ E_4 \end{pmatrix} \tag{7.7}$$

4. Propagation from TWSLA to coupler

$$\begin{pmatrix} E_3 \\ E_4 \end{pmatrix} = \begin{pmatrix} \exp\left(\dfrac{j2\pi N_f (L+\Delta L)}{\lambda_s}\right) & 0 \\ 0 & \exp\left(\dfrac{j2\pi N_f (L-\Delta L)}{\lambda_s}\right) \end{pmatrix} \begin{pmatrix} E_3 \\ E_4 \end{pmatrix} \tag{7.8}$$

5. Propagation through coupler (output)

$$\begin{pmatrix} E_1 \\ E_2 \end{pmatrix} = \begin{pmatrix} \alpha_{4,1} \exp(j\delta) & \alpha_{3,1} \\ \alpha_{4,2} & \alpha_{3,2} \exp(j\delta) \end{pmatrix} \begin{pmatrix} E_4 \\ E_3 \end{pmatrix} \tag{7.9}$$

In the above $2L$ is the length of the fibre loop, λ_s is the signal wavelength, N_f the refractive index of the fibre, F_{CW} and F_{CCW} the gain and phase functions of the TWSLA in the CW and CCW directions respectively. The various components can be brought together to give a matrix description of the loop thus:

$$\begin{bmatrix} E_{1x} \\ E_{1y} \\ E_{2x} \\ E_{2y} \end{bmatrix} = \begin{bmatrix} m_{11} & m_{12} & m_{13} & m_{14} \\ m_{21} & m_{22} & m_{23} & m_{24} \\ m_{31} & m_{32} & m_{33} & m_{34} \\ m_{41} & m_{42} & m_{43} & m_{44} \end{bmatrix} \begin{bmatrix} E_{1x} \\ E_{1y} \\ E_{2x} \\ E_{2y} \end{bmatrix} \tag{7.10}$$

The effects of phase and amplitude in the loop can be tabulated (see table 7.1) to give values for the matrix elements where $\phi_S = 2\pi(L - \Delta L)N_f/\lambda$, $\phi_L = 2\pi(L + \Delta L)N_f/\lambda$, ϕ_{CW} and ϕ_{CCW} the TWSLA CW and CCW phase shifts, G_{CW} and G_{CCW} the TWSLA CW and CCW

power gains, $\phi_{\parallel}$ and ϕ_x are the phase shifts for through and cross coupling of the coupler and α_F, is the fibre absorption coefficient.

Matrix element	CW	CCW
$m_{11}(E_{1x}\rightarrow E_{1x})$	$(\alpha_{1,3}\alpha_{4,1}(G_{CW})^{1/2}.exp(-\alpha_F L - j[\phi_{\parallel} + (\phi_S + \phi_{CW} + \phi_L) + \phi_X])$	$(\alpha_{1,4}\alpha_{3,1}(G_{CCW})^{1/2}.exp(-\alpha_F L - j[\phi_x + (\phi_L + \phi_{CCW} + \phi_L) + \phi_{\parallel}])$
$m_{12}(E_{1y}\rightarrow E_{1x})$	Birefringence and polarisation	Birefringence and polarisation
$m_{13}(E_{2x}\rightarrow E_{1x})$	$(\alpha_{2,3}\alpha_{1,3}(G_{CW})^{1/2}.exp(-\alpha_F L - j[\phi_X + (\phi_S + \phi_{NLE\text{-}CW} + \phi_{\parallel}) + \phi_X])$	$(\alpha_{2,4}\alpha_{3,1}(G_{CCW})^{1/2}\exp(.-\alpha_F L - j[\phi_{\parallel} + (\phi_L + \phi_{NLE\text{-}CCW} + \phi_L) + \phi_{\parallel}])$
$m_{14}(E_{2y}\rightarrow E_{1x})$	Birefringence and polarisation	Birefringence and polarisation
$m_{21}(E_{1x}\rightarrow E_{1y})$	Birefringence and polarisation	Birefringence and polarisation
$m_{22}(E_{1y}\rightarrow E_{1y})$	$\alpha_{1,3}\alpha_{4,1}G^{1/2}.exp(-\alpha_F L - j[\phi_{\parallel} + (\phi_S + \phi_{NLE\text{-}CW} + \phi_L) + \phi_X])$	$\alpha_{1,4}\alpha_{3,1}G^{1/2}.exp(-\alpha_F L - j[\phi_x + (\phi_L + \phi_{NLE\text{-}CCW} + \phi_L) + \phi_{\parallel}])$
$m_{23}(E_{2x}\rightarrow E_{1y})$	Birefringence and polarisation	Birefringence and polarisation
$m_{24}(E_{2y}\rightarrow E_{1y})$	$\alpha_{2,3}\alpha_{1,3}G^{1/2}.exp(-\alpha_F L - j[\phi_X + (\phi_S + \phi_{NLE\text{-}CW} + \phi_{\parallel}) + \phi_X])$	$\alpha_{2,4}\alpha_{3,1}G^{1/2}.exp(-\alpha_F L - j[\phi_{\parallel} + (\phi_L + \phi_{NLE\text{-}CCW} + \phi_L) + \phi_{\parallel}])$
$m_{31}(E_{1x}\rightarrow E_{2x})$	$\alpha_{1,3}\alpha_{4,2}G^{1/2}.exp(-\alpha_F L - j[\phi_{\parallel} + (\phi_S + \phi_{NLE\text{-}CW} + \phi_L) + \phi_{\parallel}])$	$\alpha_{1,4}\alpha_{3,2}G^{1/2}.exp(-\alpha_F L - j[\phi_X + (\phi_L + \phi_{NLE\text{-}CCW} + \phi_{IS}) + \phi_X])$
$m_{32}(E_{1y}\rightarrow E_{2x})$	Birefringence and polarisation	Birefringence and polarisation
$m_{33}(E_{2x}\rightarrow E_{2x})$	$\alpha_{2,3}\alpha_{4,2}G^{1/2}.exp(-\alpha_F L - j[\phi_X + (\phi_S + \phi_{NLE\text{-}CW} + \phi_L) + \phi_{\parallel}])$	$\alpha_{2,4}\alpha_{3,2}G^{1/2}exp(-\alpha_F L - j[\phi_{\parallel} + (\phi_L + \phi_{NLE\text{-}CCW} + \phi_{IS}) + \phi_X])$
$m_{34}(E_{2y}\rightarrow E_{2x})$	Birefringence and polarisation	Birefringence and polarisation
$m_{41}(E_{1x}\rightarrow E_{2y})$	Birefringence and polarisation	Birefringence and polarisation
$m_{42}(E_{1y}\rightarrow E_{2y})$	$\alpha_{1,3}\alpha_{4,2}G^{1/2}.exp(-\alpha_F L - j[\phi_{\parallel} + (\phi_S + \phi_{NLE\text{-}CW} + \phi_L) + \phi_{\parallel}])$	$\alpha_{1,4}\alpha_{3,2}G^{1/2}.exp(-\alpha_F L - j[\phi_X + (\phi_L + \phi_{NLE\text{-}CCW} + \phi_{IS}) + \phi_X])$
$m_{43}(E_{2x}\rightarrow E_{2y})$	Birefringence and polarisation	Birefringence and polarisation
$m_{44}(E_{2y}\rightarrow E_{2y})$	$\alpha_{2,3}\alpha_{4,2}G^{1/2}.exp(-\alpha_F L - j[\phi_X + (\phi_S + \phi_{NLE\text{-}CW} + \phi_L) + \phi_{\parallel}])$	$\alpha_{2,4}\alpha_{3,2}G^{1/2}.exp(-\alpha_F L - j[\phi_{\parallel} + (\phi_L + \phi_{NLE\text{-}CCW} + \phi_{IS}) + \phi_X])$

Table 7.1 Loop mirror matrix components.

In the case where the fibre and loop components are free from birefringence and polarisation effects, the x and y components undergo equal amplitude and phase change (*x* components are dependent only on *x* components and *y* on *y*). The matrix can then be written in a simpler form as follows:

$$\begin{bmatrix} E_{1x} \\ E_{1y} \\ E_{2x} \\ E_{2y} \end{bmatrix} = \begin{bmatrix} m_{11} & 0 & m_{13} & 0 \\ 0 & m_{22} & 0 & m_{24} \\ m_{31} & 0 & m_{33} & 0 \\ 0 & m_{42} & 0 & m_{44} \end{bmatrix} \begin{bmatrix} E_{1x} \\ E_{1y} \\ E_{2x} \\ E_{2y} \end{bmatrix} \tag{7.11}$$

The matrix is a comprehensive analysis of the loop and the effects of various field components in the loop can be described by selecting the appropriate element in the field vector. For example to simulate the component reflected from port 1 in the direction of x polarisation the following equation is used (assuming input is to port 1 only):

$$E_{1x} = m_{11}E_{1x} + 0E_{1y} + 0E_{2x} + 0E_{2y} \tag{7.12}$$

Note that the absence of any birefringence effects indicate no contribution from the y direction of polarisation.

7.3.2 Power transmission coefficients

To obtain power transmission consider a field **E** incident on the loop with no input to port 2 (normal operation of ASLALOM) i.e.:

$$\mathbf{E} = \begin{bmatrix} E_{1x} \\ E_{1y} \\ 0 \\ 0 \end{bmatrix} \tag{7.13}$$

after loop transmission the output power can be written as a transmission vector **T** multiplied by the input field vector and noting that the power of a complex wave is written as $(Ee^{j\phi})\times(Ee^{-j\phi})$ where $Ee^{j\phi}$ represents the complex amplitude then:

$$\begin{bmatrix} T_{1x} \\ T_{1y} \\ T_{2x} \\ T_{2y} \end{bmatrix} \begin{bmatrix} E_{1x} * E_{1x} \\ E_{1y} * E_{1y} \\ E_{1x} * E_{1x} \\ E_{1x} * E_{1x} \end{bmatrix} = \begin{bmatrix} (m_{11}E_{1x}) * \\ (m_{22}E_{1y}) * \\ (m_{31}E_{1x}) * \\ (m_{42}E_{1y}) * \end{bmatrix} \begin{bmatrix} m_{11}E_{1x} \\ m_{22}E_{1y} \\ m_{31}E_{1y} \\ m_{42}E_{1y} \end{bmatrix} \tag{7.14}$$

Re-writing equation 7.14:

$$\begin{bmatrix} T_{1x} \\ T_{1y} \\ T_{2x} \\ T_{2y} \end{bmatrix} \begin{bmatrix} |E_{1x}|^2 \\ |E_{1y}|^2 \\ |E_{1x}|^2 \\ |E_{1y}|^2 \end{bmatrix} = \begin{bmatrix} m_{11} * m_{11} \\ m_{22} * m_{22} \\ m_{31} * m_{31} \\ m_{42} * m_{42} \end{bmatrix} \begin{bmatrix} |E_{1x}|^2 \\ |E_{1y}|^2 \\ |E_{1x}|^2 \\ |E_{1y}|^2 \end{bmatrix} \tag{7.15}$$

then **T** can be written as:

$$\begin{bmatrix} T_{1x} \\ T_{1y} \\ T_{2x} \\ T_{2y} \end{bmatrix} = \begin{bmatrix} m_{11} * m_{11} \\ m_{22} * m_{22} \\ m_{31} * m_{31} \\ m_{42} * m_{42} \end{bmatrix} \tag{7.16}$$

7.4 Phase And Gain Responses

7.4.1 Simulation of the loop mirror phase response with constant gain

Initial simulations of the loop mirror will be presented using defined phase and gain functions in the matrix equations. Zero birefringence and polarisation rotation are assumed to simplify the analysis. Phase modulation will be considered first. In addition, as further simplifications, the fibre loop represents a simple delay in time only and the fibre absorption coefficient is assumed to be zero since only small lengths of fibre are used in an ASLALOM [Glesk et al 94]. The equations used for transmission need only take into account the *x* polarised field vector only. The following equations for phase modulation can then be written noting that $\phi_{\parallel} = 0$ and $\phi_x = \pi/2$ for ideal coupling and the CW and CCW field gains are both one:

$$T_1 = \alpha_{1,3}\alpha_{4,1}\exp(j(\phi_{CW} + \phi_X)) + \alpha_{1,4}\alpha_{3,1}.\exp\text{-}j(\phi_x + \phi_{CCW}) \tag{7.17}$$

$$T_2 = \alpha_{2,3}\alpha_{1,3}\exp(j(\phi_X + \phi_{CW} + \phi_X)) + \alpha_{2,4}\alpha_{3,1}\exp(j(\phi_{CCW}) \tag{7.18}$$

The variables in equations (7.12) and (7.13) are the CW and CCW phase shifts ϕ_{CW} and ϕ_{CCW} and it is assumed that these take on different values. Figure 7.4 then illustrates the simulated phase response using equations 7.17 and 7.18.

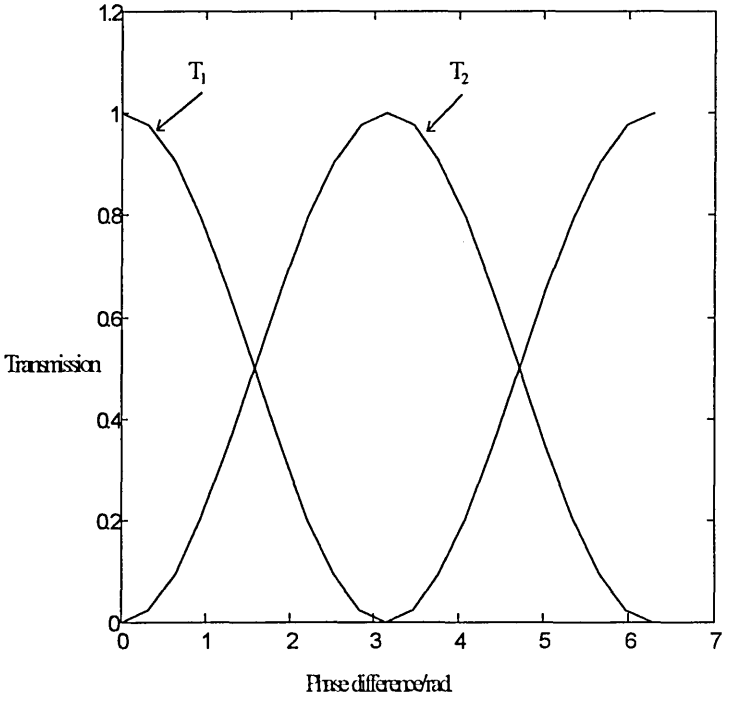

Figure 7.4 Transmission against phase. (gcw - gccw = 0).

It can be seen that the phase transmission of the ASLALOM is sinusoidal with maximum transmission occurring when the phase difference is an odd multiple of π. The system is therefore an interferomic device with an equivalent switching parameter $|\phi_{CW} - \phi_{CCW}|_{\pi} = \pi$. The variation in phase can be assumed to be due to a non-linear element in the ASLALOM. To verify this response, a comparison with experimental results by Eiselt [Eiselt et al 95] also shows oscillations in the transmission. This was accomplished using a TWSLA in the loop which is highly saturated such that the phase response $|\phi_{CW} - \phi_{CCW}|$ will pass through π.

7.4.2 Simulation of the loop mirror gain response with constant phase.

For gain modulation the following two equations apply:

$$T_1 = \alpha_{1,3}\alpha_{4,1}(G_{CW})^{1/2}\exp j\phi_x + (\alpha_{1,4}\alpha_{3,1}(G_{CCW})^{1/2}\exp j\phi_x \quad (7.19)$$

$$T_2 = \alpha_{2,3}\alpha_{1,3}(G_{CW})^{1/2}\exp j2\phi_x + \alpha_{2,4}\alpha_{3,1}(G_{CCW})^{1/2} \quad (7.20)$$

The simulated gain response (see figure 7.5) shows the loop output with a device which has a zero relative phase shift between the CW and CCW fields.

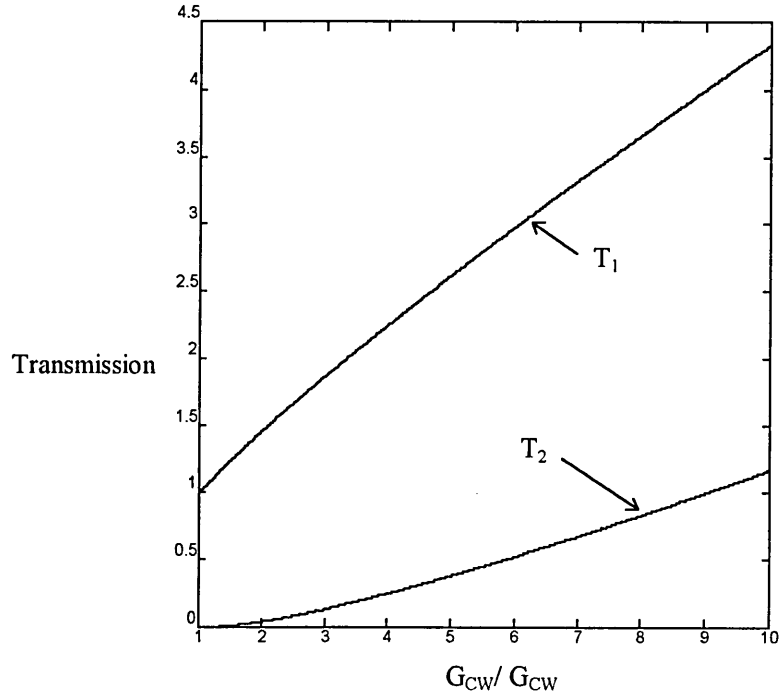

Figure 7.5 Transmission against gain ratio (ϕ_{cw} - ϕ_{ccw} = 0)

At a gain = 0 the loop is reflecting and all power output is from port 1. An output is obtained from both ports for all values of gain ratio above 1 and continues to rise with port 1 transmission always above port 2. It is not possible with this method to switch all the signal over from port 1 to port 2 and an output is always present at port 1. The two cases in 7.4.1 and 7.4.2 compare the difference when amplitude modulating and phase

modulating the fields. In practise the TWSLA will give gain and phase modulation simultaneously.

7.5 Loop Asymmetry

7.5.1 Large asymmetry loops

Refer to the ASLALOM architecture in section 5.3.4.4 and the TWSLA simulations in section 6.4.3. Large asymmetry loops are defined as having an asymmetry which is much greater than the TWSLA length, and the TWSLA is assumed to follow the point element model. The phase and gain responses of a CW data signal passing around the loop are simulated using equations 6.17, 6.18, 6.25 and 6.26. The CCW data is delayed by a time equal to the asymmetry t_{asy} (see figure 5.16). These values are then substituted for ϕ_{CW}, ϕ_{CCW}, G_{CW} and G_{CCW} in equation 7.16 using the values for m_{ij} given in table 7.1 which gives the power transmission vector of a data signal entering port 1. Effectively the transmission is simulating the output at port 2 of a continuous wave signal fed to port 1. Initially consider the case when the TWSLA is placed at a distance from the loop centre with an asymmetry comparable to the relaxation time (TWSLA parameters are as in table 6.1). This will be considered a large asymmetry loop. Consider first the case when the TWSLA has an asymmetry 1.5 times the recombination time by placing the TWSLA off the loop centre by a distance equal to $c_f \times \tau_2 \times 0.75 \approx 0.075$m which is 150 times the length of the TWSLA. The CW and CCW gain and phase temporal responses are shown in figures 7.6 and 7.7 respectively. The responses are separated in time by t_{asy} = 1 ns.

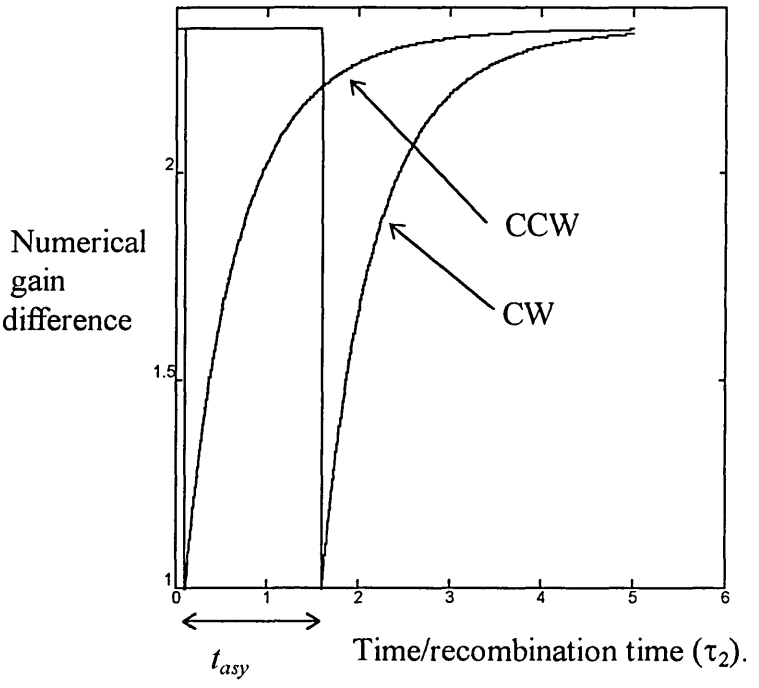

Figure 7.6
Simulated CW and CCW gain responses of large asymmetry loop

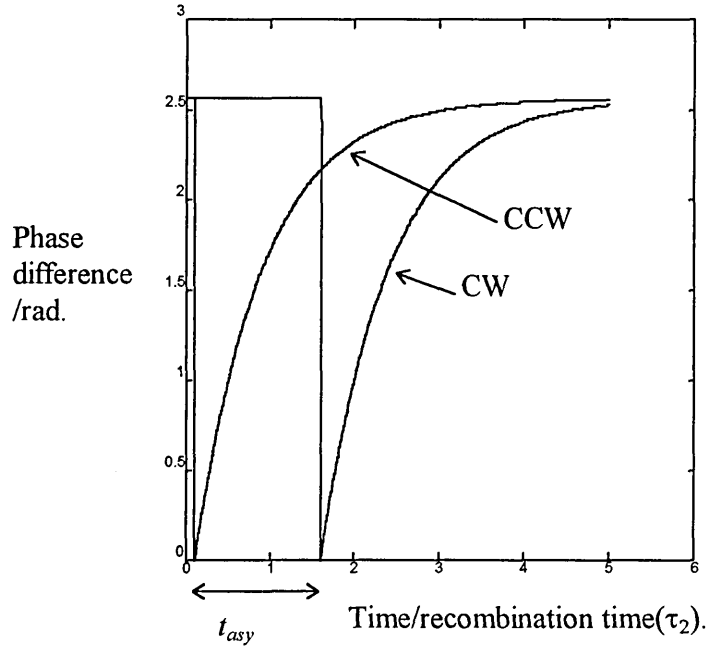

Figure 7.7
Simulated CW and CCW phase responses of large asymmetry loop.

The resulting power transmission using the gain and phase responses of figures 7.6 and 7.7 is shown in figure 7.8.

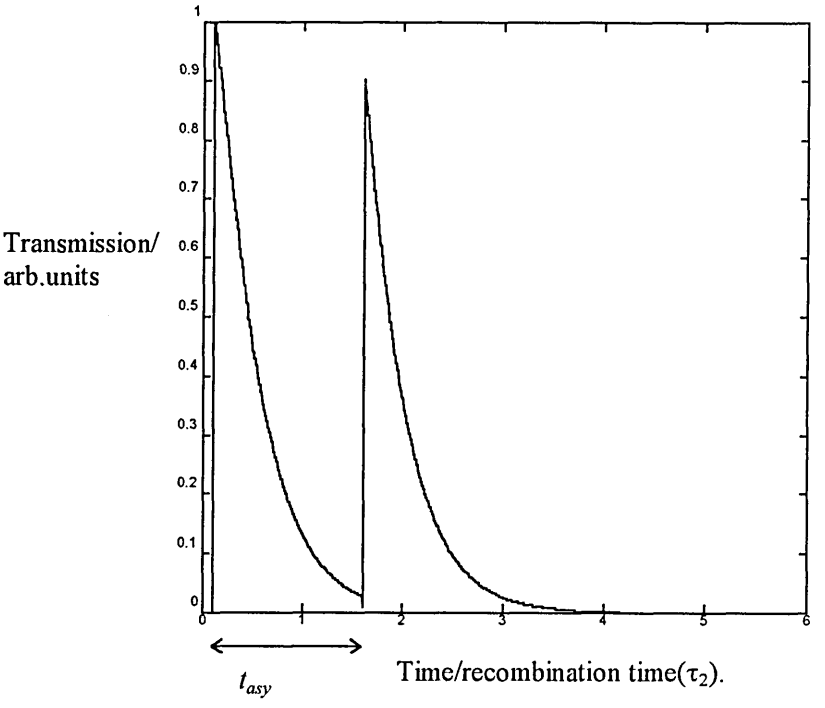

Figure 7.8 Simulated transmission response of large asymmetry loop.

From the waveform given in figure 5.16 one transmission window is expected to be opened with a width of t_{asy}. What is evident from figure 7.8 is that two windows have been opened separated by t_{asy}. With this configuration attempts to demultiplex a single OTDM pulse within the period t_{asy} could result in a second output immediately after the asymmetry time (the frame period is assumed > t_{asy}). Consider next the case where the TWSLA has an asymmetry equal to 0.75 times the recombination time. The resulting transmission is shown in figure 7.9. Two windows are apparent but note that the second window is reduced considerably in amplitude.

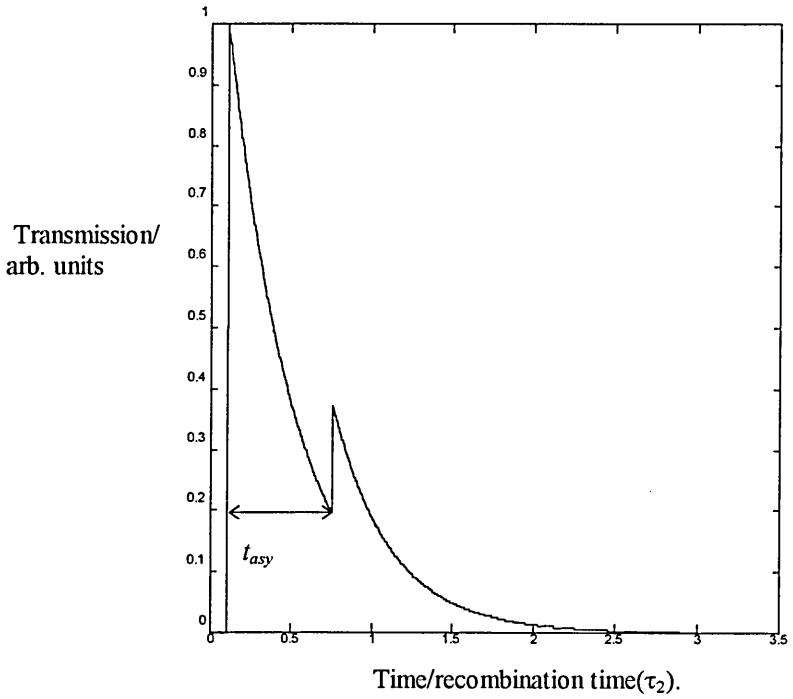

Figure 7.9 Simulated large asymmetry loop with reduced asymmetry.

Intuitively it is apparent that reducing the asymmetry will result in a reduction of the second window eventually leaving just one which will give a demultiplexing system which can select channels within a period equal to t_{asy}. Experimental results by Sokollof on an ASLALOM with t_{asy} = 690 ps and τ_2 = 600 ps show a second transmission window appearing at t = 690 ps which confirms the predictions of the large asymmetry simulation of figure 7.9. The configuration required to give one transmission window will be discussed next.

7.5.2 Medium asymmetry loops

The situation resulting from an TWSLA placed close to the loop centre such that one transmission window is evident will be called a medium asymmetry loop. The simulation presented in figure 7.10 is when the asymmetry is equal to 1/10 of the recombination time (equivalent to 20 device lengths).

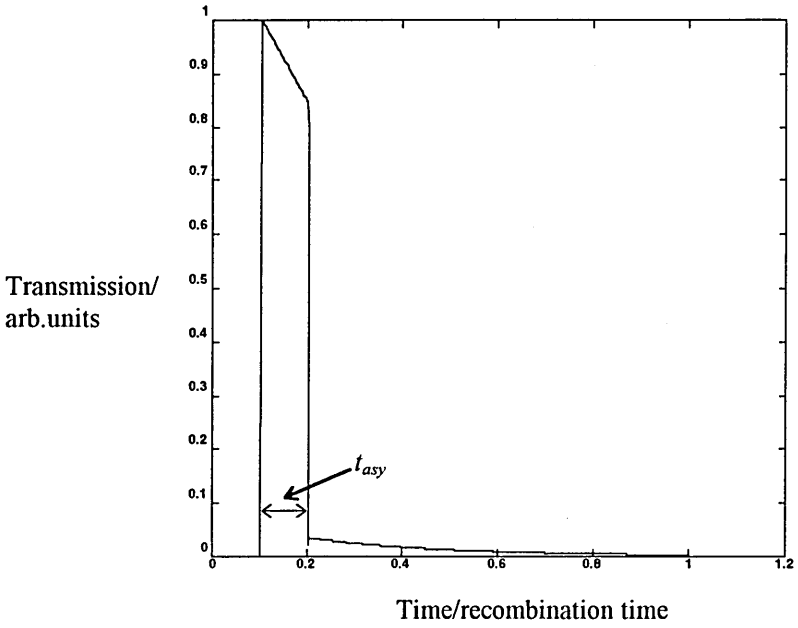

Figure 7.10 Transmission response of medium asymmetry loop.

The second transmission window has disappeared with a small trailing edge remaining ≈ 0.025 times the full transmission. Adjacent channel crosstalk would result from this trailing edge (≈ -16 dB). The transmission window has almost parallel sides with a width equal to 100 ps. Practical results of an ASLALOM by Sokollof [Sokolloff et al 93] also show a window with parallel sides when using an asymmetry of 130 ps (≈ 21 device lengths). If pulsed data input was used in this configuration it would be possible to demultiplex data at a rate of 10 Gbit/s. Theoretically the asymmetry could be reduced indefinitely and is effectively limited only by the rise time of the TWSLA non-linearity. Figure 7.11 shows the transmission response when the TWSLA is placed increasingly closer using the medium asymmetry analysis. The width of the transmission widow indicates the asymmetry.

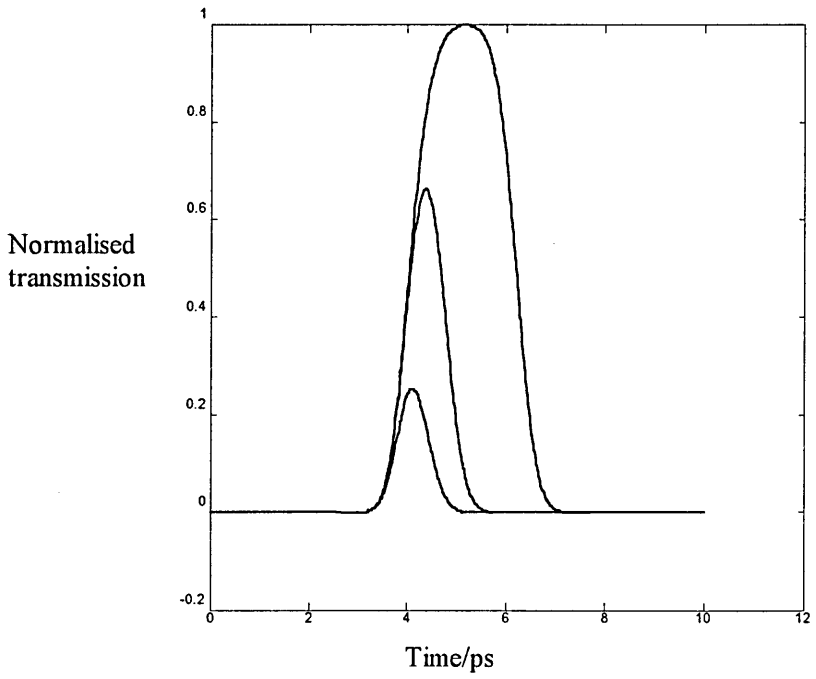

Figure 7.11 Transmission of small asymmetry using medium asymmetry method.

7.5.3. Small asymmetry loops

In the medium asymmetry case decreasing the offset from the loop centre resulted in a transmission window which will be limited by the non-linearity rise time. This would be the limiting case when two responses (gain or phase) are brought increasingly closer together. This is illustrated in figure 7.12.

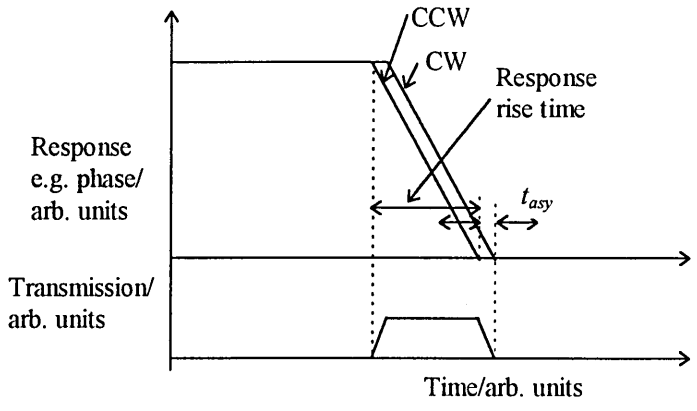

Figure 7.12 Transmission window for decreasing t_{asy}.

Using a 1 ps control pulse the window could be made as small as ≈ 1.5 ps (figure 6.5). The TWSLA was considered as a single point in sections 7.5.1 and 7.5.2. In reality it can be up 1 mm long for ASLALOM applications [Sokollof et al 94] giving a signal propagation time of ≈ 11 ps. With a device of such length it is difficult to specify the asymmetry when windows of the order of the propagation time are considered. This section will examine what effect the length of the TWSLA has on loop operation. Section 6.4.4 demonstrated a method of modelling the TWSLA which includes time and space information on the carrier density when subjected to a pulse input. The function for calculating the gain and phase modulation is calculated by integrating over the carrier density function $n(z,t)$. Consider a case initially where the carrier density has reached a steady state value and n is a function of length only i.e. $n = n(z)$. A parameter can be defined which will be called the carrier density length product and is calculated from the following integral which describes a wavefront travelling along the amplifier:

$$n'_{CW(CCW)} = \int_0^L n(z)dz \qquad (7.21)$$

The above integral assumes that $n(z)$ is constant for the time period $t - L/c_{Nf}$ to t where $t - L/c_{Nf}$ marks the beginning of the input signal and c_{Nf} is the speed of propagation in the TWSLA. However, during the control pulse input, the carrier density is a function of time and the carrier density can be written as $n(z,t)$. The time is assumed to span the interval $-\infty$ to $+\infty$ with the control pulse applied between the time intervals t_1 to $t + L/c_{Nf} + t_p$ where t_p is the width of the control pulse. Before t_1 the carrier density is assumed to be the value given by the data signal intensity and to have reached steady state conditions. It is calculated using the method outlined in section 6.2.3. After $t +$

$L/c_{Nf} + t_p$ when the pulse has propagated through the TWSLA, the carrier density is assumed to have the saturated value for a time period associated with small asymmetry demutiplexing (a few ps). As the carrier density is now a function of time the carrier density length product moves along the time axis by a period equal to dz/c_{Nf} for each movement along the length axis of figure 6.9. The integral in equation 7.21 now needs to move along the time axis with the speed of propagation of the wavefront. A new function is now defined, $n(z,t-\frac{L}{c_{Nf}}+\frac{z}{c_{Nf}})$, where it is understood that every occurrence of t in the function $n(z,t)$ is replaced by $t - L/c_{Nf} + z/c_{Nf}$ when performing the integral to calculate the carrier density length product. This means the CW data experiences a carrier density length product described by:

$$n'_{CW}(t) = \int_0^L n(z, t - \frac{L}{c_{Nf}} + \frac{z}{c_{Nf}})dz \qquad (7.22)$$

(Note the term L/c_{Nf} ensures the time t in equation 7.22 corresponds with a wavefront reaching the end of the TWSLA). The corresponding CCW integral moves as the same speed as the CW integral of equation 7.22 but in the opposite direction, resulting in a sign change in the moving co-ordinate i.e.:

$$n'_{CCW}(t) = \int_0^L n(z, t - \frac{z}{c_{Nf}})dz \qquad (7.23)$$

The carrier density length product is now a useful parameter in calculating the phase and gain of a wavefront which has passed through the TWSLA at a time t. c_{Nf} is essentially a function of carrier density and can be written as:

$$c_{Nf} = \frac{c}{N - \frac{dN}{dn}(n - n_1)} \qquad (7.24)$$

If the change in index is assumed to have a negligible effect on the speed of the wave then c_{Nf} can be considered constant throughout the length of the TWSLA (which amounts to a propagation time 5 orders of magnitude different for a π phase change). The CW and CCW wavefronts experience different TWSLA properties determined by the asymmetry present in the loop. Consider figure 7.13 which depicts the asymmetry present in an ASLALOM architecture with the length of the TWSLA included showing the z direction for the CW and CCW integrals.

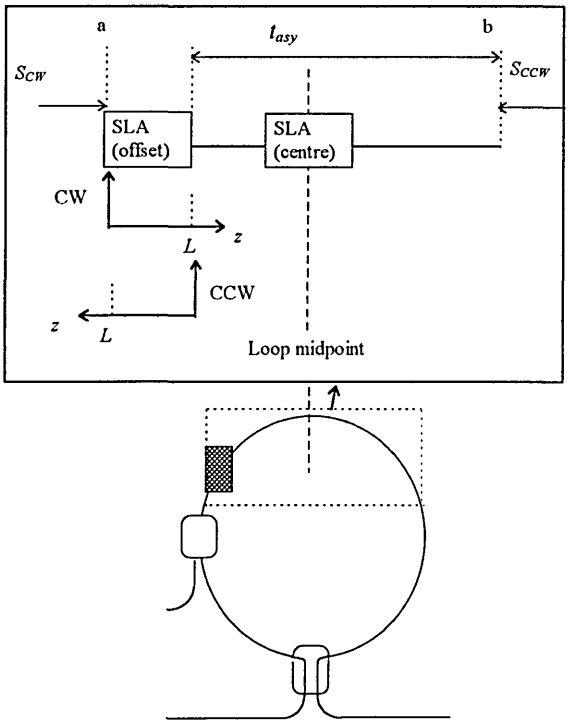

Figure 7.13 CW and CCW co-ordinate system.

The CW and CCW wavefronts are represented by the arrows shown (S_{CW} and S_{CCW}), and with identical fibre lengths in the loop the two signals arrive at the points indicated at the same time. With the TWSLA centrally positioned equations 7.22 and 7.23 apply directly. When the TWSLA is positioned off centre the CW signal experiences the TWSLA

properties at a time say t_f calculated using equation 7.22. The CCW signal reaches the TWSLA at a time later given as $t_f + t_{asy}$ as indicated in figure 7.13 and, therefore, the CCW carrier density product function is now advanced by t_{asy} which may be written as:

$$n'_{CCW}(t) = \int_0^L n(z, t - \frac{z}{c_{Nf}} + t_{asy})dz \tag{7.25}$$

For simulation purposes the integrals in equations 7.22 and 7.25 are written in discrete form. To simplify the analysis the discrete length interval is related to the time interval Δt by:

$$\Delta l = \frac{\Delta t}{c_{Nf}} \tag{7.26}$$

The phase modulation at discrete time k for the CW signal is then:

$$\phi_{CW}(k) = \frac{2\pi\Delta L\Gamma}{\lambda}\frac{dN}{dn}\sum_{l=0}^{l=L_m} n(l, k - L_m + l) \tag{7.27}$$

where $L_m = L/\Delta L$. The corresponding gain modulation is:

$$g_{CW}(k) = \prod_{l=0}^{l=L_m} \exp\Gamma a(n(l, k - L_m + l) - n_0) \times \Delta L \tag{7.28}$$

or equivalently:

$$g_{CW}(k) = \exp\sum_{l=0}^{l=L_m} \Gamma a(n(l, k - L_m + l) - n_0) \times \Delta L \tag{7.29}$$

and for the CCW modulation:

$$\phi_{CCW}(k) = \frac{2\pi\Delta L\Gamma}{\lambda}\frac{dN}{dn}\sum_{l=0}^{l=L_m} n(l, k - l + k_{asy}) \tag{7.30}$$

$$g_{CcW}(k) = \prod_{l=0}^{l=L_m} \exp\Gamma a(n(l, k - l + k_{asy}) - n_0) \times \Delta L \tag{7.31}$$

$$g_{CCW}(k) = \exp\sum_{l=0}^{l=L_m} \Gamma a(n(l, k - l + k_{asy}) - n_0) \times \Delta L \tag{7.32}$$

where $k_{asy} = t_{asy}/\Delta t$ is the discrete asymmetry.

7.5.3.1 Simulations with finite length effect of TWSLA

To demonstrate the finite length of the ASLALOM the phase and gain responses are calculated using equations 7.27, 7.29 ,7.30 and 7.32 with the carrier density matrix of equation 6.27 calculated with a 800 fJ 1 ps FWHM control pulse input which propagates in the CW direction as in figure 7.13. A background data pulse train of 10 fJ 1 ps FWHM at 250 GHz is assumed giving an average power input from equation 6.1. This sets the carrier density initial conditions prior to control input. The TWSLA is positioned at the exact centre of the loop (k_{asy} = 0). The simulated phase and gain

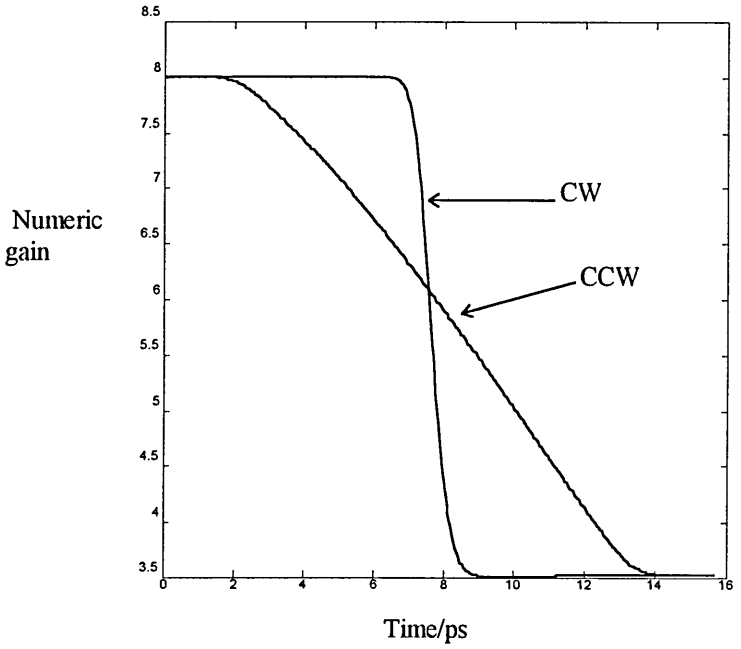

Figure 7.14 Gain response of centrally placed TWSLA.

responses are shown in figures 7.14 and 7.15.

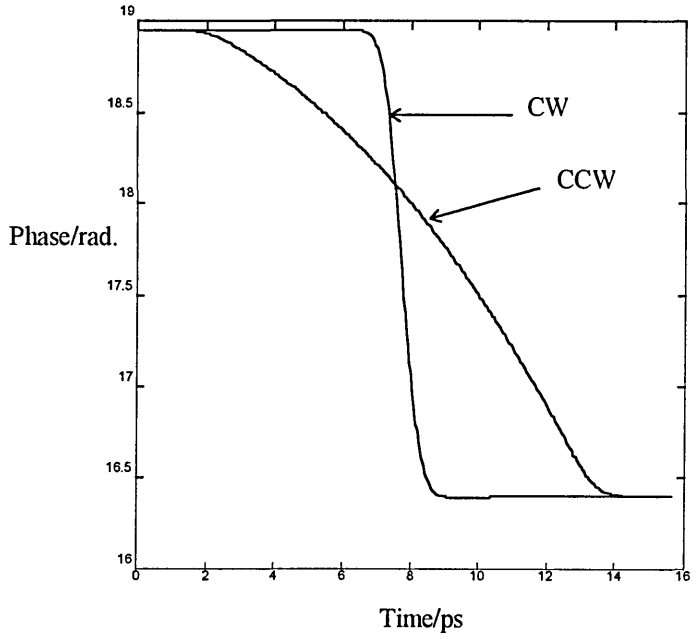

Figure 7.15 Phase response of centrally placed TWSLA.

The device length used in this simulation is 500μm and the TWSLA refractive index is chosen as ≈3.5 [Sokoloff 94] which is typical of InGaAsP devices. The plots show the different TWSLA properties experienced by a CW and CCW signal. The CW response has a fast response time similar to the medium and large asymmetry loops. The CCW response has a sloping response which spans a time interval of ≈ 10 ps, both responses have the same pre and post control values. The gain and phases response have identical shapes due to summations being equal in equations 7.27, 7.29 7.30 and 7.32. Figure 7.16 shows the resulting transmission calculated using equation 7.16.

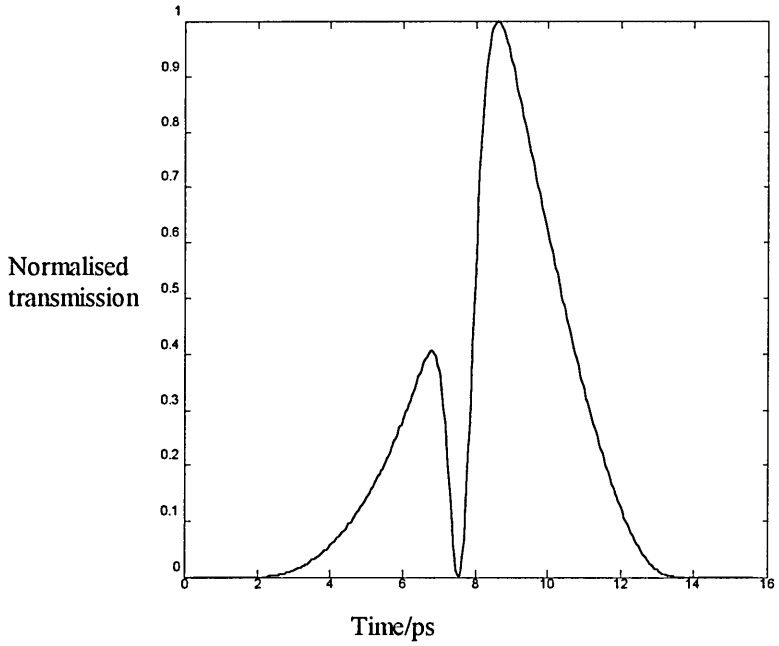

Figure 7.16 Transmission of centrally placed TWSLA.

The transmission plot has generated two pulse shapes due to the finite rise time of the CW response resulting in the central dip in the response. A single pulse shape is only achievable with a TWSLA which has zero non-linearity rise time. The transmission rise and fall times are related to the relative position of the CW to CCW response. The amplitude in figure 7.16 is normalised to a peak value of ≈ 2. An asymmetry can be introduced into the loop. Figure 7.17 shows the phase response with an asymmetry of 6 ps introduced which effectively shifts the CW response along the time axis (the asymmetry is introduced as in figure 7.13). The gain response (not shown) would have a similar shape and shift in time as the phase response .

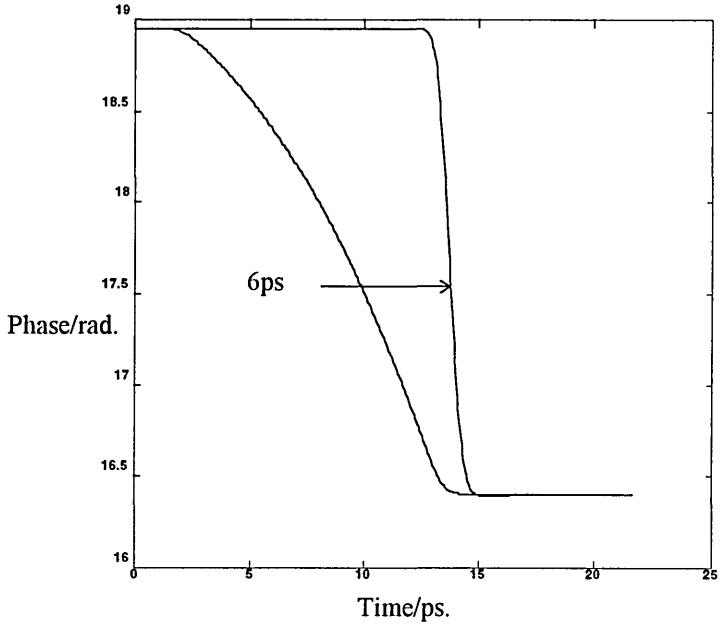

Figure 7.17 Phase response with 6 ps asymmetry.

The transmission response with this asymmetry is shown in figure 7.18.

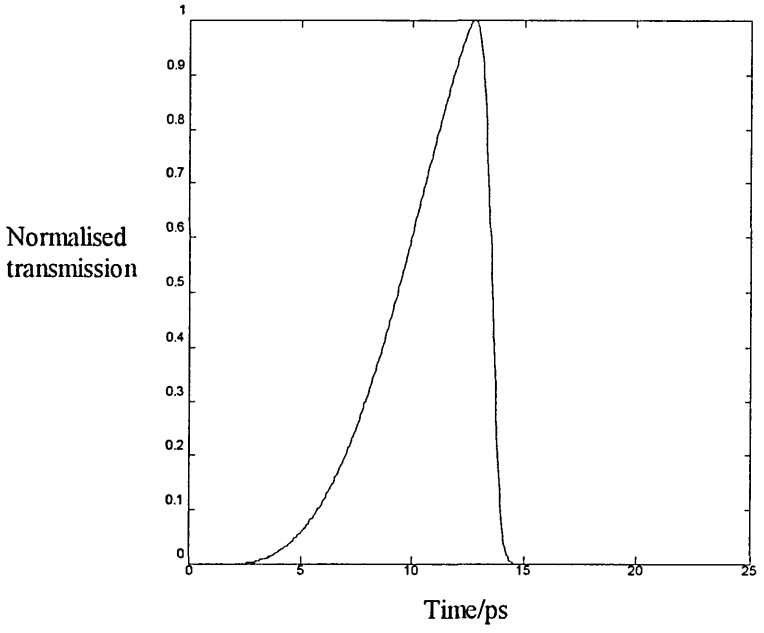

Figure 7.18 Transmission response with a 6 ps asymmetry.

The rising edge of the window is approximately 12 ps and the trailing edge is the TWSLA non-linearity rise time (the amplitude transmission is normalised to a peak value ≈ 4.5). Observations when using the finite length effect in the ASLALOM show significant departure from the expected transmission windows in figure 5.16. The long trailing edge of the CCW is now placing a fundamental limit on the width of the switching window.

7.5.3.2 CCW modulation time

The CCW long response time can be explained by considering the limits between the carrier density change of a signal propagating against the control pulse (see figure 7.19).

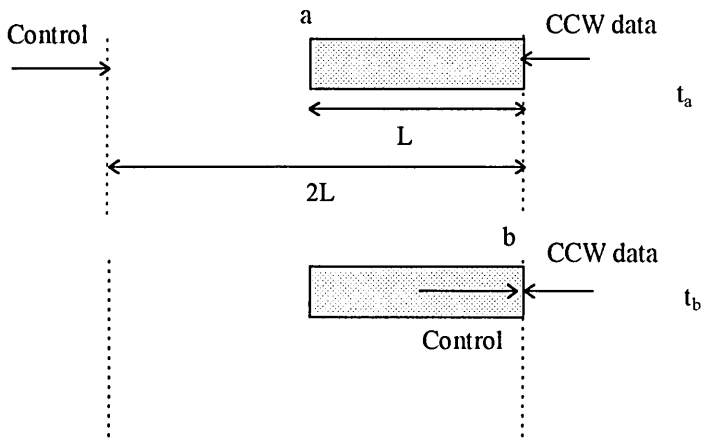

Figure 7.19 CCW response time.

t_a represents the first occurrence of the CCW pulse experiencing the effect of the control pulse and this is when both pulses will meet at point *a*, t_b is when both meet at point *b*. The total response time is:

$$t_b - t_a = 2L/c \tag{7.33}$$

which is twice the device propagation time. In effect when the CCW wavefront is advanced in time by an amount δt the addition to the modulation is $\delta z/2c_N$, i.e. the CCW

pulse moves at a speed $2c_N$ relative to the control pulse. With a step change in carrier density from n_u to n_{sat} the carrier density length product can be written simply as:

$$n' = \left[\left(1 - \frac{tc_N}{L2}\right)n_u + \frac{tc_N n_{sat}}{L2}\right]H(t-a) \tag{7.34}$$

where $H(t - a)$ is unit step function at t_a figure 7.19. Simulated values for n′ are given in figure 7.20 for propagation times equal to L/c_N where $n_{sat} = 0.1\ n_u$.

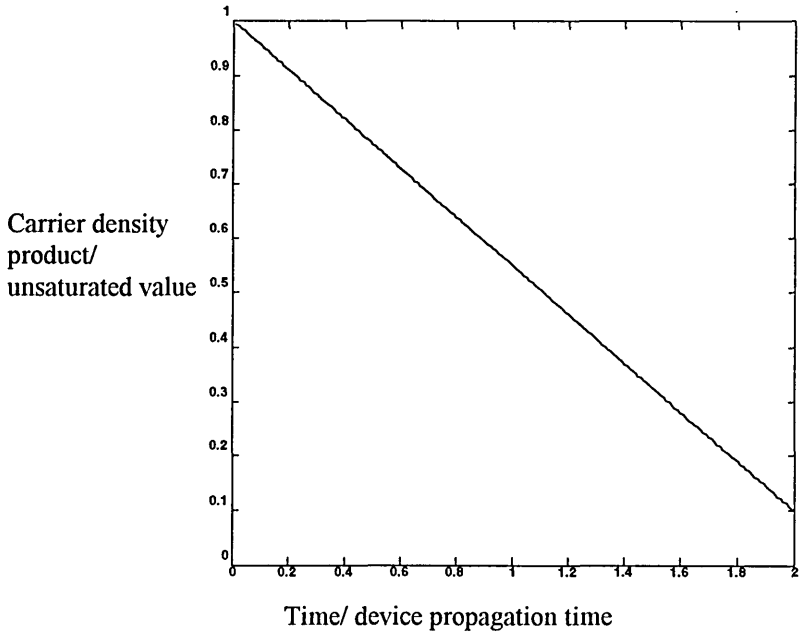

Figure 7.20 CCW modulation in relation to TWSLA propagation time.

Initial investigations and the previous explanation show the CCW response time equal to twice the propagation time. Simulations for varying TWSLA lengths are now shown in figure 7.21.

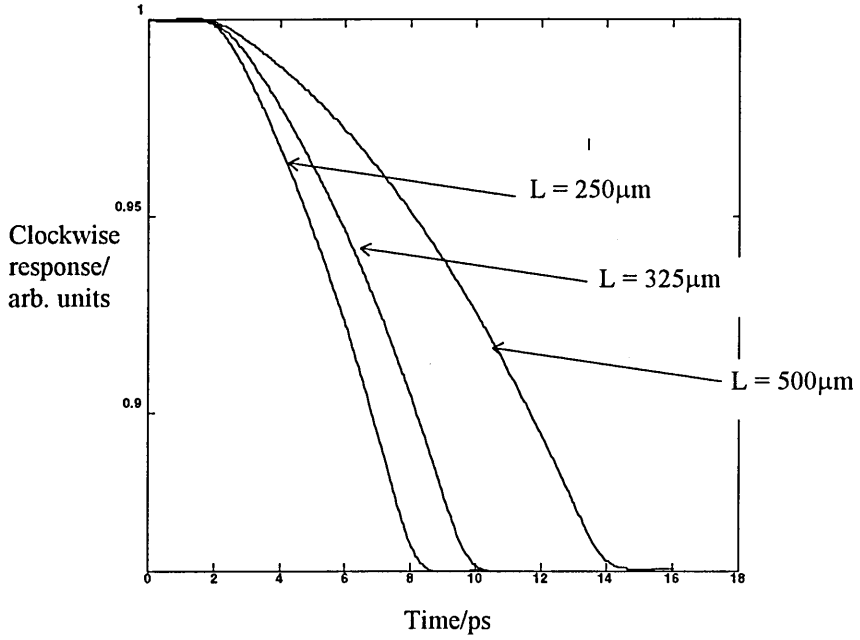

Figure 7.21 CCW response for different TWSLA lengths.

Three different device lengths are simulated in figure 7.21 where the CCW response fall times show respective values of 6.2 ps, 8 ps and 12 ps for TWSLA lengths of 250, 325 and 500 μm. The calculated values for the times from equation 7.33 are $2\times250\times10^{-6}\times3.5/3\times10^{8} = 5.83$ ps, $2\times350\times10^{-6}\times3.5/3\times10^{8} = 8.17$ ps and $2\times500\times10^{-6}\times3.5/3\times10^{8} = 11.67$ ps showing that the CCW response times are in accordance with equation 7.34. With an asymmetry included the width of the transmission window will be equal to $L/c_{NF} + t_{asy}$ if it is assumed the cross over of the CW and CCW gain and phase responses occur halfway along the CCW slope (see figures 7.14 and 7.15).

7.5.3.3 Window amplitude

The temporal response of the ASLALOM has been discussed and the amplitude of the transmission with varying asymmetry will be considered next. The results shown in

figures 7.16 and 7.18 indicate that a smaller transmission amplitude window occurs with a smaller asymmetry. Figure 7.22 shows the window amplitude against asymmetry.

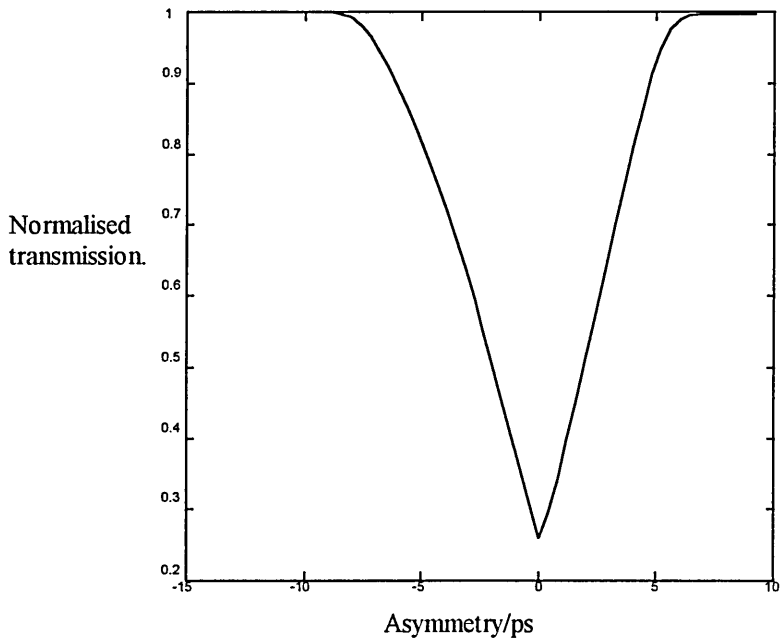

Figure 7.22 Amplitude response with varying asymmetry.

In figure 7.22 a negative value occurs if the TWSLA is placed on the left hand side of the loop in figure 7.13 and a positive value for the right hand side. The amplitude reaches a maximum value with increasing asymmetry in either direction. The minimum amplitude occurs when the asymmetry is zero and the fall and rise time are equal. This shows that the transmission window amplitude and width are both functions of asymmetry. Theoretical results of an ASLALOM in Kane [Kane 94] also show this amplitude/ asymmetry characteristic

7.5.3.4. Comparison between simulated and practical results

A comparison of the simulations with previous reported results will now be made to check the validity of the model. The simulations will be compared with previous reported results on an ASLALOM [Kane et al 94] who used the ASLALOM with an TWSLA

positioned 4 ps and 65 ps from the centre. The loop transmission for both these asymmetries will be analysed. Figure 7.23 shows the results of a simulation with a 500 μm long TWSLA placed 4 ps from the loop centre.

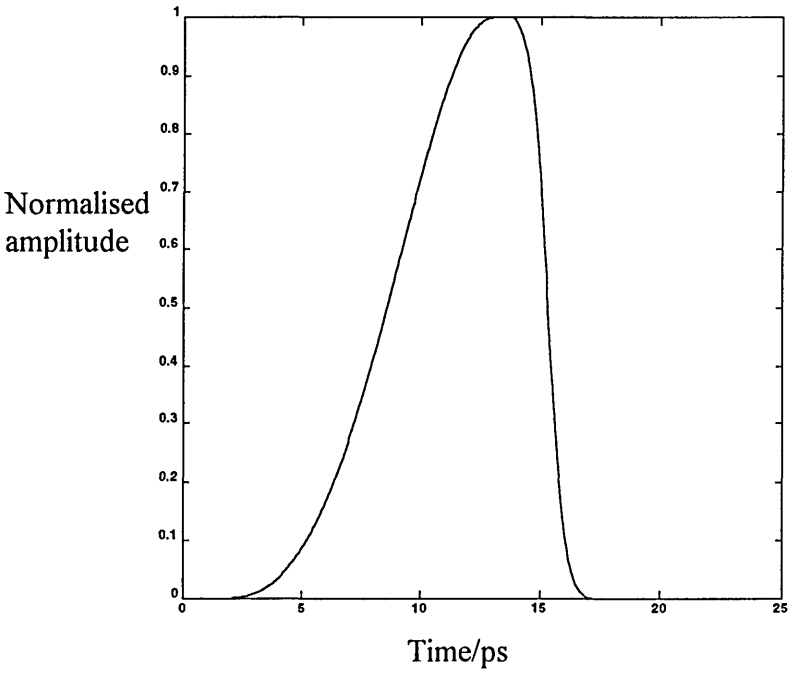

Figure 7.23 TWSLA placed 4 ps from loop centre.

The experimental and simulated comparisons are given in table 7.2.

Parameter	Experimental *	Simulated	% difference
Pulse width /ps	15	14	7
FWHM /ps	9	8	11
Rising edge /ps	≈11	11.5	4.5
Trailing edge /ps	4	3.5	12.5

Table 7.2.
A comparison of practical and simulated results for the ASLALOM.
* Kane 94

Table 7.2 indicates close agreement between simulated and experimental results. Practical measurements show the finite length effect as the rise time corresponding to 11

ps which theoretically equals $2\times500\times10^{-6}\times3.5/3\times10^{8} \approx 11.7$ ps for the finite length effect discussed in section 7.5.3.2. The width of the transmission window is expected to be approximately 8 + 11.5/2 = 14 ps which is given by the simulation. Figure 7.24 is a simulation with a medium asymmetry ASLALOM. The TWSLA is placed 65 ps from the loop centre and the pulse widths are 140 ps and 150 ps simulated and experimental [Sokolloff et al 93] respectively showing agreement to within 7%.

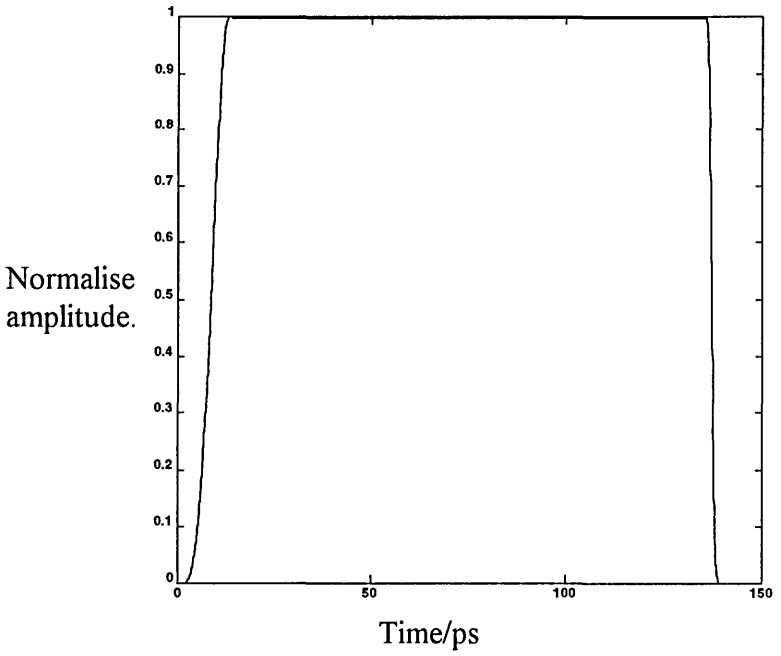

Figure 7.24 TWSLA placed 65 ps from loop centre.

7.5.3.5 Data pulse input.

Simulations will now be presented with a data pulse input to the ASLALOM.. Initially a simulation will be presented in accordance with experiments by Eiselt [Eiselt et al 93] who used 9 Gbit/s data stream consisting of 20 ps FWHM a control pulse of 35 ps and an asymmetry of 130 ps. Figure 7.25 shows the simulated response.

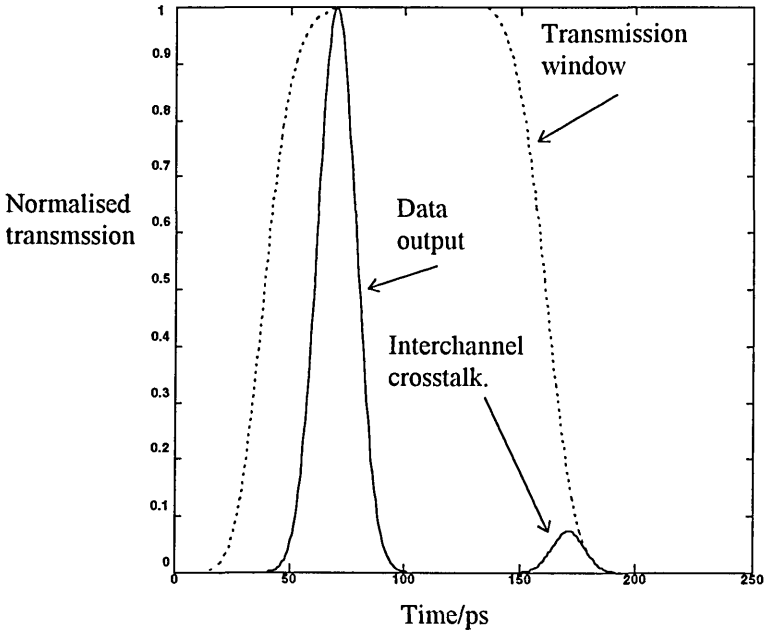

Figure 7.25 Simulation of 9 Gbit/s data demultiplexing.

The simulation of figure 7.25 is in agreement with the results of [Eiselt et al 93] and shows complete demultiplexing of a single pulse. The simulations show a second smaller pulse due to interchannel crosstalk which is also present in the practical plots. Further simulations demonstrating demultiplexing of 250 Gbit/s are shown in figures 7.26 and 7.27. Here the pulse width is 1 ps and the loop asymmetry is 5 ps. This arrangement has been demonstrated experimentally by Glesk [Glesk et al 94].

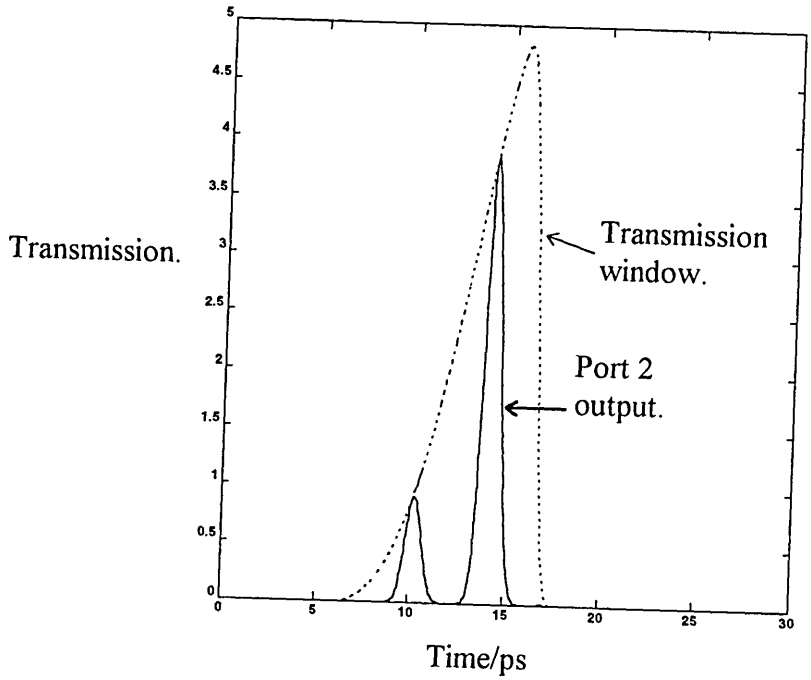

Figure 7.26 Port 2 output of 250 GBit/s data stream

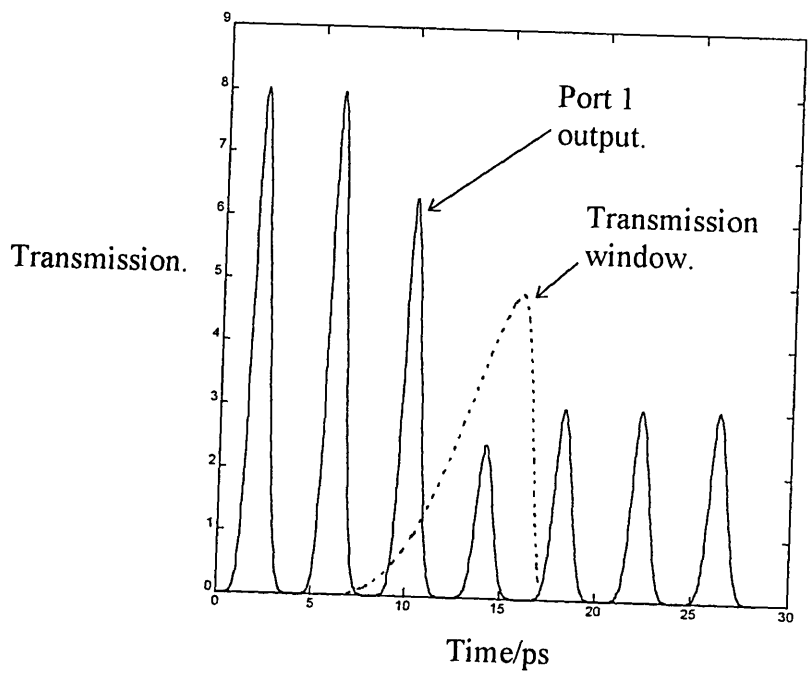

Figure 7.27 Port 1 output of 250 GBit/s data stream.

In this configuration a window of ≈ 11 ps with a FWHM of ≈ 5.5 ps is produced. The window cannot be decreased any more as it equals the finite length limit of $2L/c_{NF}$. Pulses with the parameters indicated are shown to introduce interchannel crosstalk at ≈ -5.74 dB with a pulse gain of 4 as indicated in figure 7.26. The optimum value for crosstalk is indicated in figure 7.28 by varying the data pulse position in relation to the transmission window.

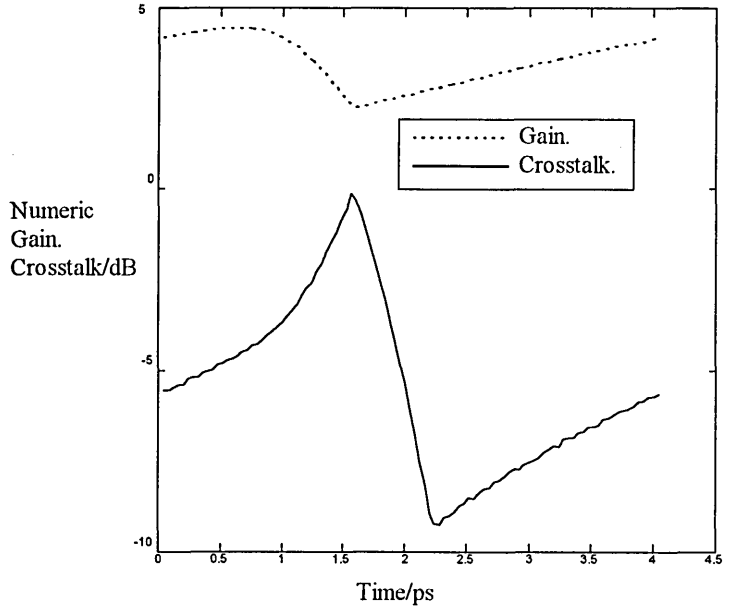

Figure 7.28 Gain and crosstalk v. pulse position.

.From figure 7.28 it is apparent that an optimum position can be achieved regarding crosstalk. The optimum crosstalk however does not coincide with the maximum gain. Table 7.3 indicates that any further reduction in crosstalk is at the expense of bit separation.

Bit rate Gbit/s	Crosstalk/dB	Gain.
1000	-0.81	4.60
500	-2.21	4.09
333	-4.6	3.79
250	-8.85	3.15
200	-16.33	2.72
168	-18.38	1.23

Table 7.3. Interchannel Cross talk for different bit rates.

Figure 7.27 shows that the output from port 1 allows a certain amount of signal to be let through during the transmission window. Although this is unimportant as regards the demultiplexed data it may be disadvantageous if a drop and insert function was required [Ellis et al 94]. Figure 7.29 shows the port 1 and 2 transmissions with an increased control pulse energy.

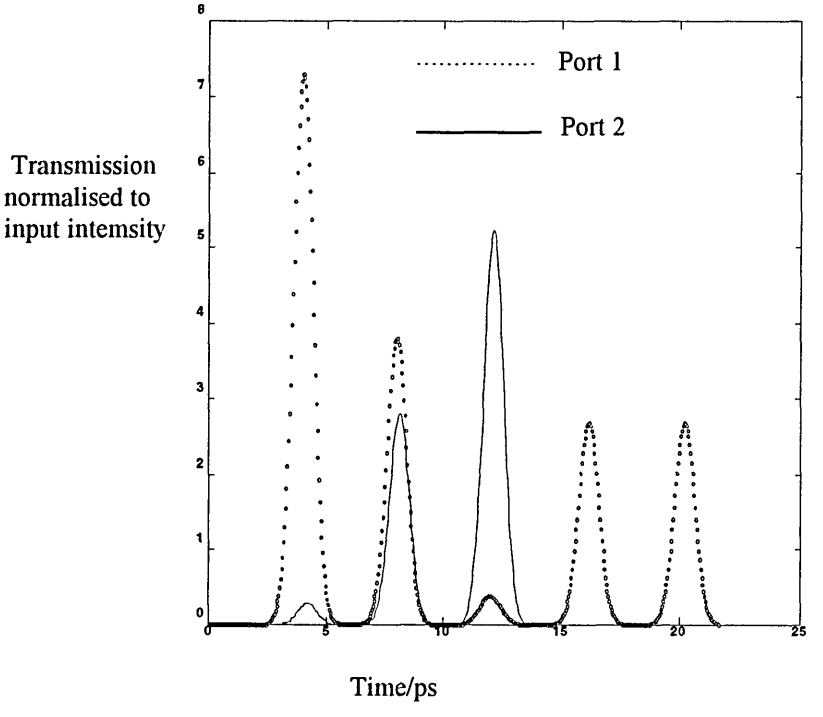

Figure 7.29 Port 1 and port 2 output optimised for add drop function.

Table 7.4. further illustrates the improvement in port 1 interchannel crosstalk with an increase in control pulse energy and consequently phase.

Pulse energy/fJ	Phase difference/rad	Crosstalk/ dB
600	1.7	-0.8978.
800	2.0	-2.1722.
1000	2.3	-3.5782.
1150	2.5	-4.9383.
1600	3	-7.9339.

Table 7.4. Port 1 interchannel crosstalk.

7.5.4 High frequency control input

When a signal is fed to the loop which has a period which is short compared to the recombination time, then the carrier density will settle to a value which is determined by the average power of the signal as in section 6.1. With control pulse separation times > τ full recovery of the device is allowed and the carrier density settles back to its pre-control input value as in the preceding sections. With a small separation time the carrier density will achieve an average approximated from the steady state rate equation 6.3 corresponding to n_i. Equation 6.5 results in a smaller Δn and when substituted in equation 6.25 the ASLALOM gives a lower transmitted intensity (equation 7.18). To overcome this the ASLALOM is operated with higher currents which increases Δn due to the increase in n_i in equation 6.5. Figure 7.30 shows the simulated effect of increasing current on the transmitted intensity for a 100 GHz control signal.

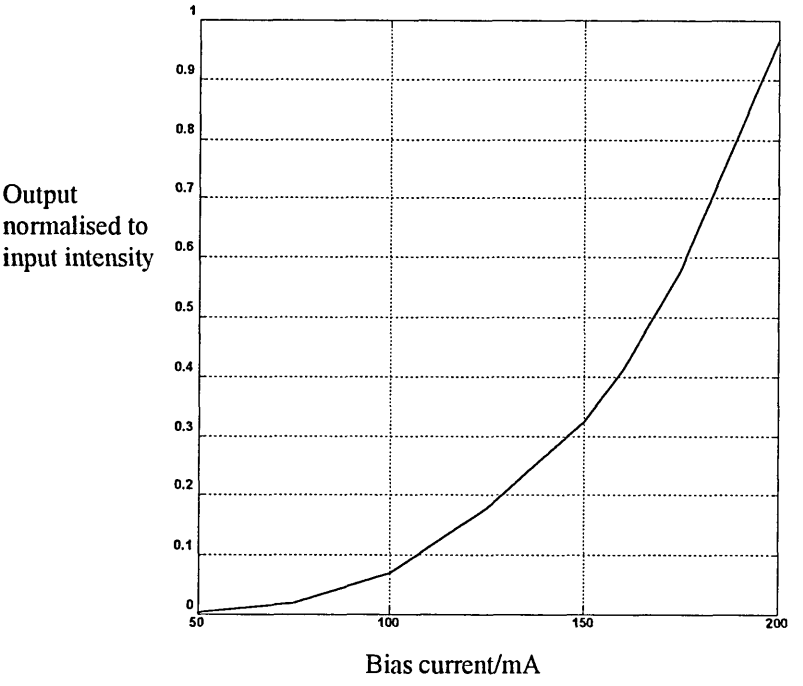

Figure 7.30 Relative output of loop with increasing bias current.

The concept of high bias currents for high data rate inputs is evident in the experiments of [Ellis et al 95] who used a current of 200 mA for a 5 GHz control signal compared to the considerably lower current used by Sokollof [Sokollof et al 94] (35 mA) for a control pulse frequency of 100 MHz.

7.5.4.1 Response of ASLALOM with 100 GHz control signal

At 100 GHz the control pulse period is 10 ps which is 1/100 of a recombination time of 1 ns. By inputting a continuous pulse stream of this form to the ASLALOM the resulting phase and gain responses can be observed for both the CW and CCW propagating signal. Consider figures 7.31 and 7.32 which show the gain and phase response of the ASLALOM for a CW data signal with a 100 fJ 1 ps control pulse, a bias current of 200 mA and with the TWSLA positioned at the loop centre. It can be seen that the phase difference exhibits a variation of ≈ 0.35 radians and a gain variation of ≈ 0.7 which will

result in a lower transmission compared to previous loop operation which had gain and phase differences an order of magnitude greater.

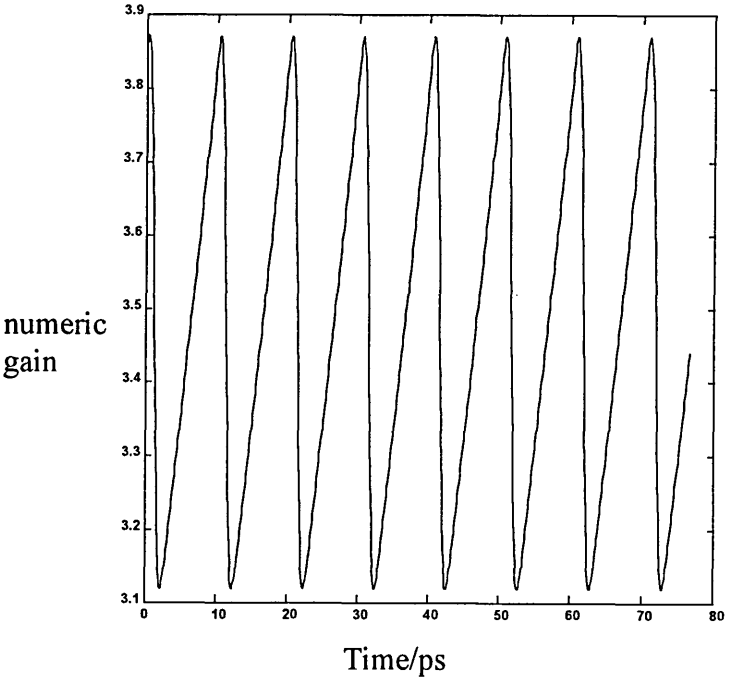

Figure 7.31 CW gain response of 100 GHz control signal.

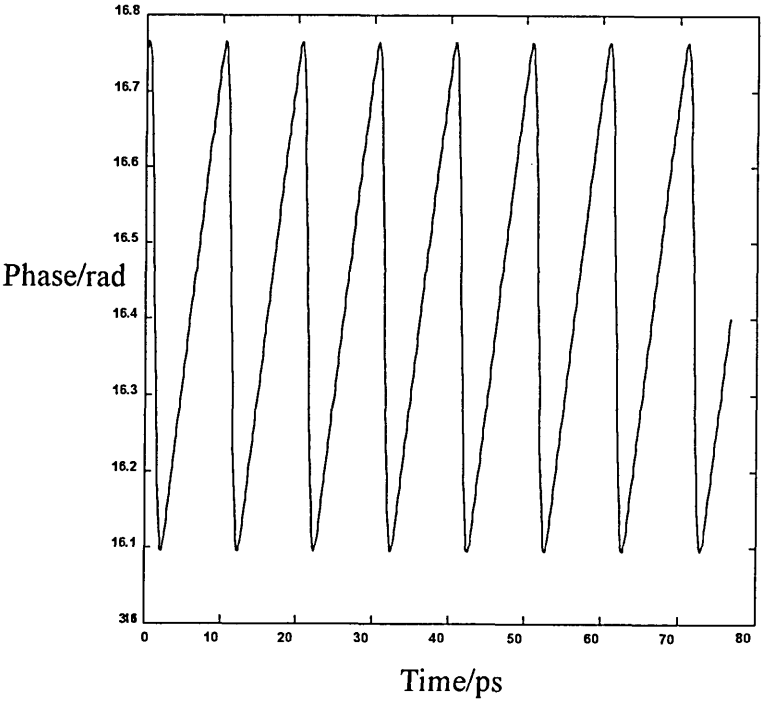

Figure 7.32 CW phase response of 100 GHz control signal.

The responses of figure 7.31 and 7.32 give the characteristic sawtooth wave form as demonstrated theoretically in [Ellis et al 95] which shows a similar shape for the phase response of an ASLALOM when a 10 GHz control signal is input with a value of 500 ps for τ_2.

7.5.4.2 CCW data response and the finite length effect

The spacing between pulses in this example is 10 ps and as discussed previously the finite length is effective around the propagation time of the TWSLA ($\approx$ 5 ps for a 500 μm device). To avoid patterning (section 7.5.6) the TWSLA needs to be placed at a distance of 500 μm from the loop centre which is considered to be a small asymmetry. The CCW responses need to be calculated according to equation 7.25 as in the low frequency control case. A further point to consider is the recombination of the carriers for high control frequencies. As previously discussed the recombination rate is effectively determined by the control frequency which gives a recombination time around 10 ps. Previous analysis considered that a pulse (CW or CCW) passed through the TWSLA with negligible recombination of the carriers. Figure 7.33 helps to explain the concept.

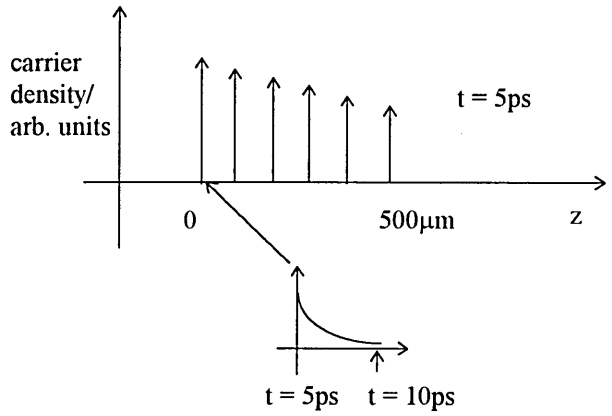

Figure 7.33 Recombination of carriers with 100 GHz control.

Consider a control pulse incident on the TWSLA with a delta function for the control. The delta function is assumed to produce an instantaneous local depletion of the carriers [Manning 94]. The carrier density will decay on a 10 ps time scale before the arrival of the next control pulse (cf. figure 7.31). A CCW data pulse will have an TWSLA device propagation time of $T_L \approx 5$ ps and over this period the carrier density will have decayed considerably (≈ 0.5 if the decay is considered linear). This effect is demonstrated in Figures 7.34 and 7.35 which show the gain and phase response of CCW data signals.

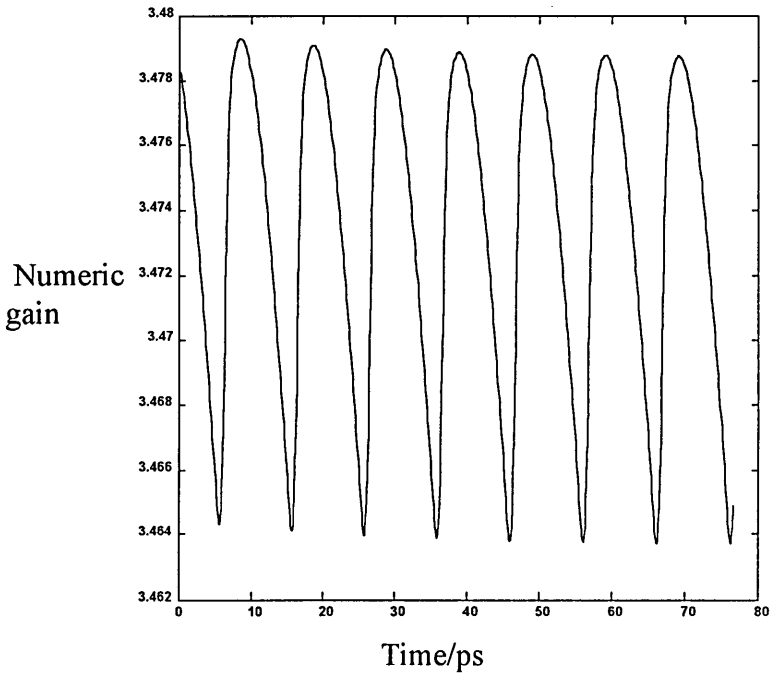

Figure 7.34 CCW gain response of 100 GHz control signal

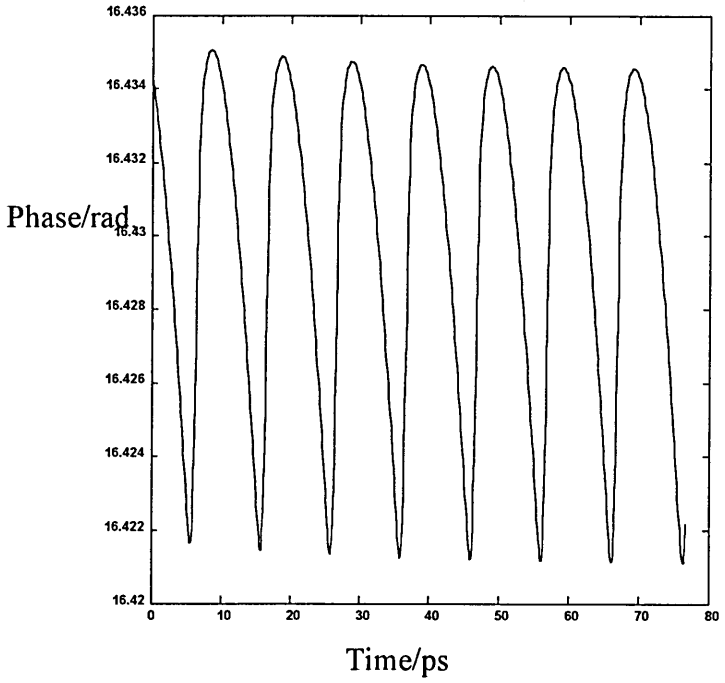

Figure 7.35 CCW phase response of 100 GHz control signal

As expected the CCW gain and phase responses do not reach the CW modulated value as in the low frequency case as in sections 7.5.1. to 7.5.3 The phase and gain variation is now only 0.12 rads and 0.015 respectively. Now consider the loop transmission as in figure 7.36. The output is still evident even with this low value of CCW modulation with a normalised output of 0.1.

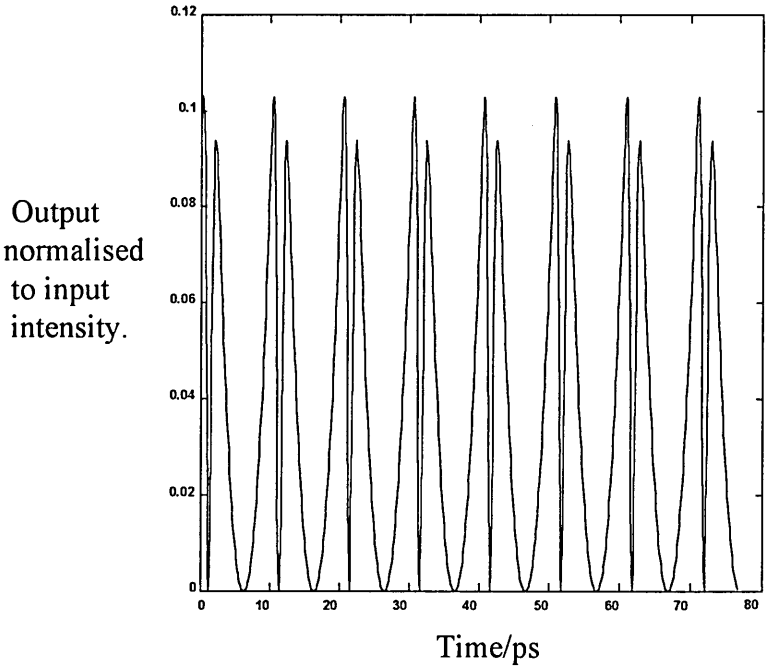

Figure 7.36 Port 2 output with 100 GHz control signal.

Here the pulse width is equal to the bit period (10 ps). To explain the pulse width dependence on the control frequency period consider figure 7.37 where it can be clearly seen that the CCW response is almost flat compared with the CW response.

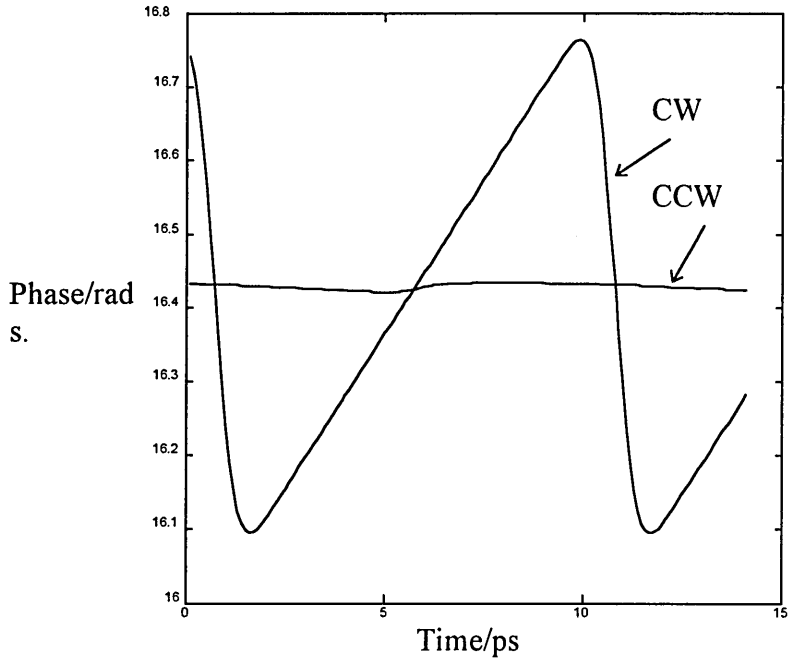

Figure 7.37 CW and CCW data phase response with 100 GHz control signal.

The CW response will tend to dominate the output and the pulse width is determined by this.

A control pulse frequency of 40 GHz is now investigated (i.e. a time of 25 ps between pulses ($5 \times T_L$)) with a bias current is 100 mA. Assuming a linear carrier density relaxation between control pulses the decay is now only 20% during T_L. The effect of this on the phase response can be seen in figure 7.38.

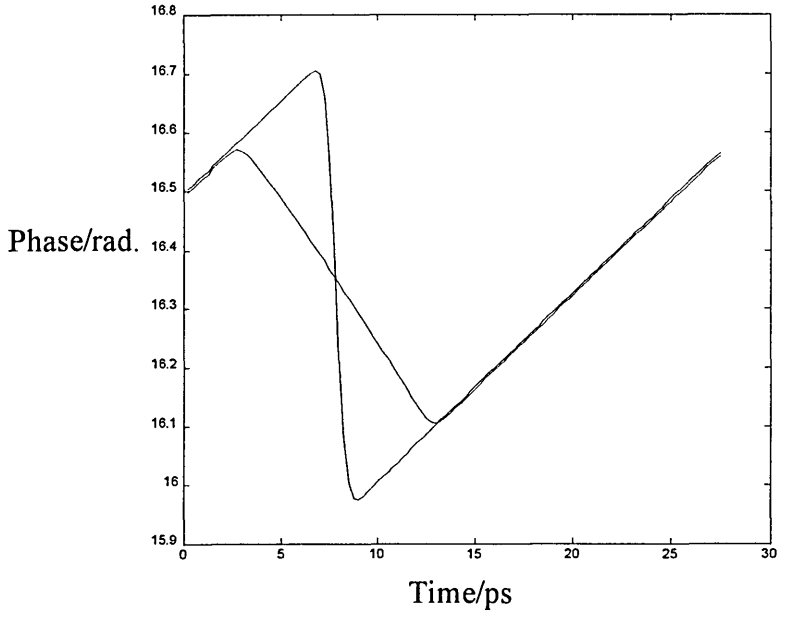

Figure 7.38 Phase response 40 GHz system

This time the CCW phase almost reaches the CW value and it occurs over a period $2T_L$ which is the finite length effect, the response is affected by this and carrier recombination. The simulated transmission is shown in figure 7.39.

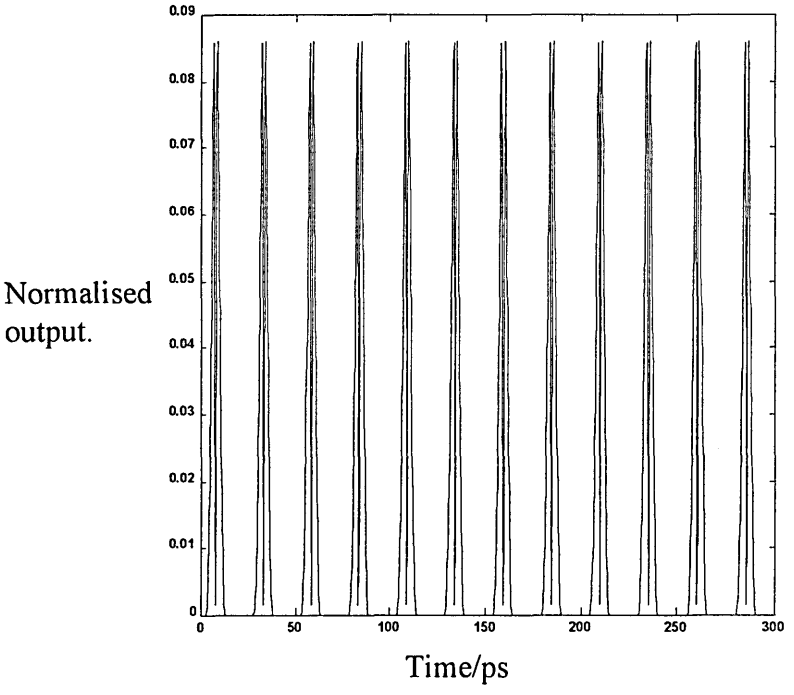

Figure 7.39 Loop transmission of 40 Gbit/s data system.

Figure 7.40 shows a single pulse which has the characteristic shape produced by an ASLALOM with the TWSLA placed at the loop centre. The transmission window width = $T_L \times 2$ and has a FWHM of T_L.

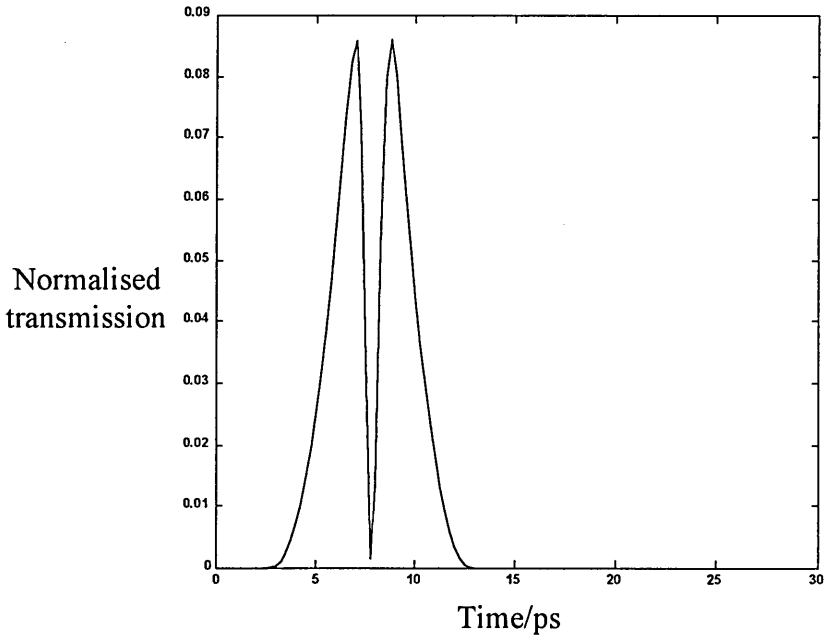

Figure 7.40 Single pulse of 40 Gbit/s data system.

7.5.5 Binary data input

The previous analysis centred around a continuous pulse input. The simulations will now look at data input consisting of zeros and ones (c.f. section 5.3.5). The input data stream chosen consists of a pulse pattern of 11100011110. An examination of figure 7.41 shows the phase temporal response of the CW data and the CCW data. The data rate in this case is 100 Gbit/s with a bias current of 200 mA.

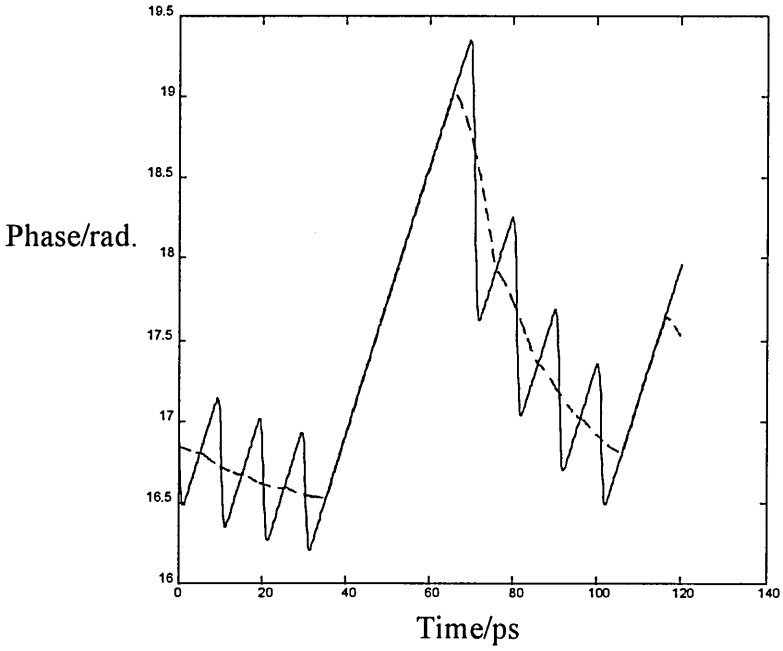

Figure 7.41 CW and CCW response of 100 Gbit/s data.

Note the response in figure 7.41 shows that a difference exists between the phase change for different bits. This is in agreement with the theoretical shape of the phase response of a TWSLA when a data pattern for the control is used [Manning et al 94]. Figure 7.42 shows the loop transmission due to the phase and gain response at this data rate.

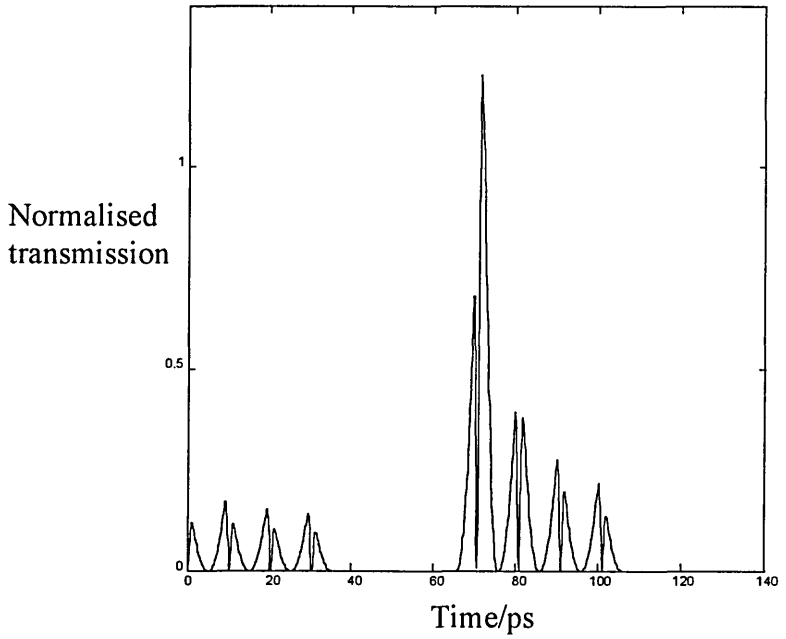

Figure 7.42 Transmission response of 100 Gbit/s data.

Evident again at this rate is the flat CCW response seen in the continuous pulse case. The transmitted pulses also show a marked variation in amplitude This configuration has been used by Ellis et al [Ellis 95] to wavelength convert a signal by inputting a continuous wave signal into port 1 and the data into the control coupler. It can be seen from figure 7.42 that pulses with a guard band cannot be generated. The relaxation time between pulses is again the main factor in the CCW modulation masking the finite length effect. The amplitude variation is a direct consequence of data input to an TWSLA which was described in section 3.5.1. A period of zeros (bits 5, 6 and 7) relaxes the carrier density over a longer period resulting in a higher carrier density for the following bit. From a carrier density rate equation (equation 2.15) a higher carrier density gives a larger carrier differential. The carrier density change over one bit period T is thus:

$$\Delta n \approx -\left(\frac{n}{\tau_2} + \Gamma a(n-n_0)I\right)T \qquad (7.35)$$

The result is a larger fall in carrier density with increasing n following a sequence of zeros (see figure 3.9). The simulated CW and CCW responses due to a 40 Gbit/s data stream with a bias current of 100 mA is shown in figure 7.43.

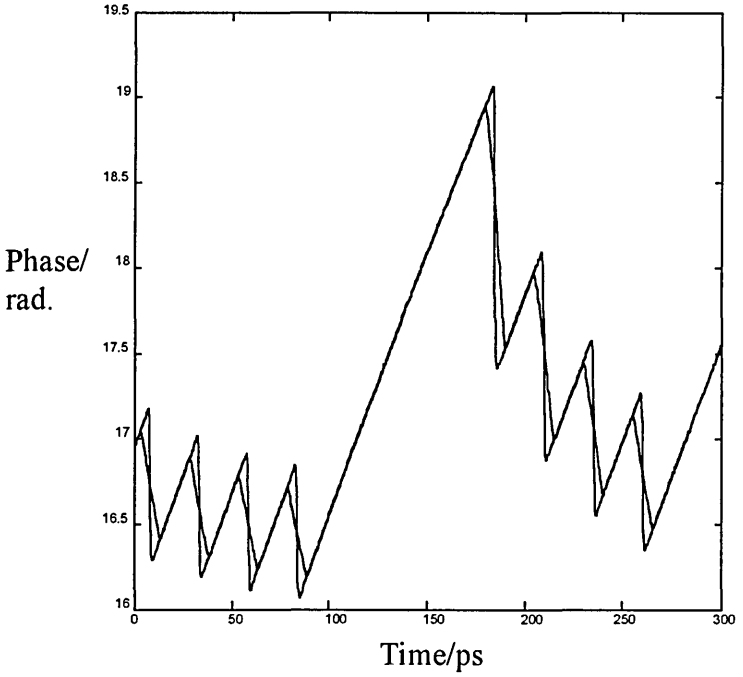

Figure 7.43 CW and CCW response of 40 Gbit/s data

Here the finite length effect begins to appear again. Figure 7.44 shows the transmission response giving a pulse width equal to T_L

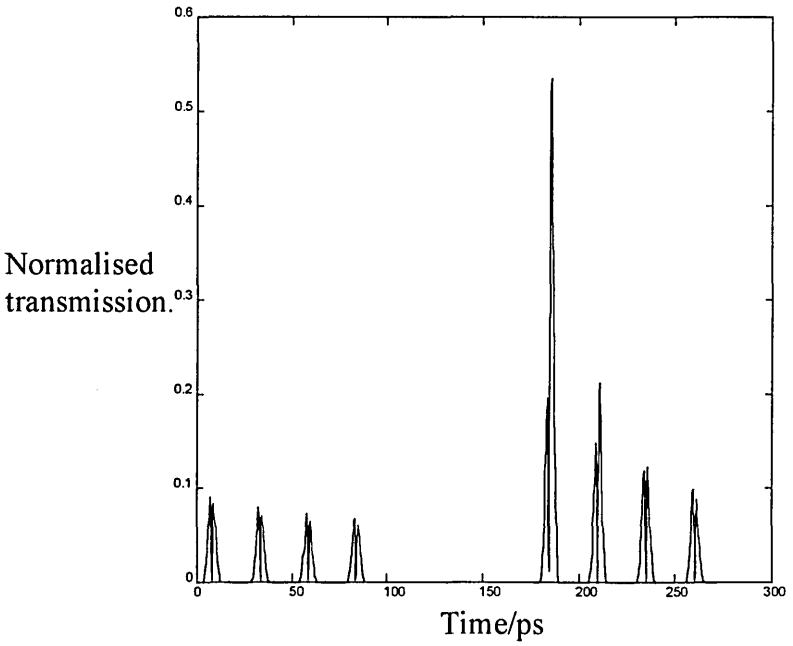

Figure 7.44 Transmission response of 40 Gbit/s data.

7.5.6 Patterning

The effect of patterning in a data driven ASLALOM will now be demonstrated using a 40 Gbit/s data signal. Section 5.3.5. pointed out the condition for patterning as an TWSLA with an asymmetry greater than the time between data pulses. The phase response with this asymmetry is shown in figure 7.45.

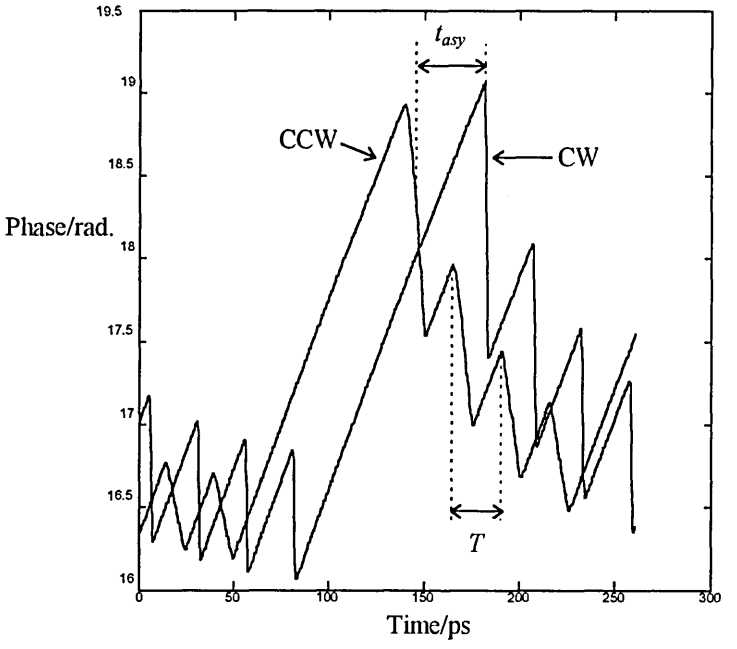

Figure 7.45 Phase response of data driven ASLALOM where $t_{asy} > T$.

The resulting transmission is shown in figure 7.46.

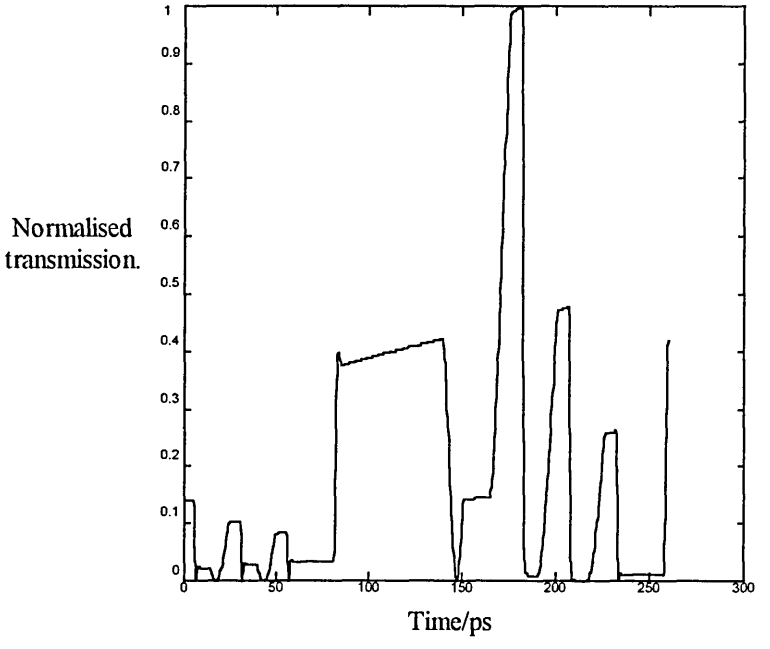

Figure 7.46 Patterning in an ASLALOM.

The transmission shows a significant departure from the transmission shown in figure 7.44 indicating that the simulation model can predict patterning as outlined in [Davies et al 95] who demonstrated patterning with 10 Gbit/s data and t_{asy} = 640 ps.

7.5.7 A method for multi-output data

Using data input as a control superimposes a binary pattern on a continuous wave signal at the input (port 1). An enhancement of this method is used to demonstrate a novel method of using the ASLALOM for multi channel output. Presently the ASLALOM is only operated as a single output device.

Consider initially the chirping effect of long lengths of fibre on optical pulses. One type of chirp produced by passing an optical pulse through a length of optical fibre is linear in frequency. The Kerr coefficient in an optical fibre (equation 5.9) produces a self phase modulation on a signal according to:

$$\phi(t) = \frac{2\pi(n_0 + n_2 I_0 e^{-2at^2})L_f}{\lambda} \tag{7.36}$$

where L_f is the fibre length the signal of wavelength λ propagates. The frequency imposed on the signal is given by:

$$\frac{d\phi}{dt} \approx \frac{4\pi a n_2 L_f t I_0 e^{-2at^2}}{\lambda} \tag{7.37}$$

which corresponds to a linear frequency chirp imposed on a pulse of centre frequency ω_0, by the intensity signal. The phase of the signal is given by:

$$\int \omega_0 t + 2bt = \omega_0 t + bt^2 + \psi \tag{7.38}$$

A linearly chirped pulse is thus described as:

$$E = A(t)(\exp(\omega_0 t + bt^2) + c.c) \tag{7.39}$$

An example of a linearly chirped Gaussian pulse is shown graphically in figure 7.47.

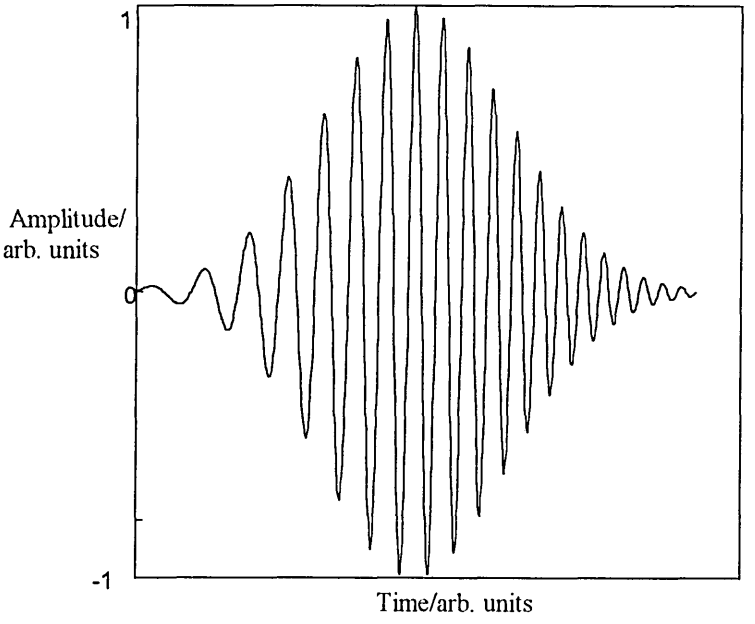

Figure 7.47 Gaussian pulse with linear chirp.

Pulse broadening will also occur through long lengths of fibre which can be incorporated into the pulse using a super Gaussian pulse shape which have been generated experimentally by [Morioka et al 94] and are described theoretically as [Agrawal and Olsson 89]:

$$I = I_0 e^{-2at^{2m}} \tag{7.40}$$

where m indicates the broadening factor. To implement multi-channel output the chirped pulse is input to the data driven loop in a similar manner to the continuous wave input previously described. The simulation assumes a chirp factor of 2.77 nm/10 ps which is taken from data given in [Uchiyama et al 96]. Here the chirped pulse was generated by passing the signal through a length of non-dispersion shifted fibre. If the input coupler is considered ideal, the loop output would be according to figure 7.48 which shows the linear frequency response of the output pulses due to the chirp. The pulse width in this

case was 80 ps. This gives a range of wavelength chirp equal to 8×2.77 = 22.16 nm (see figure 7.48).

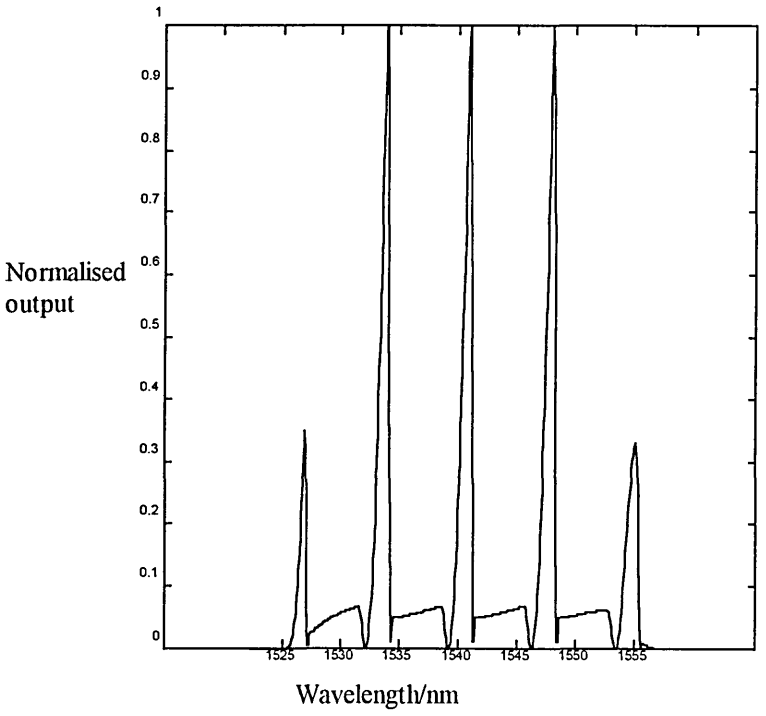

Figure 7.48
Simulated multichannel output with ideal coupler.

Note the Gaussian pulse shape has attenuated the extreme channels. The coupler of the ASLALOM has a wavelength dependent coupling (section 7.1) and the response over the linearly chirped region is given from a section of the typical raised cosine response as shown in figure 7.2. The coupler simulations will use parameters from two practical devices. The first is from a design by Morishita [Morishita and Shimamoto 95] and the second from [Mortimore 88]. The wavelength minimums for these devices occur at 1531 nm and 1553 nm, and 1200 nm and 1800 nm respectively. Figure 7.49 shows the coupling coefficient for both couplers over the chirp range and is simulated using equations 7.1, 7.2 and 7.3.

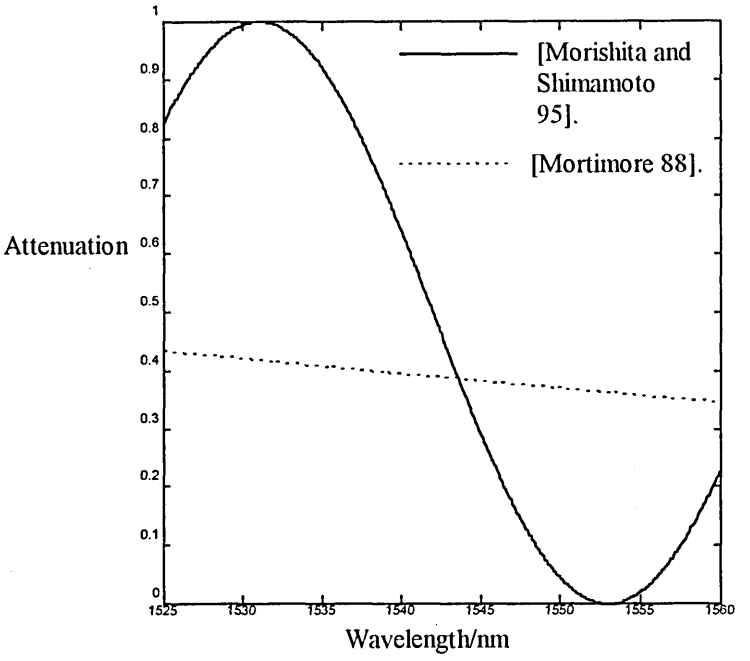

Figure 7.49 Coupling coefficients for chirp range.

The coupler from [Morishita and Shimamoto 95] will attenuate the signal over this range between ≈ 0.65 and ≈ 0.2 and this reduces the signal amplitude (figure 7.50).

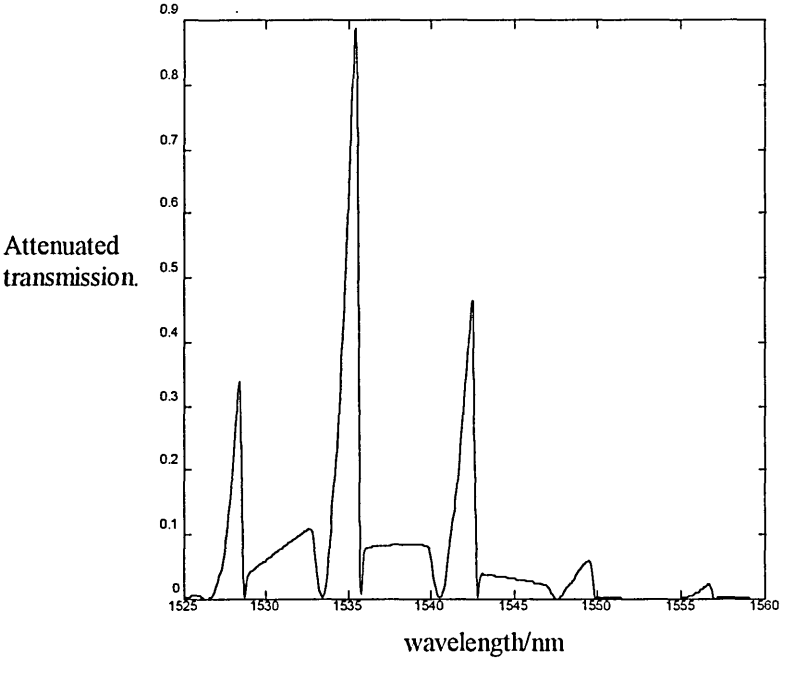

Figure 7.50 Loop response with coupler from [Morishita and Shimamoto 96].

In comparison with the coupling device from [Mortimer 88] it can be seen the response gives less attenuation over the range considered (see figure 7.51) and gives a flatter response over a wider frequency range which is advantageous for a system envisaged with more channels.

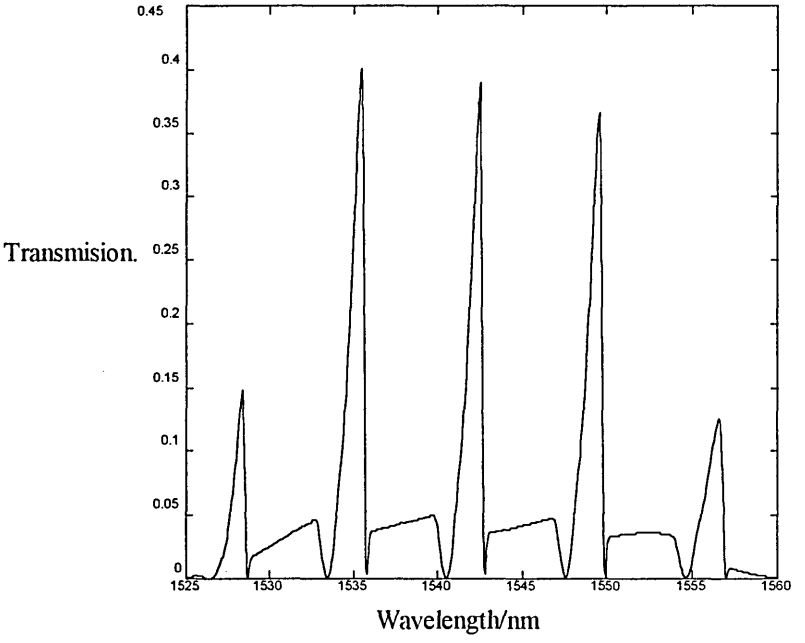

Figure 7.51 Loop response with coupler from [Mortimore 88].

7.6. Birefringence And Polarisation Effects In An ASLALOM.

7.6.1 Jones matrix of waveplate

In the ideal case, wave components will propagate at the same speed. The effects of birefringence or the introduction of a wave plate can change the phase propagation of one component to the other. Consider the case where a waveplate is inserted in the path of a travelling wave. To represent this a Jones matrix is described for the system. The waveplate makes an angle θ with the vertical y axis and the retardation of the plate is ϕ.

Figure 7.52 shows how an electric field can be resolved into x and y components which are incident on such a waveplate.

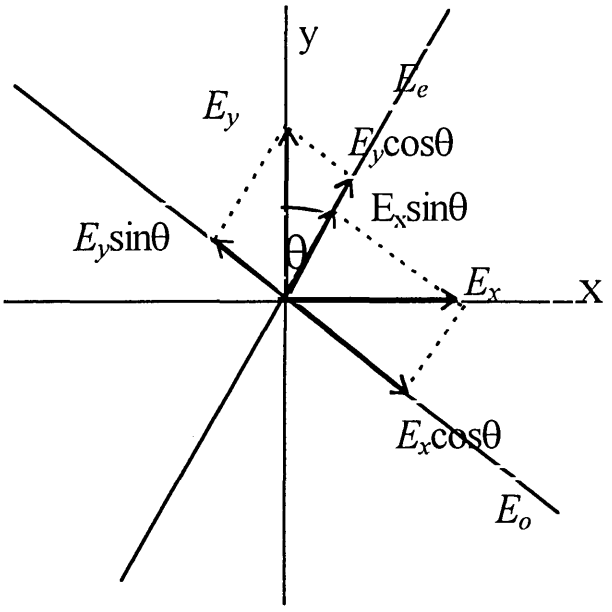

Figure 7.52 Electric field incident on a waveplate.

Each component is represented as a travelling wave of the form $\mathbf{E_S} = \mathbf{E_c}e^{j(\omega t - kz - \gamma)}$. The fast axis is given along E_f and the slow along E_O The signal wave is given by the vector sum:

$$\mathbf{E_x} + \mathbf{E_y} = \mathbf{E_s} \tag{7.41}$$

Initially the x and y components of the electric field are resolved into components along the E_e and E_o axis giving:

$$E_o = E_x\cos\theta - E_y\sin\theta \tag{7.42}$$

$$E_e = E_x\sin\theta + E_y\cos\theta \tag{7.43}$$

The signal vector in terms of $\mathbf{E_o}$ and $\mathbf{E_e}$ is shown in figure 7.52. On passing through the birefringent material the E_e component of the signal will undergo a phase shift equal to ϕ. The signal components are now modified to:

$$E_{o1} = E_x\cos\theta - E_y\sin\theta = E_o \tag{7.44}$$

$$E_{e1} = (E_x\sin\theta + E_y\cos\theta)(\exp(j\,\phi)) = E_e(\exp(j\,\phi)) \tag{7.45}$$

Resolving the E_e and E_o components back to the x and y directions gives:

$$E_y = (E_x\sin\theta + E_y\cos\theta)\cdot\exp(j\,\phi)\cdot\cos\theta - (E_x\cos\theta - E_y\sin\theta)\cdot\sin\theta \tag{7.46}$$

$$E_y = E_{e1}\cos\theta - E_{o1}\sin\theta) \tag{7.47}$$

$$E_x = (E_x\sin\theta + E_y\cos\theta)(\exp(j\,\phi))\sin\theta + (E_x\cos\theta - E_y\sin\theta)\cos\theta \tag{7.48}$$

$$E_y = E_{e1}\sin\theta + E_{o1}\cos\theta \tag{7.49}$$

Rearranging in terms of E_x and E_y components:

$$E_y = E_y(\cos^2\theta\cdot\exp(j\,\phi) + \sin^2\theta) + E_x(\sin\theta\cos\theta\exp(j\,\phi) - \cos\theta\sin\theta) \tag{7.50}$$

$$E_x = E_x(\sin^2\theta\cdot\exp(j\,\phi) + \cos^2\theta) + E_y(\cos\theta\sin\theta\exp(j\,\phi) - \sin\theta\cos\theta) \tag{7.51}$$

The transfer function for these equations is:

$$\begin{pmatrix} E_y' \\ E_x' \end{pmatrix} = \begin{pmatrix} J_{yy} & J_{yx} \\ J_{xy} & J_{xx} \end{pmatrix}\begin{pmatrix} E_y \\ E_x \end{pmatrix} \tag{7.52}$$

where:

$$J_{yy} = \cos^2\theta\cdot\exp(j\,\phi) + \sin^2\theta \tag{7.53}$$

$$J_{xx} = \sin^2\theta\cdot\exp(j\,\phi) + \cos^2\theta \tag{7.54}$$

$$J_{yx} = J_{xy} = (\exp(j\,\phi) - 1)\cos\theta\sin\theta \tag{7.55}$$

where J_{mn} represent the Jones matrix coefficients.

The fibre loop has E_x and E_y components which travel counter directionally. The waveplate is non-reciprocal and a reverse wave propagates with coefficients:

$$J_{yy} = \cos^2\theta\cdot\exp(j\,\phi) + \sin^2\theta \tag{7.56}$$

$$J_{xx} = \sin^2\theta\cdot\exp(j\,\phi) + \cos^2\theta \tag{7.57}$$

$$J_{yx} = J_{xy} = (1 - \exp(j\,\phi))\cos\theta\sin\theta \tag{7.58}$$

7.6.2 Waveplate in a fibre loop

The waveplate description now needs to be entered into the ASLALOM matrix. As an example consider the E_{1x} field leaving the loop and the effect of the E_{1x} components and E_{1y} components due to the waveplate. The E_{1y} field leaves the coupler and meets a waveplate halfway around the loop and from the waveplate analysis E_{1y} now produces an Ey and E_x component in equation 7.12. On returning to the coupler E_x now contains a contribution from the element m_{12} in equation 7.12 which contains information of the effect of the y field on the x field.

The transmission vector now has the modified form:

$$\begin{bmatrix} T_{ix} \\ T_{iy} \\ T_{2x} \\ T_{2y} \end{bmatrix} \begin{bmatrix} E_{1x} * E_{1x} \\ E_{1y} * E_{1y} \\ E_{1x} * E_{1x} \\ E_{1y} * E_{1y} \end{bmatrix} = \begin{bmatrix} (m_{11}E_{1x})* \\ (m_{22}E_{1y})* \\ (m_{31}E_{1x})* \\ (m_{42}E_{1x})* \end{bmatrix} \begin{bmatrix} m_{11}E_{1x} \\ m_{22}E_{1y} \\ m_{31}E_{1x} \\ m_{42}E_{1x} \end{bmatrix} + \begin{bmatrix} (m_{12}E_{1x})* \\ (m_{22}E_{1y})* \\ (m_{32}E_{1x})* \\ (m_{41}E_{1x})* \end{bmatrix} \begin{bmatrix} m_{12}E_{1x} \\ m_{21}E_{1y} \\ m_{32}E_{1x} \\ m_{41}E_{1x} \end{bmatrix} \tag{7.59}$$

$$\begin{bmatrix} T_{ix} \\ T_{iy} \\ T_{2x} \\ T_{2y} \end{bmatrix} \begin{bmatrix} |E_{1x}|^2 \\ E_{1y} \\ E_{1x} \\ E_{1y} \end{bmatrix} = \begin{bmatrix} m_{11} * m_{11} \\ m_{22} * m_{22} \\ m_{31} * m_{31} \\ m_{42} * m_{42} \end{bmatrix} \begin{bmatrix} |E_{1x}|^2 \\ E_{1y} \\ E_{1x} \\ E_{1y} \end{bmatrix} + \begin{bmatrix} m_{12} * m_{12} \\ m_{21} * m_{21} \\ m_{32} * m_{32} \\ m_{41} * m_{41} \end{bmatrix} \begin{bmatrix} |E_{1x}|^2 \\ E_{1y} \\ E_{1x} \\ E_{1y} \end{bmatrix} \tag{7.60}$$

Equation 7.47 takes into account the field amplitudes of the x and y components, a simplification will be used in the following analysis where $|E_{mx}|^2 = |E_{my}|^2$ giving:

$$\begin{bmatrix} T_{ix} \\ T_{iy} \\ T_{2x} \\ T_{2y} \end{bmatrix} = \begin{bmatrix} m_{11} * m_{11} \\ m_{22} * m_{22} \\ m_{31} * m_{31} \\ m_{42} * m_{42} \end{bmatrix} + \begin{bmatrix} m_{12} * m_{12} \\ m_{21} * m_{21} \\ m_{32} * m_{32} \\ m_{41} * m_{41} \end{bmatrix} \tag{7.61}$$

Figure 7.53 shows how transmission and reflection are affected in the presence of birefringence using different delay waveplates.

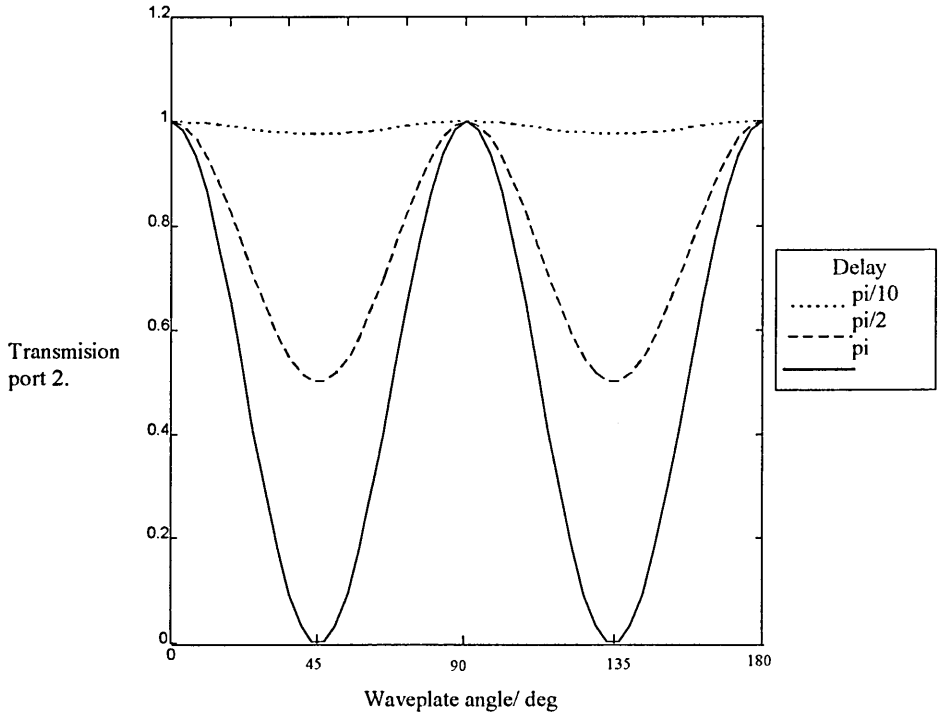

Figure 7.53
Transmission and reflection of ASLALOM for different waveplates.

The loop is normally in transmission mode by setting the CCW phase at π relative to the CCW phase. The different waveplates show varying levels of effect on the loop transmission. The most notable is the π delay which can effectively switch the whole of the ASLALOM output from port 2 to port 1. Delays less than π show only partial switching. In this mode the waveplate can effectively switch off or re-route a particular channel in an OTDM system. [Mortimore 88] demonstrated practically the effect of a halfwave plate in a fibre loop reflector and the results compare well with figure 7.53. Notably the transmission is fully re-routed at a waveplate angle of 45°, and both experimental and simulated results have a shape given by a raised cosine. Figure 7.54 shows the amount of signal that can be re-routed for a particular waveplate delay.

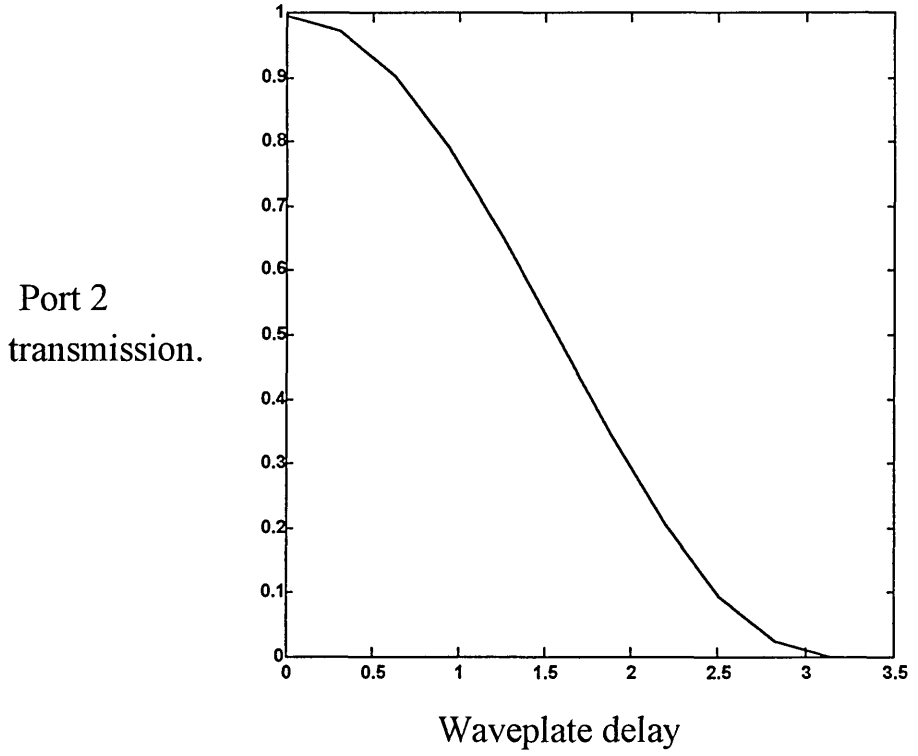

Figure 7.54 Transmission with waveplate in ASLALOM.

The transmission of a loop with a waveplate included has been demonstrated practically by [Eiselt 92] where adjustment of the polarisation in a loop is used to set a SLALOM to reflect or transmit a signal.

7.6.3. Birefringence in ASLALOM.

Birefringence in a fibre loop can occur due to bends and twist within the fibre [Mortimore 88]. Desruelle [Desruelle 95] has used the waveplate to describe the effects of dispersion and walk off in a NOLM. Using this method the loop is considered to possess birefringence modelled in the form of a waveplate with associated delay and angle. Figure 7.55 shows the effect of a π waveplate in a ASLALOM configuration.

7.6.2 Waveplate in a fibre loop

The waveplate description now needs to be entered into the ASLALOM matrix. As an example consider the E_{1x} field leaving the loop and the effect of the E_{1x} components and E_{1y} components due to the waveplate. The E_{1y} field leaves the coupler and meets a waveplate halfway around the loop and from the waveplate analysis E_{1y} now produces an E_y and E_x component in equation 7.12. On returning to the coupler E_x now contains a contribution from the element m_{12} in equation 7.12 which contains information of the effect of the y field on the x field.

The transmission vector now has the modified form:

$$\begin{bmatrix} T_{ix} \\ T_{iy} \\ T_{2x} \\ T_{2y} \end{bmatrix} \begin{bmatrix} E_{1x} * E_{1x} \\ E_{1y} * E_{1y} \\ E_{1x} * E_{1x} \\ E_{1y} * E_{1y} \end{bmatrix} = \begin{bmatrix} (m_{11}E_{1x})* \\ (m_{22}E_{1y})* \\ (m_{31}E_{1x})* \\ (m_{42}E_{1x})* \end{bmatrix} \begin{bmatrix} m_{11}E_{1x} \\ m_{22}E_{1y} \\ m_{31}E_{1x} \\ m_{42}E_{1x} \end{bmatrix} + \begin{bmatrix} (m_{12}E_{1x})* \\ (m_{22}E_{1y})* \\ (m_{32}E_{1x})* \\ (m_{41}E_{1x})* \end{bmatrix} \begin{bmatrix} m_{12}E_{1x} \\ m_{21}E_{1y} \\ m_{32}E_{1x} \\ m_{41}E_{1x} \end{bmatrix} \tag{7.59}$$

$$\begin{bmatrix} T_{ix} \\ T_{iy} \\ T_{2x} \\ T_{2y} \end{bmatrix} \begin{bmatrix} |E_{1x}|^2 \\ E_{1y} \\ E_{1x} \\ E_{1y} \end{bmatrix} = \begin{bmatrix} m_{11} * m_{11} \\ m_{22} * m_{22} \\ m_{31} * m_{31} \\ m_{42} * m_{42} \end{bmatrix} \begin{bmatrix} |E_{1x}|^2 \\ E_{1y} \\ E_{1x} \\ E_{1y} \end{bmatrix} + \begin{bmatrix} m_{12} * m_{12} \\ m_{21} * m_{21} \\ m_{32} * m_{32} \\ m_{41} * m_{41} \end{bmatrix} \begin{bmatrix} |E_{1x}|^2 \\ E_{1y} \\ E_{1x} \\ E_{1y} \end{bmatrix} \tag{7.60}$$

Equation 7.47 takes into account the field amplitudes of the x and y components, a simplification will be used in the following analysis where $|E_{nx}|^2 = |E_{ny}|^2$ giving:

$$\begin{bmatrix} T_{ix} \\ T_{iy} \\ T_{2x} \\ T_{2y} \end{bmatrix} = \begin{bmatrix} m_{11} * m_{11} \\ m_{22} * m_{22} \\ m_{31} * m_{31} \\ m_{42} * m_{42} \end{bmatrix} + \begin{bmatrix} m_{12} * m_{12} \\ m_{21} * m_{21} \\ m_{32} * m_{32} \\ m_{41} * m_{41} \end{bmatrix} \tag{7.61}$$

Figure 7.53 shows how transmission and reflection are affected in the presence of birefringence using different delay waveplates.

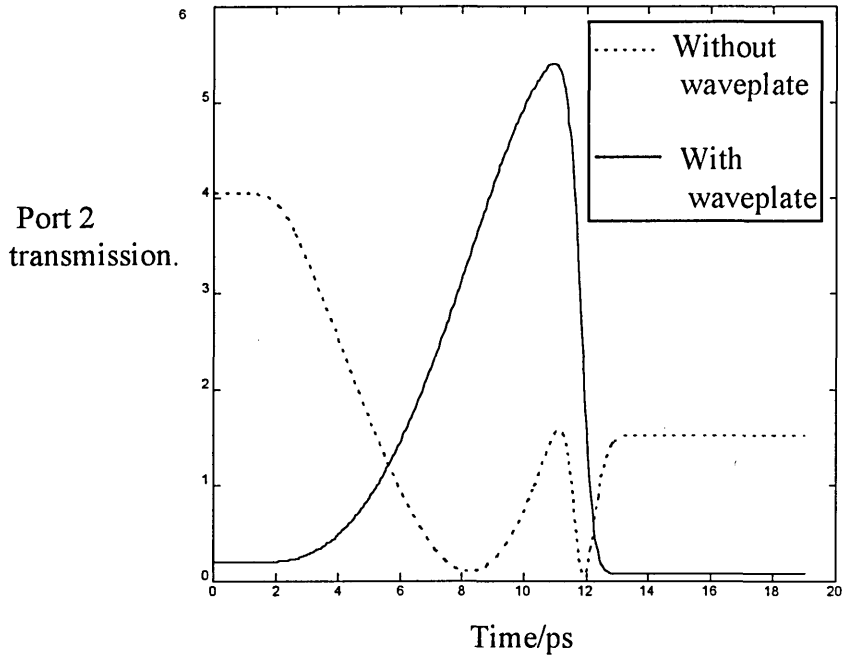

Figure 7.56 Compensating loop birefringence.

Similarly Mortimore [Mortimore 88] demonstrated how the addition of an extra halfwave plate in a fibre loop reflector can re-route the power to the opposite port when a single halfwave plate is present. Note that the addition of a waveplate with a different delay to one already present in the loop will not fully compensate for the birefringence.

7.7 Summary

This chapter has presented the authors model of an ASLALOM which incorporates the TWSLA model developed in chapter 6. Initially the coupler was modelled and was in good agreement with a practical device. A model of the full loop was then developed and when used as a demultiplexer of low data rates the analysis proves to be the simpler with the point element model of the TWSLA in chapter 6 sufficient. This model was used for the large and medium asymmetry loops and compared favourably with experimental

results. The large asymmetry showing two transmission windows as in the practical system, the medium asymmetry transmission window width was within 7% of experimental data. For higher data rates where the TWSLA is moved close to the loop centre a finite length model is required. Initial simulations show that the ASLALOM opens a sampling window which is asymmetric in shape and comparisons with experimental data show the model to be in agreement with these over a range 4.5% to 12.5%. The model is then used to simulate the case where modulated data is used to modulate the loop, the response agreed in principle with a previous theoretical response. With these techniques to hand, a novel method of multi-channel output (section 7.5.7) is demonstrated in principle which shows how one loop can be used for this purpose. A model to simulate birefringence effects was also developed to assess the performance of the loop which agreed with previous experiments on a fibre loop.

Chapter 8

Conclusions And Suggestions For Further Work

8.1 Conclusions

This thesis has been concerned with developing a model for an OTDM system based around the experimental architecture known as the ASLALOM. Fundamental to the operation of such a system is the inclusion of a non-linear element in the form of a TWSLA. The TWSLA is included in a fibre loop mirror and the principle of operation stems from previous architectures which use a long length of fibre as the NLE. The TWSLA has a disadvantage in that it has a slow recovery time which makes it seem unsuitable for high speed switching. The advantage of low power requirements when using a TWSLA prompted research into this area. The use of short fibre loops removes the problems associated with attenuation and dispersion. The modelling and simulations have been divided into two areas.

The modelling of the TWSLA is considered separately because of the various techniques used and the diverse nature of the signal input. The modelling techniques have been divided into two areas dependent on the type of signal input. For high frequency pulse input or continuous intensity signals the model uses a continuous wave analysis. This is the simpler of the two and uses a laser rate equation which is a derivative of the carrier density in the device. The simplifications allowed in the use of laser rate equations were identified and justified and include homogeneous broadening which removed the necessity for a set of equations for each signal frequency. The continuous wave analysis

allowed the rate equation to be used in steady state. The analysis used an approach in which the amplifier was divided into a number of segments equations being solved numerically for each segment. An analytical expression has been developed which is simpler and comparisons made with the numerical method. The analytical method proves to be of use with high input powers of the order of 10 times the saturation value. The aim of a continuous wave model was to provide information regarding the channels in an OTDM system.

The TWSLA was also modelled dynamically to analyse the variation in its properties when a time varying input is used. This type of signal is the control in an OTDM system. The equations are solved without recourse to steady state methods and to implement this a method of longitudinally averaging the signal within the device was used. Comparisons with reported results are made on transmission properties. This gives an indication of the temporal nature of the response to pulse input and the model shows the characteristic short fall time and long rise time reported in laboratory results. The carrier density is related to the transmission and phase and gain responses can be calculated using appropriate equations. The phase response shows a phase difference of π is achievable with moderate current input. This would give maximum power transfer when using the TWSLA in an interferomic device.

The previous analysis gave information on the time response of a signal and treated the TWSLA as a single point with zero dimensions. To analyse the model with time and space information a finite length model was used. This used a matrix analysis of the TWSLA which was assisted by the matrix processing capabilities of the software

package MATLAB™. The information was then available in matrix form. The TWSLA models were compared with previously reported experiments and simulations and were found to be in good agreement.

With a model of the TWSLA available for all inputs to the ASLALOM the next step identified the equations necessary for analysing the loop as a whole. The coupler, an integral part of the loop, was identified as a wavelength dependent component and the description included an expression to reflect this which follows the raised cosine response of practical devices. The analysis of the ASLALOM was approached by tracing the signal path around the loop. This gave a series of components which could be multiplied together to form a comprehensive matrix description of the whole loop. This description allowed the input to be of a polarised nature with signals consisting of orthogonally placed components. Initially, polarisation was not considered and intensity signals were considered. Fundamental to the loop is the placing of the TWSLA and this was considered with the loop described as having large, medium or small asymmetry. The first two gave a simple analysis with the TWSLA information input to the loop matrix directly. The model shows that the large asymmetry would demultiplex two data channels and is of little use in a slow data rate system. The medium asymmetry can demultiplex signals at rates approaching 1/2 the recombination time. The small asymmetry loop required a more thorough investigation and utilised the finite length model of the TWSLA. The transmission in this configuration showed that the switching frequency now depended on the TWSLA length. The transmission window was equal to twice the propagation time of the TWSLA which suggests Terahertz switching frequencies for a 100 μm device. As devices commonly used are based around a length of 500 μm this was

the length used for simulations. The characteristics of the window simulated showed excellent agreement with an experimental set up and in addition this gave a check on the accuracy of the finite length model. The ASLALOM was simulated with pulsed data input at 250 Gbit/s, this also having been demonstrated experimentally by other workers. The simulation suggest a significant amount of crosstalk appeared which has not been described in the laboratory. The ASLALOM also provided signal gain which is a feature uncommon to most switching devices as outlined in chapter 4.

The ASLALOM has also been demonstrated with a data signal for the control input. This was demonstrated first by simulations with high frequency input. These simulations showed the finite length effect was less evident for bit rates at 100 Gbit/s but was noticeable for lower frequencies (around 40 Gbit/s). With this type of control input a method of generating multi-channel output was demonstrated. To check the validity of the simulations for data input the results were compared with recently reported theoretical predictions giving good agreement with the shape of the response.

The polarisation aspect was considered next by including birefringence effects in the loop. The aim of this was two fold (i) to introduce and investigate the effect of placing polarisation components into the loop and (ii) to demonstrate the feasibility of compensating for birefringence in the loop. The first method introduced a waveplate into the loop where it was demonstrated that the loop could be switched on or off depending on the waveplate angle. It was also shown that any birefringence in the loop could be compensated by the introduction of a waveplate in the loop. Experimental results of a

waveplates in a fibre loop without a TWSLA have been published and this was used to check the accuracy of this model, good comparisons were reported.

8.2 Suggestions For Further Work

The emphasis on this work has been to develop a model of the ASLAOM with regard to examining the temporal switching window obtainable with this configuration. With models of this type not yet reported it is clear that an initial model such as this will omit some aspects. There are various areas in which the analysis can be taken further. Chapter 3 indicated that the TWSLA was a source of noise and this will be a factor in signal to noise ratio considerations and ultimately the bit error rate. Experimental results published contain results of the bit error rate where comparisons can be made. The model can be used to asses the performance of higher data rate systems, e.g. using a 100 μm TWSLA in the ASLALOM suggests switching speeds of 1 Terabit/s are attainable. The use of ultrashort pulses within the TWSLA are giving interesting results and is an area which could be pursued, particularly in the effect of the fast components on switching speeds. If it is the case that shorter pulses can be demultiplexed due to this effect then gain dispersion of the TWSLA may be investigated as this is more pronounced on short pulses. A further aspect could involve the modelling of the system of an integrated device with the emerging technology of waveguiding technology which has allowed integration in the Mach Zender version.

The following list of publications have been produced from this work.

1. G. Swift, A.K. Ray, Z. Ghassemlooy and J.R. Travis, 'Modelling of semiconductor laser amplifier for optical time division demultiplexing' , *Third Comm. Network Symposium, Manchester Metroplolitan University*, pp. 35-38, July 1996.

2. G. Swift, A.K. Ray, Z. Ghassemlooy, 'Modelling of semiconductor laser amplifier for terahertz optical asymmetric demultiplexer', *Mid-infrared Optoelectronics Materials and Devices, International Conference*, September 1996.

3. G. Swift, A.K. Ray, Z. Ghassemlooy and J.R. Travis , Modelling of an all optical time division demultiplexer, *To be published in Microwave and Opt. Technol. Lett.*, August 1997.

4. G. Swift, A.K. Ray, Z. Ghassemlooy, 'Modelling of semiconductor laser amplifier for terahertz optical asymmetric demultiplexer', *To be published in IEE Proceedings-Circuits Devices and Systems*, 1997.

References

M.J. Adams, J.V. Collins, I.D. Henning, 'Analysis Of Semicondutor Laser Amplifiers', *IEE Proc. J*, **132**, (1), pp. 58-63, February 1985.

M.J. Adams, D.A.O. Davies, M.C. Tatham and M.A. Fisher, 'Nonlinearities in semiconductor laser-amplifiers *Opt. and Quantum Electron.*, **27**, (1), pp. 1-13, 1995.

G.P. Agrawal, 'Effect of gain dispersion on ultrashort pulse amplification in semiconductor laser amplifiers', *IEEE J.Quantum Electron*, **QE-27**, (6), pp. 1843-1849, June 1991.

G.P. Agrawal, *Fibre optic communication systems*, John Wiley & Sons inc., 1986.

G.P. Agrawal and N.A. Olsson, 'Self-phase modulation and spectral broadening of optical pulses in semiconductor laser amplifiers', *IEEE J. Quantum Electron.*, **QE-25**, (11), pp. 2297-2306, November 1989.

R.C Alferness, L.L. Buhl, M.J.R. Martyak, M.D.Divino, C.H. Joyner and A.G. Dentai, ' Narrowband GaInAsP/InP waveguide grating-folded directional coupler multiplexer demultiplexer', *Electron. Lett.*, **24**, (3), pp. 150-151, February 1988.

P.A. Andrekson, N.A. Olsson, J.R. Simpson, T. Tanbun-ek, R.A. Logan and M. Haner, '16 Gbit/s all-optical demultiplexing using four wave mixing', *Electron. Lett.*, **27**, (11), pp. 922-924, May 1991.

A.G. Bell, 'Selenium and the photophone', *The Electrician*, pp. 214, 215, 220,221, 1880.

N.S. Bergano and C.R. Davidson, 'Wavelength division multiplexing in long-haul transmission systems', *J. Lightwave Technol.*, **LT-14**, (6), pp. 1299-1308, June 1996.

L.C. Blank, 'Multi-GBit/s optical time division multiplexing employing $LiNbO_3$ switches with low-frequency sine wave drive', *Electron. Lett.*, **24**, (25), pp. 1543-1544, december 1988.

K.J. Blow, N.J. Doran and B.P. Nelson, ' Demonstration of the Non-linear Fibre Loop Mirror As An Ultrafast All Optical Demultiplexer', *Electron Lett*, **26,** (14), pp. 962-964, July 1990.

M.E. Bray and M.J. O'Mahony, 'Cascading gain saturation semiconductor laser-amplifier wavelength translators, *IEE Proc. Optoelectron.*, **143**, (1), pp. 1-6, February 1996.

D.T. Cassidy, C. Derwyn, C. Johnson and K.O. Hill, 'Wavelength dependence transmission of monomode optical fibre tapers', *Appl. Opt.*, **24**, (7), pp. 945-950, April 1985.

I. P. Christov, Propagation of short optical pulses in dispersive medium, *IEEE J. Quantum. Electron*, **QE-24**, (8), pp. 1548-1553, August 1988.

M.F. Dautartas, A.M. Benzoni, Y.C. Chen, G.E. Blonder, B.H. Johnson, C.R. Paolo, E. Rice and Y.H. Wong', 'A silicon-based moving-mirror optical switch', *J. Lightwave Technol.*, **10**, (8), pp. 1078-1085, August 1992.

D.A.O. Davies, A.D. Ellis, T. Widdowson and G. Sherlock, '10 Gbit/s data switched semiconductor laser amplifier nonlinear looop mirror', *Electron. Lett.*, **31**, (2), pp. 111-112, January 1995.

P.J. Delfyett, Y. Silberberg and G.A. Alphonse, 'Hot-carrier thermalisation induced self phase modulation in semiconductor travelling wave amplifiers', *Appl. Phys. Lett.*, **59**, (1), pp. 10-12, July 1991.

B. Desruelle, E. Desurvie and S. Bigo, 'Analysis of the polarisation group velocity dispersion effect in polarisation-independent nonlinear-optical loop mirror demultiplexers', *Opt. Lett.*, **20**, (50), pp. 516-518, March 1995.

P.J. Duthie and M.J. Wale, '16×16 optical switch array in lithium niobate', *Electron. Lett.*, **27**, (14), pp. 1265-1266, July 1991.

M. Eiselt, 'Optical loopmirror with semiconductor laser amplifier', *Electron. Lett.*, **28**, (16), pp. 1505-1507, July 1992.

M. Eiselt, W. Pieper and H.G.Weber, 'All-optical high speed demultiplexing with a semiconductor laser amplifier in a loop mirror configuration', *Electron. Lett.*, **29**, (13), pp. 1167-1168, June 1993.

M. Eiselt, W. Pieper and H.G. Weber,' SLALOM: Semiconductor laser amplifier in a loop mirror', *J. Lightwave Technol.*, **13**, (10), pp. 2099-2110, October 1995.

G. Eisenstein, P.B. Hansen, J.M.Wiesenfeld, R.S. Tucker and G. Raybon, 'Amplification of high repitition rate picosecond pulses using an InGaAsP travelling-wave optical amplifier', *Appl. Phys. Lett.*, **53**, (16), pp. 1539-1541, October 1988.

G. Eisenstein and R.M Jopson, 'Measurements of the gain spectrum of near-travelling-wave and Fabry Perot semiconductor laser amplifiers', *Int. J. Electron.*, **60**, (1), pp. 113-121, 1986.

A.D. Ellis, D.A.O. Davies, A. Kelly and W.A. Pender, 'Data driven operation of semiconductor amplifier loop mirror at 40 Gbit/s', *Electron. Lett.*, **31**, (15), pp. 1245-1247, July 1995.

A.D. Ellis, D.M. Patrick, D. Flannery, R.J. Manning, D.A.O. Davies an D.M. Spitrit, 'Ultra-high speed OTDM networks using semiconductor amplifier-based processing nodes', *J. Lightwave Technol.*, **13**, (5), pp.761-770, May 1995.

A.D. Eliss and D.M. Spirit, ' Compact 40 Gbit/s optical demultiplexer using a GaInAsP optical amplifier, *Electron. Lett.*, **29**, (24), pp. 2115-2116, November 1993.

A.D. Ellis, T. Widdowson, X. Shan and D.G. Moodie, 'Three-node 40 GBit/s OTDM network experiment using electro-optic switches', *Electron. Lett.*, **30**, (16), pp. 1333-1334, August 1994.

J. Fan, G. Jacobsen and L. Kazovsky, 'Preamplifier ASK system performance with incomplete ASK modulation: Influence of ASE and laser phase noise', *J. Lightwave Tecnol.*, **LT-13**, (2), pp. 302-311, February 1995.

D.S. George and M.W. McCall, 'Control of nearly degenerate four-wave nixing in a distributed feedback semiconductor laser amplifier via coherent electrical modulation' *IEE Proc. Optoelectron.*, **141**, (1), pp. 33-37, February 1994.

L. Gillner, 'Comparative study of some travelling-wave semiconductor laser amplifier models', *IEE Proc. J.*, **139**, (5), pp. 339-347, October 1992.

L. Gillner, 'Modulation properties of a near travelling-wave semiconductor laser amplifier', *IEE Proc. J.*, **139**, (5), pp.331-338, October 1992.

I. Glesk and P.R. Prucnal, '250 Gbit/s self clocked optical TDM with a polarisation multiplexed clock', *Fiber and Integrated Optics*, **14**, pp. 71-82, 1995.

I. Glesk, J.P. Sokoloff and P.R. Prucnal, 'Demonstration of all-optical demultiplexing of TDM data at 250 Gbit/s', *Electron. Lett.*, **30**, (4), pp. 339-341, February 1994.

E.L. Goldstein, L. Eskilden and AF. Elrefaie, 'Performance implications of component crosstalk in transparent lightwave networks', *IEEE Photonics Technol. Lett.*, **6**, pp. 657-660, 1994.

M.J. Guy, J.R. Taylor, D.G. Moodie and A.E. Kelly, '10 GHz 3ps actively mode-locked ring laser incorporating a semiconductor laser amplifier and an electro-absorption modulator', *Electron. Lett.*, **32**, (24), pp. 2240-2241, November 1996.

K.L. Hall, J. Mark, E.P. Ippenand G. Eisenstein, 'Femtosecond gain dynamics in InGaAsP optical amplifiers', *Appl. Phys. Lett.*, **56**, (18), pp. 1740-1742, April 1990.

P.O. Hedekvist, P.A. Andrekson and K. Bertilsson, 'Impact of spectral inverter fibre length on four-wave mixing efficiency and signal distortion', *J. Lightwave Technol.*, **lt-13**, (9), p. 1815, september 1995.

K. Al-Hemyari, J.S. Aitchinson, C.N. Ironside, G.T. Kennedy, R.S. Grant and W. Sibbett, 'Ultrafast all optival switching in GaAlAs integrated interferometers in 1.55μm spectral region', *Electron Lett*, **28**, 12, pp.1090-1092, June 1992.

I.D. Henning, M.J. Adams and J.V. Collins, 'Performance predictions from a new optical amplifier model', *IEEE J. Quantum Electron.*,**QE-21**, (6), pp. 609-613, June 1985.

G.R. Hill, P.J. Chidgey, F. Kaufhold, T. Lynch, O. Sahlen, M. Gustavsson, M. Janson, B. Lagerstrom, G. Grasso, F. Meli, S. Johansson, J. Ingers, L. FErnandez, S. Rotolo, A. Antonionelli, S. Tebaldini, E. Vezzoni, R. Caddedu, N. Caponio, F. Testa, A. Scavennec, M.J. O' Mahony, J. Zhou, A. Yu, W. Sohler, U. Rust and H. Herrmann, ' Atransport network layer based on optical network elements', *J. Lightwave Technol.*, **LT-11**, pp. 667-680, 1993.

D. Hondros, P. Debye 'Elektromagnetische Wellen An Dielektrischen Draehten'. *Annal Physik.*, **4**. Folge, 32, pp. 465- 476.

M.Y. Hong, Y.H. Chang, A. Dienes, J.P. Heritage and P.J. Delfyett, 'Subpicosecond pulse amplifaication amplification in semiconductor laser amplifiers: theory and experiment', *IEEE J. Quantum Electron.*, **QE-30**, (40), pp. 1122-1131, April 1994.

W. Hunziker, W. Vogt, H. Melchior, D. Leclerc, P. Brosson, F. Pommereau, R. Ngo, P. Doussiere, F. Mallecot, T. Fillion, I. Wamsler and G. Laube. 'Self aligned flip-chip pacakaging of tilted semiconductor optical amplifier arrays on Si motherboard', *Electron. Lett.*, **31**, (6), pp. 488-490, March 1995.

K. Innoue, T. Mukai and T. Saitoh, 'Gain saturation dependence on signal wavlength in a travelling wave semiconductor laser amplifier', *Electron. Lett.*, **23**, (7), pp. 328-329, 1987.

K. Innoue and M. Yoshino, 'Gain dynamics of a saturated semiconductor laser amplifier with 1.47 μm LD pumping', *IEEE Photonics Technol. Lett.*, **8**, (4), pp. 506-508, Aptil 1996.

M.N. Islam, 'Ultrafast switching with non linear optics', *Physics Today*, pp.34-40, May 1994.

J.L. Jackel, M.S. Goodman, J.E. Baran, W.J. Tomlinson, Gee-Kung Chang, M.Z. Iqbal, G.H. Song, K. Bala, C.A. Brackett, D.A. Smith, R.S. Chakravarthy, R.H. Hobbs, D.J. Fritz, R.W. Ade and K.M. Kissa, ' Acousto-optic tunable filters (AOTF) for multiwavelength optical cross-connects: crosstalk considerations', *J. Lightwave Technol.*, **LT-14**, (6), pp. 1056-1066, June 1996.

S. Jensen, 'The non linear coherent coupler', *IEEE Trans. on Microwave Theory and Techniques,* **MTT-30**, (10), pp. 1568-1571, October 1982.

C. Joergensen, S.L. Danielsen, B. Mikkelsen, M. Vaa, K.E. Stubkjaer, P. Doussiere, F. Pommerau, L. Goldstein, R. Ngo and M. Goix, 'All optical 40 Gbit/s OTDM to 2×20 Gbit/s WDM format translation', *Electron. Lett.*, **32**, (15), pp. 1384-1386.

P.W. Juodawlkis, D.T. McInturff and S.E. Ralph, 'Ultrafast carrier dynamics and optical nonlinearities of low-temperature-grown InGaAs/InAlAs quantum wells', *Appl. Phys. Lett.*, **69**, (26), pp. 4062-4064, December 1996.

A.M. Kan'an, P. Li Kam Wa, M. Dutta and J. Pamulapati, 'Integrated all-optical routing Y-junction device with ultrafast on/off switching', *Electron. Lett.*, **32**, (16), pp. 1476-1477, August 1996.

M.G. Kane, I. Glesk, J.P. Sokolloff and P. Prucnal, 'Asymmetric optical loop mirror: analysis of an all optical switch', *Appl. Opt.*, **33**, (29), pp.6833-6842, October 1994.

K.L. Kang, I. Glesk, T.G. Chang, P.R. Prucnal and R.K. Boncek, 'Demonstration of all optical Mach-Zender demultiplexer', *Electron. Lett.*, **31**, (9), pp. 749-750, April 1995.

Y. H. Kao, I.V. Golster, M. Jiang and M.N. Islam, 'Gain dispersion induced subpicosecond pulse breakup in afibre and semiconductor laser amplifier conbined system', *Appl. Phys. Lett.*, **69**, (27), pp. 4221-4223, December 1966.

K.C. Kao, and G.A. Hockamm, 'Dielectric fibre surface waveguides for optical frequencies', *Proc. IEE,* **113**, (7), pp.1151-1158, 1966.

H. Kawaguchi, *Bistabilities and nonlinearities in laser diodes*, Artech house inc., 1994.

S. Kawanishi, T. Morioka, O. Kamatani, H. Takara and M. Saruwatari, '100 Gbit/s, 200 km optical transmission experiment using extremely low jitter PLL timing extraction and all-optical demultiplexing based on polarisation insensitive four-wave mixing' *Electron. Lett.*, **30**, (30), pp. 800-810, May 1994.

S. Kawanishi, H. Takara, T. Morioka, O. Kamatani and M. Sarawatari, '200 GBit/s, 100 km time-division-multiplexed optical transmission using super continuum pulsse with prescaled PLL timing extraction and all-optical demultiplexing', *Electron. Lett.*, **31**, (10), pp. 816-817, May 1995.

G. L. Kazovsky, 'Optical signal processing for lightwave communication networks', *IEEE J. Sel. Areas Comm.*, **8**, (6), pp. 973-982, August 1990.

A.E. Kelly, I.F. Leaman, L.J. Rivers, S.D. Perinn and M. Silver, 'Polarisation insensitive, 25dB gain semiconductor laser amplifier without antireflection coatings', *Electron. Lett.*, **32**, (19), pp.1835-1836, September 1996.

N. Kiel, H.H Yao and C. Zawadzki, '(2×2) digital optical switch realised by low cost polymer waveguide technology', *Electron. Lett.*, **32**, (16), pp. 1470-1471.

N. Kiel, H.H. Yao, C. Zawadzki and B. Strebel, 'Rearrangeable nonblocking polymer waveguide thermo-optic 4×4 switching matrix with low power consumption at 1.55 μm' *Electron. Lett.*, **31**, (50), pp. 403-404, March 1995.

M. Koga, A. Watanabe, S. Okamoto, K. I. Sato and M. Okuno, '8×16 delivery-and-coupling type optical switches for a 320 Gbit/s throughput optical path cross-connetc system', *Electron. Lett.*, **32**, (13), pp. 1213-1214, June 1996.

V.A. Kozlov, V.V. Ter-Mikirtychev and T. Tsuboi, 'In-line single mode fibre amplifiers based on LiF_2+ and LiF_2- crystals', *Electron. Lett.*, **31**, (24), pp. 2104-2105, November 1995.

Y. Lai, K.L.Hall, E.P. Ippen and G. Eisenstein, 'Short pulse gain saturation in InGaAlAsP laser amplifiers, *IEEE Photonics Technol. Lett.*, **2**, (10), pp. 711-713, October 1990.

S.S. Lee, L.Y. Lin and M.C. Wu, 'Surface-micromachined free-space fibre-optic switches', *Electron. Lett.*, **31**, (17), pp. 1481-1482, August 1995.

K.S. Lee and C. Shu, 'Optical loop mirror multiplexer', *IEEE Photonics Technol. Lett.*, **7**, (12), pp. 1444-1446, December 1995.

W.S Lee, G. Pettitt, D. Garthe and A. Hadjifotiou, '40 Gbit/s OTDM transmission over a distance of 560 km: system implementation and performance evaluation', *Electron. Lett.*, **32**, (18), pp. 1685-1686, August 1996.

G. Lenz, E.P. Ippen, J.M. Wiesenfeld, M.A. Newkirk and U. Koren, 'Femtosecond dynamics of the non linear anisotropy in polarisation insensitive semiconductor optical amplifiers', *Appl. Phys. Lett.*, **68**, (21), pp. 2933-2935, May 1996.

J. Leuthold, J. Eckner, C. Holtmann, R. Hess and H. Melchior, 'All-optical 2×2 switches with 20 dB extinction ratios', *Electron. Lett.*, **32**, (24), pp. 2235-2236, November 1996.

E. Lichtman, 'Performance limitations imposedon all-optical ultralong lightwave systems at the zero dispersion wavelength', *J. Lightwave Technol.*, **LT-5**, (5), pp 898-905, May 1995.

A. Lomax and I.H. White, 'Modulation of picosecond pulses using semiconductor laser amplifiers', *IEE Proc. J.*, **138**, (2), pp. 178-184, april 1991.

Mm. Ligne, Y. Sorel and J.F. Kerdiles, 'Theoretical and experimental study of a saturated near travelling wave amplifier working at 1 Gbit/s and 4.8 Gbit/s', *J. Opt. Commun.*, **11**, (3), pp. 104-106, 1990.

P. LiKamWa and A. MIller, '130 ps recovery of all optical switching in a GaAs multiquantum well directional coupler', *Appl. Phys. Lett.*, **58**, (19), pp. 2055-2057, May 1991.

L.Y. lin, S.S. Lee, K.S.J. Pister and M.C. Wu, 'Micro-machined three-dimensional micro-optics for integrated free-space optical system', *IEEE Photonics Technol. Lett.*, **6**, (12), pp. 1445-1447, December 1994.

G. Lindfield and J. Penny, *Numerical Meihods Using MATLAB*, Chapter 3, Ellis Horwood, 1995.

Y.L Liu, E.K. Liu, S.L. Zhang, G.Z. Li and J.S. Luo, 'Silicon 1×2 digital optical switch using plasma dispersion', *Electron. Lett.*, **30**, (2), pp. 130-131, January 1994.

R.J. Manning and D.A.O. Davies, 'Three wavelength device for all-optical signal processing', *Opt. Lett.*, **19**, (12), pp. 889-891, June 1994.

E.A.J. Marcatili, 'Slab-coupled waveguides', *Bell. Syst. Tech. J.*, **53**, (4), pp. 645-674, 1974.

D. Marcuse, 'Computer Model Of An Injection Laser Amplifier', *IEEE J. Quantum Electron.*, **QE**-19, (1), pp 63-73, January 1983.

J. Mark and J. Mork, 'Subpicosecond gain dynamics in InGaAsP optical amplifiers: Theory and experiment', *Appl. Phys. Lett.*, **61**, (19), pp. 2281-2283, November 1992.

I.W. Marshall, D.M. Spirit and M.J. O'Mahony, 'Picosecond pulse response of atravelling wave semiconductor laser amplifier', *Electron. Lett.*, **23**, (16), pp. 818-819, July 1987.

S. Melle, 'Optical amplifier systems point to high-capacity, all optical network applications, *Lightwave*, pp. 34-37, March 1996.

R. Moosburger, G. Fischbeck, C. Kostrzewa and K. Petermann, 'Digiatl optical switch based on 'oversized' polymer rib wave guides', *Electron. Lett.*, **32**, (6), pp. 544-545, March 1996.

T. Morioka, S. Kawanishi, H. Takara, O. Kamatani, M. Yamada, T. Kanamori, K. Uchiyama, and M. Sarawutari, '100 GBit/s × 4 Ch 100 km repeaterless TDM-WDM transmission using a single supercontinuum source', *Electron. Lett.*, **32**, (5), pp. 468-470, February 1996.

T. Morioka, S. Kawanishi, H. Takara and M. Sarawatari, 'Multiple-output 100 Gbit/s all-optical demultiplexer based on multichannel four-wave mixing pumped by a linearly-chirped square pulse', *Electron. Lett.*, **30**, (23), pp.1959-1960, November 1994.

T. Morioka, S. Kawanishi, K. Uchiyama, H. Takara and M. Saruwatari, 'Polarisation-independent 100 Gbit/s all-optical demultiplexer using four wave mixing in a polarisation maintaining fibre', *Electron. Lett.*, **30**, (7), pp. 591-592, March 1994.

K. Morishita and K. Shimamoto, 'Wavelength-selective fiber loopmirrors and their wavelength tunability by twisting', *J. Lightwave Technol.*, **13**, (11), pp. 2276-2281, November 1995.

D.B Mortimore, 'Fibre loop reflectors', *J. Lightwave Technol.*, **6**, (70), pp.1217-1224, July 1988.

T. Mukai, K. Innoue and T. Saitoh, 'Homogeneous gain saturation in 1.5 μm InGaAsP travellin wave semiconductor laser amplifier', *Appl. Phys. Lett.*, **51**, (6), pp. 381-383, 1987.

E.J. Murphy, W.R. Gaylord, T.O. Murphy, M.T. Fatehi and S.S. Bergstein, ' Ti:$LiNbO_3$ photonic switch modules for large strictlt non-blocking architectures', Tec. Dig. on Photonics in switching, Paper PMD3, 1993.

E.J. Murphy, T.O. Murphy, A.F. Ambrose, R.W. Irving, B.H. Lee, P. Peng, G.W. Richards and A. Yorinks, '16×16 strictly nonblocking guided-wave optical switching system', *J. Lightwave Technol.*, **14**, (3), pp. 352-358, March 1996.

M. Nakazawa, K. Suzuki, E. Yoshida, E. Yamada, T. Kitoh and M. Kawachi, '160 Gbit/s soliton data transmission over 200 km', *Electron. Lett.*, **31**, (7), pp. 565-566, March 1995.

M. Nakazawa and E. Yoshoida, 'Direct generation of a 750 fs 10 GHz pulse train from a regeneratively mode-locked fibre laser with multiple harmonic modulation', *Electron Lett.*, **32**, (14), pp. 1291-1293, July 1996.

B.P Nelson, K.J. Blow, P.D. Constantine, N.J. Doran, J.K. Lucek, I.W. Marshall and K. Smith, 'All-optical Gbit/s switching using nonlinear loop mirror', *Electron. Lett.*, **27**, (9), pp. 704-705, April 1991.

D. Nesset, M.C. Tatham and D. Cotter, 'All-optical gate operating on 10 Gbit/s signals at the same wavelength using four wave mixing in a semiconductor laser amplifier', E*lectron Lett.*, **31**, (11), pp. 896-897, May 1995.

L. Noel, X. Shan and A.D. Ellis, 'Four WDM channel NRZ to RZ format conversion using a single semiconductor laser amplifier', *Electron. Lett.*, **31**, (4), pp. 277-278, February 1995.

A.C. O' Donnell, 'Polarisation independent 1×16 and 1×32 lithium niobate optical switch matrixes', *Electron. Lett.*, **27**, (25), pp. 2349-2350, December 1991.

H. Okayama and M. Kawahara, 'Prototype 32×32 switch matrix', *Electron. Lett.*, **30**, (14), pp. 1128-1129, July 1994.

H. Okayama, T. Ushikubo and T. Ishida, 'Directional coupler switch with reduced voltage-length product', *J. Lightwave Technol.*, **LT-9**, (section IV), p. 1565, 1991.

E. Ollier. P. Labeye and F. Revol, 'A micro opto-mecahanical switch integrated on silicon', *Electron. Lett.*, **31**,(23), pp. 2003-2005, 1995.

E. Ollier and P. Mottier, 'Integrated electrostatic micro-switch for optical fibre networks driven by low voltage', *Electron. Lett.*, **32**, (21), pp. 2007-2009, October 1996.

M.J. O'Mahony, 'Semiconductor laser amplifiers for use in future fibre systems, *IEEE J. Lightwave Technol*, **LT-6**, (4), pp.531-544, April 1988.

M.J. O'Mahony, D. Simeonidou, A. Yu and J. Zhou, 'The design of a European optical network', *J. Lightwave Technol.*, **LT-13**, (5), May 1995.

M.J. O'Mahony, M.C. Sinclair and B. Mikac,'Ultra High Capacity Transmission network European research project COST 239' in *Conf. On Telecomm*, CONTEL 93, Zagreb, July 1993.

A.W. O' Neill, 'All-optical loop-miror switch employing an asymmetric amplifier/attenuator combination', *Electron. Lett.*, **26**, (24), pp. 2008-2009, November 1990.

D. O'ttavi, E. Iannone and S. Scotti, 'Address recognition in all-optical packet switching by FWM in semiconductor laser amplifiers', *Microwave Opt. Technol. Lett.*, **10**, (4), pp. 228-230, November 1995.

K.E. Petersen, 'Michromechanical light modulator array fabricated on silicon', *J. Appl. Phys. Lett.*, **31**, (18), pp. 521-523, 1977.

M. Potenza, 'Optical fibre amplifiers for telecommuncation systems',*IEEE Communications Mgazine*, pp. 96-102, August 1996.

C. Radzewicz, M.J. la Grone and J.S. Krasinski, 'Passive pulse shaping of femto second pulses using birefringent dispersive media ', *Appl. Phys. Lett.*, **69**, (2), pp. 272-274, July 1996.

S. Ruiz-Moreno, J. Guitart, 'Practical method for modelling the nonlinear behaviour of a travelling wave semiconductor laser amplifier', *IEE Proc. J*, **140**, (1), pp. 39-43, February 1993.

F. Schliep, D. Garus and R. Hereth, 'Polarisation dependence of the phase shift of 2×2 single mode fibre directional couplers', *Electron. Lett.*, **30**, (1), pp. 78-80, January 1994.

J. Senior, *Optical Fibre Communications. Principles and Practice.* Second edition. 1992.

Y. Shibata, S. Oku, Y. Kondo, T. Tamamura and M. Naganuma, 'Semiconductor monolithic wavelength selective router using a grating switch integrated with adirectional coupler' *J. Lightwave Technol.*, **LT-14**, (6), pp. 1027-1032, June 1996.

S.P Shipley, G. Gergiou and A.C. Boucouvalas, 'Compact all-fibre Mach Zender devices', *IEE Proc. J.*, **134**, (3), pp. 203-207, June 1987.

Y.N. Singh, V.K. Jain and H.M. Gupta, 'Semiconductor optical amplifiers in WDM star networks, *IEE Proc. Optoelectron.*, **143**, (2), pp. 144-152, April 1996.

D.A. Smith, R.S. Chakravarthy, Z. Bao, J.E. Baran, J.L. Jackel, A. d'Alessandro, D. J. Fritz, S.H. Huang, X.Y. Zou, S.M. Hwang, A.E. Willner and K.D. Li, 'Evolution of the acousto-optic wavelength routing switch', *J. Lightwave Technol.*, **LT-14**, (6), pp. 1005-1019, June 1996.

J.P Sokolloff, I. Glesk, P.R. Prucnal, and R.K. Boncek, 'Performance of a 50 Gbit/s optical time domain multiplexed signal using a terahertz optical asymmetric demultiplexer, *IEEE Photonics Technol. Lett.*, **6**, (1), pp. 98-100, January 1994.

J.O. Sokolloff, P.R. Prucnal, I. Glesk and M. Kane, ' A terahertz optical asymmetric demultiplexer (TOAD)', *IEEE Photonics Technol. Lett.*, **5**, (7), pp. 787-790, July 1993.

D.M. Spirit and L.C. Blank, 'Optical time division multiplexing for future high-capacity network applications', *BT Technol. J.*, **11**, (2), pp. 35-45, April 1993.

M.S. Stix, M.P. Kesler and E.P. Ippen, 'Observations of subpicosecond dynamics in GaAlAs laser diodes', *Appl. Phys. Lett.*, **48**, (25), pp. 1722-1724, June 1986.

A. Strass, ' OTDM switch on a chip blazes at 20 GBit/s', *Lightwave*, p. 14, June 1996.

H.Taga, 'Long distance transmission experiments using the WDM technology', *J. Lightwave Technol.*, **LT-14**, (6), pp. 1287-1298, June 1996.

C. Tai and W. Way, ' Dynamic range and switching speed limitations of an N×N optical packet switch based on low-gain semiconductor optical amplifiers', *J. Lightwave Technol.*, **LT-14**, (4), pp. 522-533, April1996.

T. Takiguchui, S. Kawanishi, H. Takara, O. Kamatani, K. Uchiyama, A. Himeno and K. Jinguji, 'Dispersion slope equalising experiment using planar lightawave circuit for 200 Gbit/s time-division-multiplexed transmission', *Electron. Lett.*, **32**, (22), pp. 2083-2085, October 1996.

J.M. Tang, P.S. Spencer and K.A. Shore, 'Effect of semiconductor no linear gain on the chirp and spectral properties of amplified subpicosecond optical pulses', *Electron Lett.*, **32**, (14), pp. 1293-1294, July 1996.

L.F. Teimeijer, P.J.A. Thijis, T van Dongen, J.J.M. Binsma and E.J. Jansen, 'Polarisation resolved, complete characterisation of 1310 nm fiber pigtailed multiple-quantum-well optical amplifiers, *J. Lightwave Technol.*, **LT-14**, (6), pp. 1524-1533, June 1996.

K. Uchiyama, S. Kawanishi, H.Takara, T. Morioka and M. Sarawatari, '100 Gbit/s to 6.3 Gbit/s demultiplexing experiment usin polarisation-independent nonlinear optical loop mirror', *Electron. Lett.*, **30**, (11), pp. 873-875, May 1994.

K. Uchiyama, H.Takara, T. Morioka, S. Kawanishi and M. Sarawatari, '*Electron. Lett.*, **32**, (21), pp. 1989-1991.

A. Uskov, J. Mork and J. Mark, 'Theory of short-pulse gain saturation in semiconductor laer amplifiers', *IEEE Photonics Technol. Lett.*, **4**, (5), pp. 443-446, May 1992.

A. Uskov, J. Mork and J. Mark, 'Wave mixing in semiconductor laser amplifiers due to carrier heating and spectral hole burning, *IEEE J. Quantum Electron.*, **QE-30**, (8), pp. 1769-1781, August 1994.

A. Villeneuve, J.S. Aitchison, B. Vogele, R. Tapella, J.U. Kang. C. Trevino and G.I. Stegeman, 'Waveguide design for minimum nonlinear effective area and switching energy in AlGaAas at half the bandgap' *Electron. Lett.*, **31**, (7), pp. 549-551, March 1995.

Z. Wang, E. Bodkter and G. Jacobsen, 'effects of cross phase modulation in wavelength-multiplexed SCM video transmission system', *Electron. Lett.*, **31**, (18), pp. 1591-1592, August 1995.

L.D. Westbrook, 'Measurements of *dg/dN* and *dn/dN* and their dependence on photon energy in $\lambda = 1.5$ μm InGaAsP laser diodes', *IEE Proc. J.*, **133**, (2), pp. 135-142, April 1986.

J.M. Wiesenfield, G. Eisenstein, R.S. Tucker, G. Raybon and P.B. Hanse, 'Distortionless picosecond pulse amplification and gain compression in a travelling-wave InGaAsP optical amplifier', *Appl. Phys. Lett.*, **53**,(14), pp. 1239-1241, October 1988.

M. Willatzen, A. Uskov, J. Mork, H. Olsen, B. Tromberg and A.P. Jauho,'Nonlinear gain supression in semiconductor lasers due to carrier heating', *IEEE Photonics Technol. Lett.*, **26**, (7), pp. 606-609, July 1991.

E.L. Wooten, R.L. Stone, E.W. Miles and E.M. Bradley,' Rapidly tunable narrowband filter using $LiNb0_3$ unbalanced Mach-Zender interferometers', *J. Lightwave Technol.*, **LT-14**, (11), pp. 2530-2536, November 1996.

H. Yanagawa, K. Ueki and Y. Kamata, 'Polarisation and wavelength-insensitive guided-wave-optical switch with semiconductor Y-junction', *J. Lightwave Technol.*, **LT-8**, (80), pp. 1192-1197, August 1990.

A.Yariv, '*Optical electronics*', Saunders college publishing, 1991.

A. Yariv, *Quantum Electronics*, 2nd. ed. Wiley 1975.

A. Yu and M. O'Mahony, ' Optimisation of wavelength spacing in a WDM transmission system in the presence of fibre nonlinearities', *IEE Proc. Optoelectron.*, **142**, (4), pp. 190-196, August 1995.

J. Zhang, 'Very high speed fibre optic networks for broadband communications', *IEE Electron. & Comm. Eng. Journal,* pp. 257-268, December 1996.